

The e-TidalGCs project

Modeling the extra-tidal features generated by Galactic globular clusters

Salvatore Ferrone¹ , Paola Di Matteo¹, Alessandra Mastrobuono-Battisti¹, Misha Haywood¹, Owain N. Snaith¹, Marco Montuori², Sergey Khoperskov^{3,1}, and David Valls-Gabaud⁴

¹ GEPI, Observatoire de Paris, PSL Research University, CNRS, Place Jules Janssen, 92195 Meudon Cedex, France
e-mail: salvatore.ferrone@obspm.fr

² SMC-ISC-CNR and Dipartimento di Fisica, Sapienza University, P.le Aldo Moro 2, 00185 Rome, Italy

³ Leibniz-Institut für Astrophysik Potsdam (AIP), An der Sternwarte 16, 14482 Potsdam, Germany

⁴ LERMA, CNRS UMR 8122, Observatoire de Paris, PSL, 61 Avenue de l'Observatoire, 75014 Paris, France

Received 29 May 2022 / Accepted 27 December 2022

ABSTRACT

We present the e-TidalGCs project, aimed at modeling and predicting the extra-tidal features surrounding all Galactic globular clusters for which 6D phase-space information, masses, and sizes are available (currently numbering 159 globular clusters). We focus the analysis and presentation of the results on the distribution of extra-tidal material on the sky, as well as on the different structures found at different heliocentric distances. We emphasize the wide variety of morphologies found: beyond the canonical tidal tails, our models reveal that the extra-tidal features generated by globular clusters take a wide variety of shapes, from thin and elongated shapes to thick and complex halo-like structures. We also compare some of the most well-studied stellar streams found around Galactic globular clusters to our model predictions, namely, those associated with the clusters NGC 3201, NGC 4590, NGC 5466, and Pal 5. Additionally, we investigate how the distribution and extension in the sky of the simulated streams vary with the Galactic potential by making use of three different models, either containing a central spheroid, not containing one, or containing a stellar bar. Overall, our models predict that the mass lost by the current globular cluster population in the field from the last 5 Gyrs is between $0.3\text{--}2.1 \times 10^7 M_{\odot}$. This amount is comparable to a value between 7–55% of the current mass. Most of this lost mass is found in the inner Galaxy, with the half-mass radius of this population being between 4–6 kpc. The outputs of the simulations will be publicly available, coinciding with the unique opportunity presented by the delivery of the ESA *Gaia* mission and complementary spectroscopic surveys. Their exquisite data will offer the possibility to carry out novel comparisons with the models discussed in this work.

Key words. globular clusters: general – Galaxy: structure – Galaxy: kinematics and dynamics – Galaxy: evolution – methods: numerical

1. Introduction

Globular clusters are the oldest gravitationally bound stellar systems in the Galaxy (Meylan & Heggie 1997). About 170 are currently known in the Milky Way (Vasiliev & Baumgardt 2021) and the census is still incomplete, particularly in the inner regions of the bulge and disk of our Galaxy, where dust extinction and high stellar number density limit detections. It is in these regions in particular that new globular cluster candidates have been recently discovered, especially thanks to the analysis of near-infrared surveys (Moni Bidin et al. 2011; Minniti et al. 2011, 2017a,b, 2018, 2021a,b; Gran et al. 2019, 2022; Garro et al. 2020, 2021, 2022a,b). The current population of globular clusters is likely to merely represent the leftovers of an initially more numerous and more massive one that had been depopulated as a result of many disruptive processes (Gnedin & Ostriker 1997; Murali & Weinberg 1997b,a; Vesperini & Heggie 1997; Fall & Zhang 2001). One of the main processes affecting the globular cluster population and its evolution in number, mass, and size is tidal stripping.

As all stellar systems are characterized by a finite size and defined orbit of the Galaxy, globular clusters are subject to tidal effects, which arise because the opposite sides of these systems experience a different gravitational acceleration. The

long-term effect of this process strips the system of its most loosely bound stars, which redistribute themselves onto orbits similar to those of their progenitor, forming so-called “tidal tails” or streams around it (see Grillmair et al. 1995; Leon et al. 2000, for some of the earliest studies). Some spectacular tails have been discovered and studied over the past twenty years around Milky Way globular clusters, ranging from the long tails (of roughly 30° degrees) departing from the Palomar 5 cluster (Odenkirchen et al. 2001, 2003, 2009; Grillmair & Dionatos 2006a; Thomas et al. 2016; Starkman et al. 2020; Ibata et al. 2021) to those of NGC 5466 (Belokurov et al. 2006), Palomar 14 (Sollima et al. 2011), and the GD-1 stream, whose parent cluster has still to be discovered (or has already been completely destroyed, leaving behind the stream as the only vestige of its past existence; see Grillmair & Dionatos 2006b; Webb & Bovy 2019; Bonaca et al. 2020a). These studies have been boosted in the last few years thanks to the publication of the ESA *Gaia* mission catalogues (Gaia Collaboration 2016, 2018, 2021b,a) which has been delivering parallaxes, proper motions, and magnitudes for about 1.4 billion stars, as well as the radial velocities for several million, and thus allowing for searches of stars with coherent distances and motions in the Galaxy, revealing the existence of a number of new and spectacular streams, as well as rediscovering and confirming already

known ones (Navarrete et al. 2017; Malhan et al. 2018a,b, 2019, 2021; Ibata et al. 2018, 2019a,b, 2020, 2021; Piatti 2018, 2021, 2022; Shipp et al. 2018; Kaderali et al. 2019; Bianchini et al. 2019; Malhan & Ibata 2019; Palau & Miralda-Escudé 2019, 2021; Piatti & Carballo-Bello 2019, 2020; Caldwell et al. 2020; Piatti & Fernández-Trincado 2020; Piatti et al. 2020, 2021; Shipp et al. 2020; Thomas et al. 2020; Boldrini & Vitral 2021; Jensen et al. 2021; Yuan et al. 2022; Zhang et al. 2022; Nie et al. 2022). For a general overview, Mateu (2023) provides a recent compilation of known stellar streams.

All these studies are unraveling a very complex and rich set of stellar structures in the Milky Way that are mainly distributed in the halo, where their identification is the easiest because of the low density of the background stellar field. From a numerical and theoretical point of view, many studies over the years have been focused on the formation and evolution of tidal streams around globular clusters (Keenan & Innanen 1975; Oh & Lin 1992; Oh et al. 1992; Grillmair et al. 1998; Combes et al. 1999; Ibata et al. 2002; Johnston et al. 2002; Yim & Lee 2002; Capuzzo Dolcetta et al. 2005; Di Matteo et al. 2005; Montuori et al. 2007; Siegal-Gaskins & Valluri 2008; Küpper et al. 2010, 2012; Lane et al. 2010; Mastrobuono-Battisti et al. 2012; Sanders & Binney 2013; Bovy 2014; Amorisco et al. 2016; Erkal et al. 2016; Sanders et al. 2016; Pearson et al. 2017; Carlberg 2018, 2020; Thomas et al. 2018; Vitral & Boldrini 2022). These studies have contributed to understanding how these structures form and evolve, to what extent they trace the globular cluster orbit, and how their shape, extension, and morphology depend on the orbital phase and characteristics of the Galactic potential, as well as on the potential tidal shocks experienced by the cluster itself when it crosses the Galactic disk.

Some works have presented models and simulations for specific streams (Dehnen et al. 2004; Mastrobuono-Battisti et al. 2012; Banik & Bovy 2019; Bonaca et al. 2019; Banik et al. 2021a; Mirabal & Bonaca 2021), contributing to an understanding of their morphology, density variations, and their extent. From these works, it is clear that the tidal loss of stars from globular clusters and the formation of related structures are important for several reasons: (1) in quantifying to what extent globular clusters have contributed to the field stellar populations, from the halo to the disk to the bulge, and to what extent they still do; (2) reconstructing the properties (in terms of numbers and masses) of the early Galactic globular clusters, through their current mass loss; and (3) using globular cluster streams as a probe of the Galactic potential and, more generally, of the physical laws governing gravity (see, e.g., Thomas et al. 2018; Bianchini et al. 2019; Naik et al. 2020; Banik et al. 2021a,b).

In this paper, we wish to contribute to the current discourse on this matter by presenting the first complete catalog of simulated extra-tidal features around globular clusters. We emphasize that we are speaking generically on their features, rather than specifically on tails or streams, because the latter are but one of the morphologies that extra-tidal material can reveal, as we go on to show in this work. This project is motivated, on the one hand, by the aforementioned discoveries of many numerous new streams and tails in the Galaxy and, on the other hand, by the availability of the full 6D phase information and internal parameters (masses and sizes) for more than 150 Galactic globular clusters (Baumgardt & Hilker 2018; Baumgardt & Vasiliev 2021; Vasiliev & Baumgardt 2021). The aims of this project are manifold: (1) to obtain a complete view of the expected distribution of globular clusters tidal structures in the sky; (2) to inform the interpretation of recent and future discoveries; (3) to support

the search for new extra-tidal features in the data; (4) to offer the community a repository of all these models to be compared to other theoretical and numerical predictions, which adopt different Galactic potentials and/or gravity laws.

2. Numerical method

To model the formation and evolution of extra-tidal features around Galactic globular clusters, we use a set of codes, called Globular Clusters' Tidal Tails (GCsTT) developed by our group. It comprises two python codes, for the backward and forward integration of a stellar system, made of N test-particles (see Sect. 2.1). These codes are separated for data organization and management, while the (computationally) most expensive part, namely, the calculation of the accelerations acting on the N particles and the orbits integration, is realized by means of a Fortran module written by our group. This module is interfaced to python by means of f2py directives from NumPy. The use of test-particle methods for modeling the tidal stripping process is widespread in the literature, where these methods are usually applied to one or few clusters at a time (see, e.g., Lane et al. 2012; Mastrobuono-Battisti et al. 2012; Palau & Miralda-Escudé 2019; Piatti et al. 2021; Grillmair 2022). In this work, we apply a test-particle methodology to the whole set (159) of Galactic globular clusters for which this is currently possible, also taking into account, for each cluster, the errors on astrometry, line-of-sight velocities¹ and distances. In the following, we describe the two main steps of the procedure used by GCsTT to simulate the tidal stripping process (Sect. 2.1), the initial conditions adopted for the clusters' parameters and their mass distribution (Sect. 2.2), as well as the Galactic potentials (Sect. 2.3).

2.1. Simulations of the tidal stripping process: Two-step procedure

To model the formation and evolution of extra-tidal features around Galactic globular clusters, and predict their current properties, we proceed as follows:

– Step i: Backward integration. Reconstructing the globular cluster orbit over the last 5 Gyr: First, for each Galactic globular cluster for which the distances from the Sun, proper motions, line-of-sight velocities, and structural parameters are available (see Sect. 2.2), we determine their current positions and velocities in a Galactocentric reference frame, in which the Sun is at $(x_{\odot}, y_{\odot}, z_{\odot}) = (-8.34, 0., 0.027)$ kpc (Chen et al. 2001; Reid et al. 2014) and at a given velocity for the local standard of rest, $v_{\text{LSR}} = 240 \text{ km s}^{-1}$ (Reid et al. 2014), and a peculiar velocity of the Sun with respect to the LSR, $(U_{\odot}, V_{\odot}, W_{\odot}) = (11.1, 12.24, 7.25) \text{ km s}^{-1}$ (Schönrich et al. 2010). We then integrate the orbit of a single point mass, representing the cluster barycenter, backwards in time for 5 Gyr, and in this way, we retrieve its position and velocity at that time in the chosen Galactic potential (see Sect. 2.3). We notice that other choices for the Sun's position or velocity with respect to the Galactocentric frame would have been possible. For example, Piatti et al. (2021)

¹ Note: the term “line-of-sight velocities” adopted in this paper corresponds to the term “radial velocities” often used in the literature, as well as in the *Gaia* catalogues. We prefer the use of the first term, since the second is usually used also to indicate the (Galactocentric) radial velocities and can introduce some ambiguity, especially when different coordinate systems are used. We emphasize that the choice to use the term “line-of-sight velocity” is not new (see, e.g., Vasiliev & Baumgardt 2021).

adopted the same values as ours for the v_{LSR} and for the peculiar velocity of the Sun but with a different distance to the Galactic center (8.1 kpc in their work, see [GRAVITY Collaboration 2018](#)). The difference in the adopted position of the Sun is, however, generally smaller than the uncertainties affecting our knowledge of the distance of Galactic globular clusters to the Sun. For this reason, we do not to explore the dependency of the results presented in this paper with regard to these choices.

– Step ii: Forward integration. Test-particle streams from the past to the present day: Once the positions and velocities of the barycenter of each cluster, 5 Gyr ago, have been determined, we build the corresponding N -body system, with $N = 100\,000$ particles. The phase-space coordinates of these particles are generated following a Plummer distribution, with the total mass and half-mass radius as described in Sect. 2.2. The barycenter of this N -body cluster is then assigned initial positions and velocities in the Galactic model, as those retrieved at step (i), and the cluster is then integrated forward in time until the present day. Particles in this N -body system are modeled as test-particles, that is, they experience the gravitational field exerted by the globular cluster itself (see Sect. 2.2) and by the Galaxy (see Sect. 2.3), but do not generate any gravitational field themselves. This allows us to maintain a computational time which scales as $O(N)$ and not as $O(N^2)$, as would be the case for a direct N -body self-consistent computation.

In the following, we refer to these simulations, made by using the most probable values on distances, proper motions, and line-of-sight velocities, as the “reference simulations.” In addition, for each globular cluster, we also take into account the errors on its distance, proper motions, and line-of-sight velocity, assuming Gaussian distributions of the errors, treated independently, and by generating 50 random realizations of these parameters. For each of these realizations, we repeat the steps described above, that is: (step i) we determine the associated current positions and velocities in the chosen Galactocentric reference frame, we integrate the orbit of the single-point mass (representing the cluster barycenter) backwards in time, retrieving the corresponding values 5 Gyr ago, (step ii) we build an N -body cluster containing $N = 100\,000$ particles, with total mass and half-mass radius as those used for the reference simulation, and then we integrate the N -body cluster forwards in time until the present-day position.

To summarize, for a given Galactic potential, we run $159 \times (50 + 1) = 8109$ simulations, where 159 is the total number of clusters for which we currently have both 6D phase-space information and structural parameters. As we discuss in the following section, the whole set of globular clusters has been evolved in three different Galactic potentials, which implies that a total of 24 327 simulations have been run.

For the orbit integration, a leap-frog algorithm is used, with a fixed time-step, Δt , and a total number of steps, N_{steps} , such that the total simulated time is $\Delta t \times N_{\text{steps}} = 5$ Gyr. The choice of the value of Δt adopted to simulate each cluster in the Galactic potential has been based on the energy conservation of the corresponding cluster evolved in isolation (i.e., without the effect of the Galactic gravitational field for 5 Gyr). For the majority of the clusters (109/159), this value was set to $\Delta t = 10^5$ yr (for a corresponding value of $N_{\text{steps}} = 50\,000$), while for the remaining clusters (50/159) a $\Delta t = 10^4$ yr (for a corresponding value of $N_{\text{steps}} = 500\,000$) was used. We refer to Appendix B (and in particular to Table B.1) for additional details on the choice of Δt for the whole set of clusters. As for the total simulated time, while globular clusters are much older than 5 Gyr, we chose this time limit because the longer back in time we could go, the less

certain we would be of the Galactic environment. In addition, the last significant mergers in the Galaxy happened between 9 and 11 Gyr ago (see [Belokurov et al. 2018](#); [Helmi et al. 2018](#); [Di Matteo et al. 2019](#); [Gallart et al. 2019](#); [Kruijssen et al. 2020](#)) – well before the time interval simulated in this study. Other more recent interactions, such as the accretion of Sagittarius and of the Magellanic Clouds, may perturb the Galactic potential as well (see, e.g., [Vasiliev et al. 2021](#)) and we plan to investigate their impact on the properties of globular cluster streams in the future.

For each realization, we generate an output file in an hdf5 format² containing the values for the right ascension (α), declination (δ), distance from the Sun (D), along with the components for proper motion in the equatorial coordinate system ($\mu_\alpha \cos(\delta)$ and μ_δ), the line-of-sight velocity (v_{los}), longitude (ℓ), latitude (b), as well as the components for proper motion in the Galactic coordinate system ($\mu_\ell \cos(b)$ and μ_b) and the Galactocentric positions (x, y, z), velocities (v_x, v_y, v_z) and energy, E , of each particle in the simulated system. We used Astropy ([Astropy Collaboration 2013, 2018](#)) to convert the Galactocentric positions and velocities in the equatorial and Galactic quantities $\alpha, \delta, D, \mu_\alpha \cos(\delta), \mu_\delta, v_{\text{los}}, \ell, b, \mu_\ell \cos(b)$, and μ_b .

For each particle, we also save its escape time t_{esc} , defined as the time at which the particle escapes from the cluster, that is, the time, t , at which the particle satisfies the relation³:

$$E_{\text{GC}} = 0.5 \times \left((v_x - v_{x,\text{GC}})^2 + (v_y - v_{y,\text{GC}})^2 + (v_z - v_{z,\text{GC}})^2 \right) + \Phi_{\text{GC}} > 0, \quad (1)$$

with E_{GC} being the total specific energy of the particle relative to the cluster, that is, the sum of the potential energy, Φ_{GC} , due to the gravitational field of the cluster (see Eq. (2)), and of the kinetic energy, relative to the cluster barycenter, $T_{\text{GC}} = 0.5 \times \left((v_x - v_{x,\text{GC}})^2 + (v_y - v_{y,\text{GC}})^2 + (v_z - v_{z,\text{GC}})^2 \right)$, where v_x, v_y , and v_z are its velocity components at time, t , and $v_{x,\text{GC}}, v_{y,\text{GC}}$, and $v_{z,\text{GC}}$ of the cluster barycenter at the same time. A positive value of E_{GC} implies that the particle is no longer gravitationally bound to the cluster and, hence, it is lost in the field. Overall, the total volume of the whole set of 24 327 simulations, saved in hdf5 format, amounts to about 370 Gb.

2.2. Simulations of the tidal stripping process: GCs' current and initial conditions and their gravitational potential

Steps (i) and (ii) described in the previous section require some input conditions to be adequately executed. The current distances from the Sun, proper motions, and line-of-sight velocities, as well as the related uncertainties, of all 159 globular clusters considered in this study are taken respectively from [Baumgardt & Vasiliev \(2021\)](#) and [Vasiliev & Baumgardt \(2021\)](#). These values are then converted into Galactocentric positions and velocities by making use of Astropy and used as initial conditions to execute step (i).

Step (ii) requires generating an N -body system, representing the globular cluster, whose initial total mass and half-mass radius are assigned on the basis of their current values, as given by [Baumgardt & Hilker \(2018\)](#)⁴ and reported in Table A.1. As anticipated at step (ii) in Sect. 2.1, the phase-space coordinates of

² <https://www.hdfgroup.org/solutions/hdf5/>

³ If the particle is gravitationally bound to the cluster until the end of the simulation, t_{esc} is set equal to -9999 .

⁴ In particular, the adopted values have been taken from the edition available at <https://people.smp.uq.edu.au/HolgerBaumgardt/globular/parameter.html>, up to January 14, 2022.

each N -body cluster are generated by assuming a Plummer distribution of total mass, M_{GC} , and half-mass radius, r_h , for which the corresponding potential is:

$$\Phi_{GC}(r) = -\frac{GM_{GC}}{\sqrt{r^2 + r_c^2}}, \quad (2)$$

where r_c is the cluster scale radius and it is related to the half-mass radius, r_h , through $r_h \approx 1.305r_c$ (Heggie & Hut 2003). The variable r here indicates the distance of the test particle from the center of the cluster. For each cluster, the same Plummer distribution used to generate the N -body system is also used to calculate the accelerations exerted on each particle as the system moves through time. The Plummer sphere, representing the cluster potential, indeed moves through the Galaxy along the orbit retrieved at step (i), traveling this time in the opposite direction, from 5 Gyr ago to the present day.

It might be noted that this implies that the globular cluster density profile and its internal parameters (total mass and characteristic radius) are constant over time in these models. This is, of course, a crude approximation, because in reality both the internal parameters and the density profile itself can change over time. We consider these assumptions to be acceptable within the scope of our work given that we are primarily interested in the distribution of extra-tidal stars, which had once escaped from the cluster have dynamics primarily dictated by the Galactic potential rather than the globular cluster itself. Of course, the density of stars along the extra-tidal structures, as well as the total mass lost, depend on these assumptions. That is to say that if the mass of the cluster was not assumed constant over time, but could possibly decrease, the gravitational attraction exerted by the cluster itself on its stars would be weaker and this would lead to an increasing mass loss and density along the tails. We could have proceeded with diminishing the mass over time, based on some assumptions on the temporal behavior of this relation, however, we did not find this approach satisfying. In this way, we would have taken into account a temporal evolution of the mass, but not of the size of the cluster, adding a supplementary hypothesis to the problem. For these reasons, we decided to maintain the simplest approach. We emphasize that other groups have followed the same methodology, maintaining masses and sizes that remain constant over time (see, e.g., Palau & Miralda-Escudé 2019).

The summary tables giving both the current internal parameters of the clusters (total mass and half-mass radius), their astrometric quantities of relevance for this study and the line-of-sight velocities are publicly available⁵. We have made use of these tables for our work and we report them in a unique table in our paper for the sake of the completeness and self-consistency of the data used (see Table A.1).

2.3. Simulations of the tidal stripping process: Galactic potentials

As for the Galactic mass distribution, we make use of the two axisymmetric Galactic mass models presented in Pouliaxis et al. (2017) and of an asymmetric mass model, containing a central stellar bar, and we present it here for the first time. We recall the main properties of the two models of Pouliaxis et al. (2017) below and we describe the asymmetric Galactic mass model, presented here for the first time, in more detail.

⁵ All data can be found here <https://people.smp.uq.edu.au/HolgerBaumgardt/globular>

2.3.1. Model I by Pouliaxis et al. (2017): An axisymmetric mass model for the Galaxy including a spherical bulge

Model I by Pouliaxis et al. (2017, abbreviated name: PI) consists of four components: two disks (thin and thick), both described by Miyamoto & Nagai potentials, a dark matter halo, and a central bulge. Its total potential is:

$$\Phi_{\text{tot}}(R, z) = \Phi_{\text{thin}}(R, z) + \Phi_{\text{thick}}(R, z) + \Phi_{\text{halo}}(r) + \Phi_{\text{bulge}}(r), \quad (3)$$

with $r = \sqrt{R^2 + z^2}$,

$$\Phi_{\text{thin}}(R, z) = \frac{-GM_{\text{thin}}}{\left(R^2 + \left[a_{\text{thin}} + \sqrt{z^2 + b_{\text{thin}}^2}\right]^2\right)^{1/2}}, \quad (4)$$

$$\Phi_{\text{thick}}(R, z) = \frac{-GM_{\text{thick}}}{\left(R^2 + \left[a_{\text{thick}} + \sqrt{z^2 + b_{\text{thick}}^2}\right]^2\right)^{1/2}}, \quad (5)$$

$$\Phi_{\text{halo}}(r) = \frac{-GM_{\text{halo}}}{r} - \frac{M_{\text{halo}}}{1.02a_{\text{halo}}} \times \left[\frac{-1.02}{1 + \left(\frac{r}{a_{\text{halo}}}\right)^{1.02}} + \ln\left(1 + \left(\frac{r}{a_{\text{halo}}}\right)^{1.02}\right) \right]_{R}^{100}, \quad (6)$$

and

$$\Phi_{\text{bulge}}(r) = -\frac{GM_{\text{bulge}}}{\sqrt{r^2 + b_{\text{bulge}}^2}}, \quad (7)$$

where M_{thin} , M_{thick} , M_{halo} , and M_{bulge} are the masses of the disks, halo, and bulge. Also, a_{thin} , b_{thin} , a_{thick} , b_{thick} , a_{halo} , b_{bulge} are the characteristic scale lengths of the thin and thick disks, the halo, and the central bulge, respectively (see Table 1).

This model is a modification of the classical Allen & Santillan (1991) model, made to include also the presence of a thick disk. As it has been discussed in detail by Pouliaxis et al. (2017), the choice to include a massive spheroid in this model, as well as in the original Allen & Santillan (1991) model, is dictated by the need to reproduce CO/HI-based velocity curves, as those provided by Sofue (2012), which show a rise and then a sudden decrease of the velocity curve in the inner Galactic regions ($R \leq 2-3$ kpc). In an axisymmetric model, such a rise can be reproduced only if a central spheroidal component, with a typical mass greater than 10% of that of the disk(s), is added. However, as shown by Chemin et al. (2015), the central rise observed in the rotation of the molecular gas in the inner Galaxy may be an effect of non-circular motions generated by large-scale asymmetries such as the bar. Moreover, this feature is not reported in all the observational studies (see, e.g., Reid et al. 2014, on which model PII is based). In other words, if we do not assume that the mass distribution of the inner Galaxy is axisymmetric, the need for a massive spheroidal component to reproduce velocity curves, such as those from Sofue (2012), no longer persists. In addition to that, in the last decade, a number of works have shown that if a spheroidal bulge exists in the central regions of our Galaxy, it has to be small (few percents of the mass of the disk at the most, see among others Shen et al. 2010; Kunder et al. 2012; Di Matteo et al. 2015; Gómez et al. 2018). All these arguments suggest to employ this model (as well as all models including a massive central spheroid; see, e.g., Irrgang et al. 2013) with care when dealing with the central parts of the Galaxy. Since models with a massive central spheroid,

Table 1. Parameters of the Galactic mass models adopted in this work.

Parameters	M_{bulge}	M_{bar}	M_{thin}	M_{thick}	M_{halo}	b_{bulge}	a_{bar}	b_{bar}	c_{bar}	a_{thin}	b_{thin}	a_{thick}	b_{thick}	a_{halo}
PI	460.0	0.0	1700.0	1700.0	6000.0	0.3	–	–	–	5.3000	0.25	2.6	0.8	14.0
PII	0.0	0.0	1600.0	1700.0	9000.0	–	–	–	–	4.8000	0.25	2.0	0.8	14.0
PII-0.3-SLOW	0	990.0	1120.0	1190.0	9000.0	–	4.0	1.	0.5	4.8000	0.25	2.0	0.8	14.0

Notes. Masses are in units of $2.32 \times 10^7 M_{\odot}$, distances given in units of kpc.

however, are still used in the literature, we have included model PI here, as a term of comparison.

2.3.2. Model II by Pouliaxis et al. (2017): An axisymmetric, bulge-less mass model for the Galaxy

Model II by Pouliaxis et al. (2017, abbreviated name: PII) consists of a spherical dark matter halo, with the same functional form adopted in the Allen & Santillan (1991) model, and of two disk components (a thin and a thick disk), with same functional form as PI. This model does not include any central spheroid (i.e., it is a bulge-less model) and thus its total potential is the sum of three components only:

$$\Phi_{\text{tot}}(R, z) = \Phi_{\text{thin}}(R, z) + \Phi_{\text{thick}}(R, z) + \Phi_{\text{halo}}(r), \quad (8)$$

with the thin, thick disks, and dark matter halo having the same functional forms adopted in PI.

As it has been shown in Pouliaxis et al. (2017), this model satisfies a number of observational constraints, such as the stellar density at the solar vicinity, thin- and thick-disk scale lengths and heights, the rotation curve as provided by Reid et al. (2014) and the absolute value of the perpendicular force, K_z , as a function of distance to the Galactic centre (see Sect. 2.5 in Pouliaxis et al. 2017). As it is, however, an axisymmetric model, it fails to accurately describe the inner few kpc of the Galaxy, where the stellar mass distribution has been shown to be asymmetric.

2.3.3. Model II with a massive, slowly rotating stellar bar

The third mass model (abbreviated name: PII-0.3-SLOW) that we use in this paper is a version of PII by Pouliaxis et al. (2017) modified to include a rotating stellar bar, whose mass has been assigned to be 30% of the (thin+thick) disk mass of PII. We assume that the bar rotates with a constant pattern speed of $\Omega_{\text{bar}} = 38 \text{ km s}^{-1} \text{ kpc}^{-1}$ and that it is currently inclined of 25° with respect to the Sun-Galactic center direction (see Bland-Hawthorn & Gerhard 2016). We model it as a triaxial distribution, whose gravitational potential is given by Long & Murali (1992):

$$\Phi_{\text{bar}}(x, y, z) = \frac{GM_{\text{bar}}}{2a_{\text{bar}}} \ln \left(\frac{x - a_{\text{bar}} + T_-}{x + a_{\text{bar}} + T_+} \right), \quad (9)$$

with $T_{\pm} = \left[(a_{\text{bar}} \pm x)^2 + y^2 + (b_{\text{bar}} + \sqrt{c_{\text{bar}}^2 + z^2})^2 \right]^{1/2}$ and $a_{\text{bar}}, b_{\text{bar}}, c_{\text{bar}}$ the characteristic bar parameters. The total gravitational potential generated by this model thus takes the form:

$$\Phi_{\text{tot}}(x, y, z) = \Phi_{\text{thin}}(R, z) + \Phi_{\text{thick}}(R, z) + \Phi_{\text{halo}}(r) + \Phi_{\text{bar}}(x, y, z). \quad (10)$$

with all characteristic values given in Table 1. Practically, to include the bar, we reduced the mass of the disks in such a way to maintain the total stellar mass of this model as that of PII. Long & Murali (1992) provide the formulas of the accelerations generated by this triaxial distribution in the reference frame of the bar. To calculate and add them to the accelerations generated by the disks and dark matter halo, at each time step, we converted the positions of all particles in the rotating, non-inertial reference frame of the bar, computed the corresponding accelerations on each particle, and then transformed these accelerations back in the inertial reference frame described in Sect. 2.1. In this way, the accelerations due to the bar are added to those generated by the other terms of the Galactic mass distribution.

We emphasize that we do not consider this model as the best possible representation of the Galactic mass distribution, especially in the central region. It can, however, provide a first indication on how the inclusion of a rotating asymmetric component in the inner Galaxy can affect the globular cluster streams, near and far from the Galactic center.

Moreover, since the exact characteristics of the Milky Way bar are still subject to debate (see, e.g., Bland-Hawthorn & Gerhard 2016), it is important to explore how varying the parameters adopted in this paper, such as the pattern speed, the mass, or the length of the bar, can affect the characteristics of the whole set of streams. More complex shapes for the bar can also be explored, for example, by substituting the inner parts of the triaxial bar with a boxy-peanut-shaped morphology, which has been shown to characterize the inner Milky Way (see, e.g., Wegg & Gerhard 2013; Wegg et al. 2015). These topics are, however, beyond the scope of the present paper. In sum, given the uncertainties on the bar's physical extent and how it can change over the time span investigated here, its affect on the streams presented here are purely indicative.

3. Results

A few basic premises. Given the large number of simulations carried out and the wealth of information contained in them, it is not possible to exhaust all possible applications of this simulation database in this paper. We have therefore chosen to proceed as follows.

In Sect. 3.1, we present an overview of the distribution of all streams in Galactic coordinates. This coordinate space will be the one used in the remainder of the entire article. This first section allows us to show qualitatively how the global distribution of streams varies, depending on the Galactic potential used.

We then move on (Sect. 3.2) to present the global system of streams as a function of their distance from the Sun. In this section, we also show the kinematic properties of the streams, such as proper motions and line-of-sight velocities, that can be directly compared to *Gaia* data or other astrometric and spectroscopic surveys. This section also allows us to show the variety of morphologies that the stars which escaped from globular

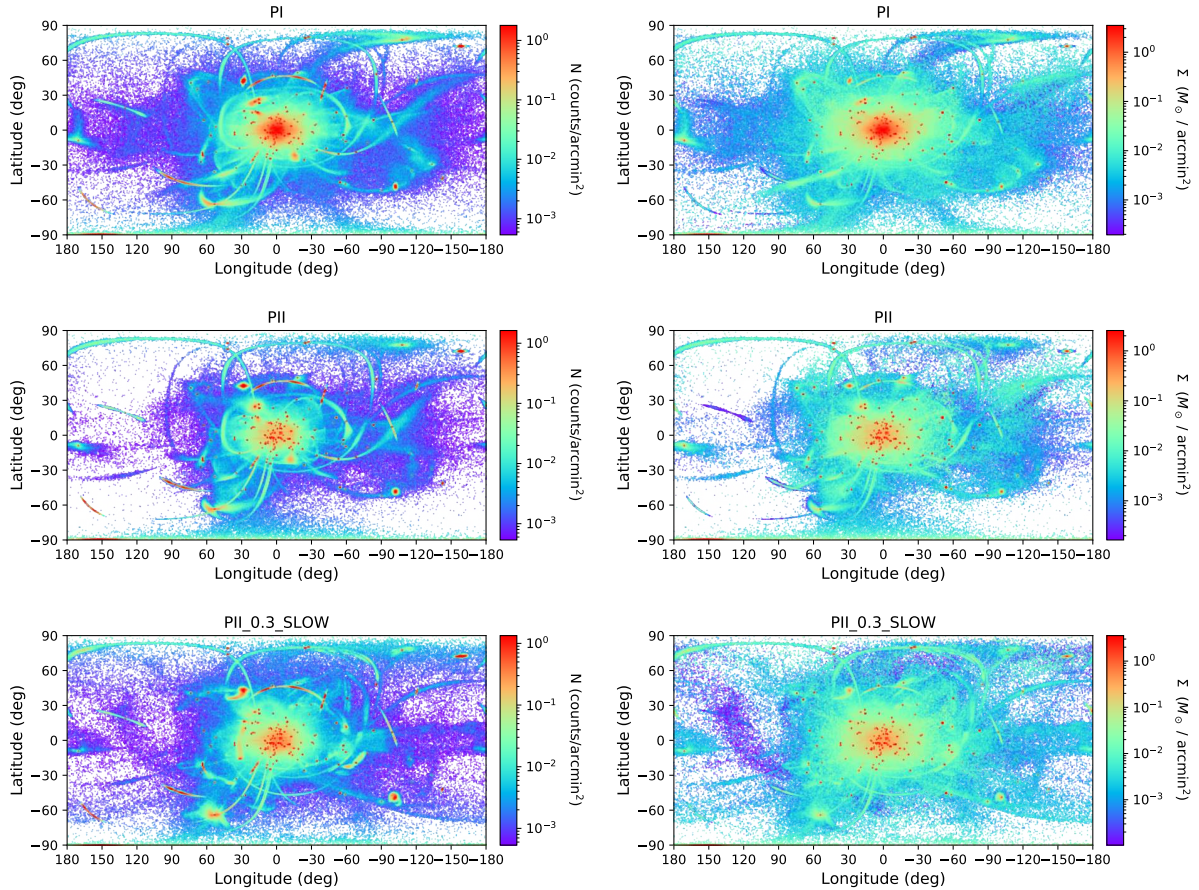


Fig. 1. Stellar surface density of the ensemble of extra-tidal features around the entire population of Galactic globular clusters at the current time, as predicted by our models. *Left:* surface number density. *Right:* surface mass density. Top row corresponds to model PI, the middle to model PII, and the bottom row to model PII-0.3-SLOW, as indicated. All densities are expressed in a logarithmic scale. The red point-like density maxima correspond to the current positions of the globular clusters. Values of higher density are overplotted. Thus in the case of mass density, diffuse tidal debris of more massive globular clusters covers the entire (ℓ, b) space and occults delicate tidal features, which are more visible when considering number density counts. In all panels, only the reference simulations are shown for clarity.

clusters can take. In Sect. 3.3, we explore this issue in more detail, showing how these morphologies depend primarily on the orbital characteristics of the clusters and their distance from the Galactic center. For the most interesting cases, we compare the tidal structures predicted by our simulations with streams found in observational data. For this purpose, we make use of the galstreams library of stellar streams in the Milky Way (Mateu 2023), which constitutes a unique and public database summarizing angular positions, distances, proper motions, and line-of-sight velocity tracks for nearly a hundred Galactic stellar streams. Any stream that is not included in this library is not compared to our simulations in the context of this paper.

We note that the tidal features associated with each of the 159 simulated clusters are presented in Appendix C. To avoid making this appendix too long, the tidal features above are presented only in the case of the potential PII. However, all the data will be made available to the community at a dedicated site⁶ where it is possible to the way the characteristics of these streams change, for any cluster, in the three chosen potentials.

3.1. A sky full of streams

Figure 1 shows the number and mass density distributions of the whole set of simulated globular clusters and their extra-tidal

features in Galactic longitude and latitude for the three Galactic potentials.

For all Galactic mass models adopted, a striking characteristic among the plots in Fig. 1 is the variety of features that our models predict, which are reminiscent of the tidal tails, stellar streams, and shells that are produced by interacting and merging galaxies in the process of mass assembly (see, e.g., Mancillas et al. 2019). Some clusters have very thin and elongated streams, which describe arcs that can extend up to 180° in longitude, or tens of kpc in physical space. In some other cases, extra-tidal features appear shorter (a few up to ten degrees) and sometimes also thicker (about 10° in the sky) than others. Finally, in some cases, clusters are surrounded by extended structures, such as halos, rather than coherent and thin streams.

This variety of properties depends on several factors: the distance of the stream to the Sun (due to projection; i.e., for a given physical thickness, the closer the stream is to the Sun, the more extended it appears in the (ℓ, b) plane), its orbital phase (towards the peri-center or the apo-center of the orbit), and the orbital properties of the parent globular cluster. We also see from these figures that stellar particles stripped from their parent clusters do not only redistribute in coherent structures, but in some cases, they can also contribute to a more diffuse density distribution.

Because of the large number of simulated clusters, we have chosen not to present the corresponding extra-tidal features one-by-one in the main part of this paper, but we have rather decided

⁶ <http://etidal-project.obspm.fr/>

to describe these extra-tidal features with a global approach, by first adopting a criterion based on the distance of these features to the Sun (see Sect. 3.2) and then discussing the types of distributions tidal debris can have and how these depend on the cluster orbital parameters (see Sect. 3.3). All the extra-tidal structures generated by the 159 globular clusters simulated in this paper, and their corresponding uncertainties, are reported in Appendix C. Among them, we include clusters with thin and elongated tails, such as IC 4499, NGC 3201, NGC 4590, NGC 5024, NGC 5053, Pal 5, to cite a few, as well as clusters such as AM 1, Pal 14, Pal 4, and Pal 15, whose extra-tidal material shows a halo-like configuration, and clusters such as NGC 1261, NGC 4147, NGC 6356, and UKS 1, whose stripped stars show a remarkable diffuse distribution in the field.

Finally, even when our models are not tailored to accurately reproduce the mass loss from globular clusters, since (as described in Sect. 2.2) we have adopted a test-particle approach with a time-constant globular cluster potential, it is however tempting to estimate, to a first order, the total mass associated with the tidally stripped population and compare it to the current mass. By calculating the mass lost in the field in the past 5 Gyr as the sum of the mass of all particles⁷ that have escaped the cluster ($t_{\text{esc}} > 0$), we find that the PI model sheds $2.1 \times 10^7 M_{\odot}$, which is 55% of the GC population's current mass. The PII model shed is $2.7 \times 10^6 M_{\odot}$, which is 7% of the current mass. Similarly, the PII-0.3-SLOW model lost $3.7 \times 10^6 M_{\odot}$, which is 10% of the current mass and gives a half mass radius of 6.3 kpc.

This mass roughly constitutes one-hundredth to one-tenth of the total stellar halo mass (Bland-Hawthorn & Gerhard 2016) and it is probably only a lower limit on the mass of escaped stars in the field, since a number of clusters initially in the Galaxy must have been destroyed over time (see introduction) and are thus no longer identifiable as globular clusters today. It is also interesting to note that escaped stars are mostly redistributed in the inner Galaxy, with the half-mass radius of the PI model being 4.0 kpc and that of the PII and PII-0.3-SLOW models being 6.3 kpc.

The total mass lost from the clusters, as well as its spatial distribution, thus depends on the Galactic potential adopted: the variations between the PI model and both the PII and PII-0.3-SLOW models are of course caused by the PI's inclusion of the bulge, which leads to larger tidal forces in the center of the galaxy and subsequently drives larger mass loss.

Despite the differences in the modeling approach, it is interesting to compare our results to those of Baumgardt & Sollima (2017). Briefly, our experiments differ in the following ways: they employ N -body simulations while we use our test-particle approach; they have an integration time of 12 Gyrs compared to our 5 Gyrs; lastly, their clusters have circular orbits in a Galactic potential modeled as an isothermal sphere as compared to the more realistic orbits and Galactic potentials considered in this work. Interestingly, the authors find that over 12 Gyrs their population of globular clusters lose two-thirds of their initial mass. This is roughly consistent with our application of the PI model, whose globular clusters shed 35% of their initial mass in 5 Gyrs, which is roughly half the mass found by Baumgardt & Sollima (2017) in a period that is also about half as long.

⁷ To estimate the mass of particles in each cluster we have quantified the number of particles, N_{bound} , bound to the cluster at the end of the simulation and calculated the corresponding particle mass as $m_p = M_{\text{GC}}/N_{\text{bound}}$, where M_{GC} is the current mass of a cluster given in Table A.1.

3.2. From the nearest to the furthest extra-tidal structures

The analysis presented in this section along with the corresponding information are given in Figs. 2–5 are restricted to the PII model.

In this section, we analyze structures located at different distances from the Sun. We identify structures as main or secondary on the basis of the fraction of stars they represent. If, for example, a cluster contributes more than 10% of its stripped stars in a given distance range, we consider the associated structure to be significant and we define it as a main structure in this distance range. If, on the other hand, the fraction of stripped stars from a cluster is between 1% and 10%, we define the associated structure as being “secondary”. Structures that constitute less than 1% of the cluster mass are considered insignificant in that range. The main and secondary structures for each distance bin are reported in Table 2, where they are named by their progenitor cluster. Below, we describe the structures encountered at different distances from the Sun, from the closest to the most distant. For the following discussions, we refer to Figs. 2–5, where we report the different streams in a given distance range (top row in each figure), the corresponding mass density generated by all the structures found in that bin (second row), the longitudinal and latitudinal proper-motions map (third and fourth rows), and the line-of-sight velocities (bottom row).

The [0–2] kpc distance range. Among the 159 simulated clusters, only NGC 6121 is currently at a distance of less than 2 kpc from the Sun. In addition to stars stripped from this cluster within this distance-to-the-Sun range, we have identified very diffuse and low density extra-tidal stars associated with five other clusters, which are currently several kpc away from the Sun, as reported in Table 2. Of these, only UKS 1 and NGC 6121 have a significant fraction of their stripped mass in this distance range. All the others contribute with only a few percent. None of these clusters seem to show well-defined, stream-like features in the (ℓ, b) plane. This extra-tidal material appears indeed quite uniformly redistributed, in a latitude range mostly inside -30° to 30° , and is mostly found at negative longitudes. Because in this interval range there is no remarkable extra-tidal structure found on the sky, we decided to plot this distance bin together with the [2–5] kpc bin (see Fig. 2, left column).

The [2–5] kpc distance range. As the distance from the Sun increases, many more tidal structures are intercepted. Eleven globular clusters are found at a distance between 2 and 5 kpc from the Sun; and together with structures emanating from these clusters, we also find extra-tidal material associated with other 48 clusters, 19 of which are significant (as listed in Table 2). Some extra-tidal structures are clearly identifiable, even when over-plotted with all the others: this is the case, for example, for the tidal material associated with the E 3 cluster, which appears as an extended thick stream (as shown in Fig. 2) at approximately -100° longitude. This is also the case for the complex tidal structure associated with BH 140, which resembles a ribbon in the sky, with a bifurcation at negative longitudes whose edges extend to about -30° and 30° latitude. In addition to these, there are a series of circular halos concentric about the Galactic center, with abrupt drop-offs in density tracing the furthest extent of diffuse debris emanating from a variety of clusters. Overall, few streams are immediately recognizable in this range, although plenty of debris is present. This is expected given that this range samples a bite of the Sun-side of the Galactic disk and that this range has a relatively small volume. In this, as in the following distance ranges, the v_{los} maps show that the tidal material at

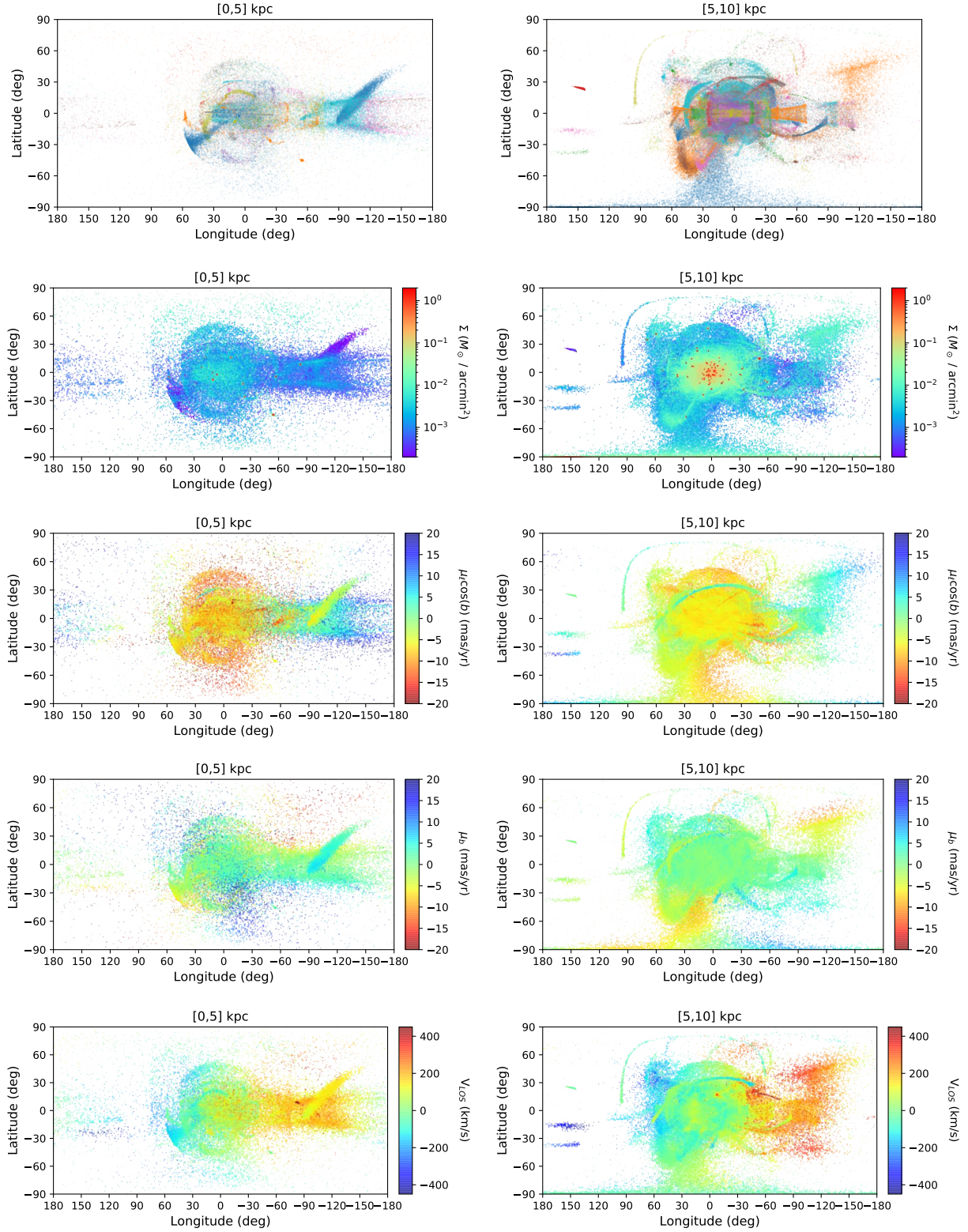


Fig. 2. Extra-tidal features colored and weighted by various quantities within limited distance bins from the Sun projected in the (ℓ, b) plane. All outputs arise from using the PII galactic potential model and only the reference simulation is shown in order to preserve clarity. *Left column:* extra-tidal features found at a distance of $[0, 5]$ kpc from the Sun. *Top row:* scatter plot, with different colors indicating different progenitor clusters. *Second row:* mass density map in logarithmic scale. *Third row:* map color-coated by proper motions in longitudinal direction. *Fourth row:* map color-coated by proper motions in latitudinal direction. *Bottom row:* map color-coded by line-of-sight velocities. *Right column:* same as left column, but for the tidal features found at a distance of $[5, 10]$ kpc from the Sun. Note: the 10 colors used in the top panels are recycled between the 159 clusters, thus, all particles from the same cluster share one color, but a color is not unique to a cluster.

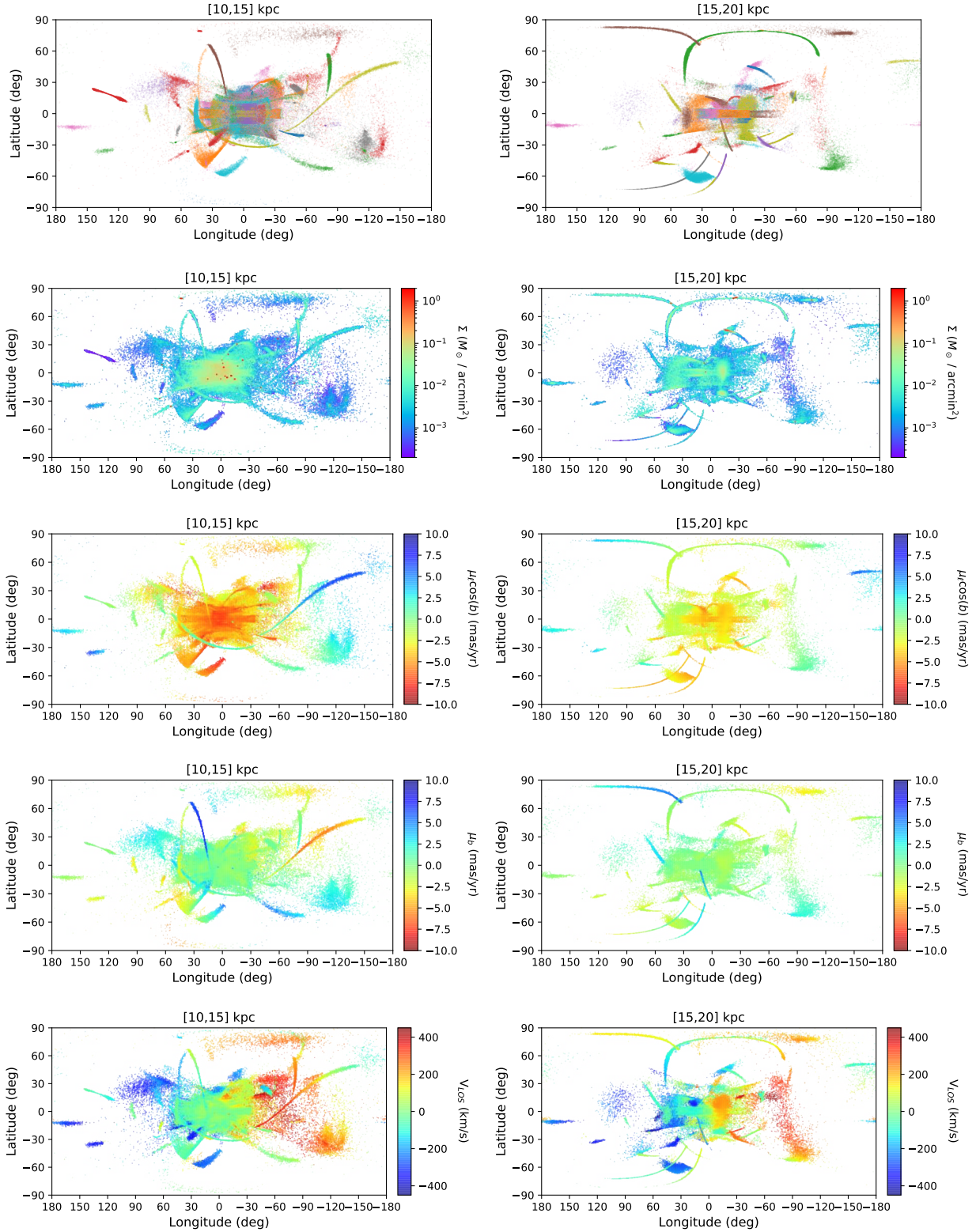


Fig. 3. As for Fig. 2, but for two father distance bins. Here, we are beyond the galactic nucleus and tidal debris are less diffuse in nature and more often stream-like. The *left column* shows debris at distances between [10, 15] kpc from the Sun while the *right column* shows debris at distances between [15, 20] kpc from the Sun.

negative Galactic longitudes has, on average, positive v_{los} while material at positive Galactic longitudes has, on average, negative v_{los} , which is due to the solar reflex velocity. This is the same trend observed for the whole set of radial (i.e., line-of-sight)

velocities in *Gaia* DR3; for instance, we refer to the bottom panel of Fig. 5 from [Katz et al. \(2023\)](#), although less extreme velocities are reported in their plot since their dataset is dominated by disk stars, whereas our maps have a high proportional

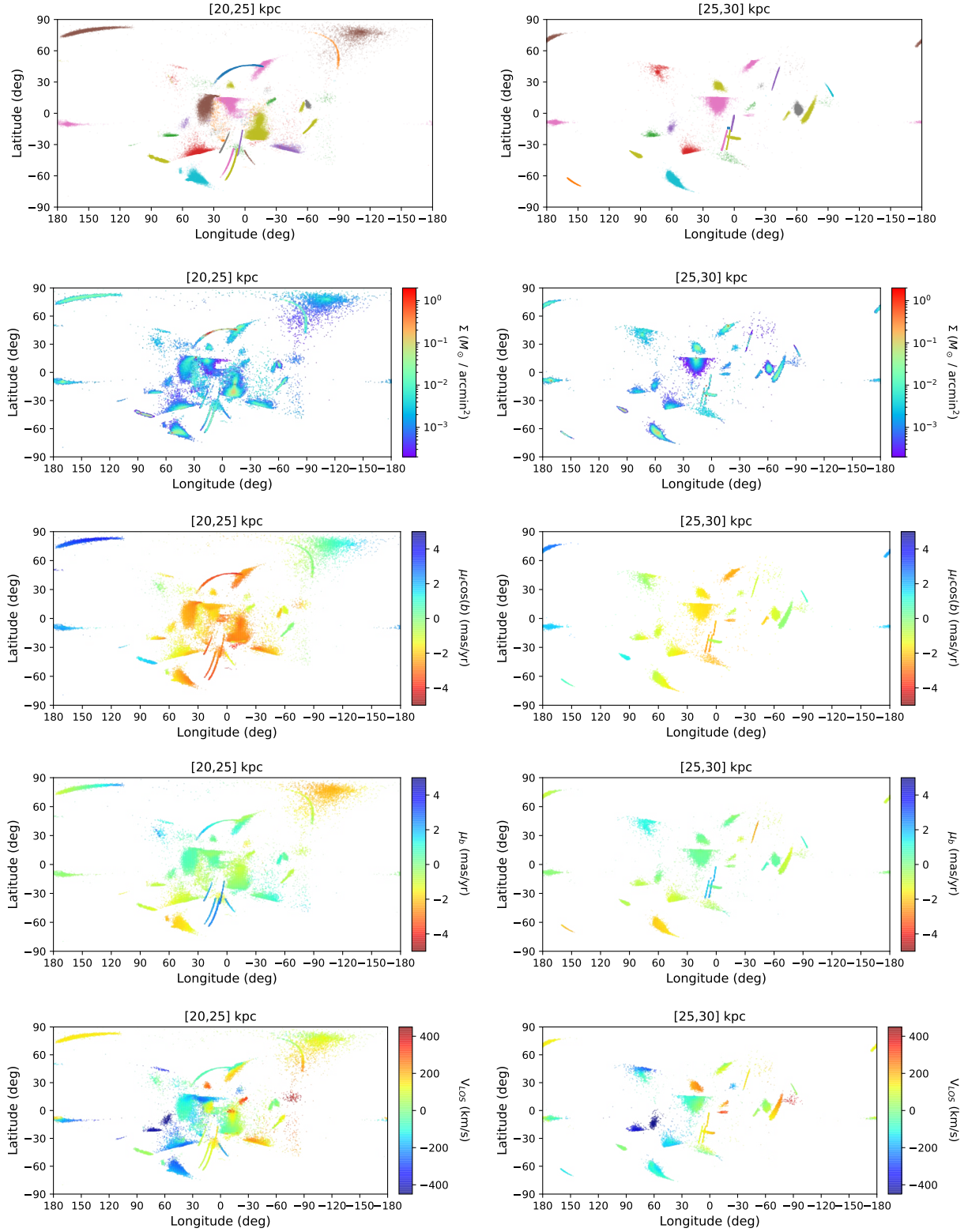


Fig. 4. As for Figs. 2 and 3, but for increased distances from the Sun. Here we notice that the tidal debris becomes more sparse as we move even farther away from the galactic center. The *left column* shows debris at distances between [20, 25] kpc from the Sun while the *right column* shows debris at distances between [25, 30] kpc from the Sun.

contribution of halo stars (additionally, they use median values in their bins, while we use an average). In order to quantify the net rotation of the system of streams, we calculated the mean angular momentum about the Galactic pole as $\langle L_z \rangle = \sum_i L_{z,i} m_{p,i} / \sum_i m_{p,i}$,

where $m_{p,i}$ is the mass of each star particle indexed by i (as discussed in footnote 7) and $L_{z,i}$ is the corresponding particle's angular momentum. The mean angular momentum is found to be $\langle L_z \rangle = -300 \text{ kpc km s}^{-1}$, which shows a slight co-rotation of the

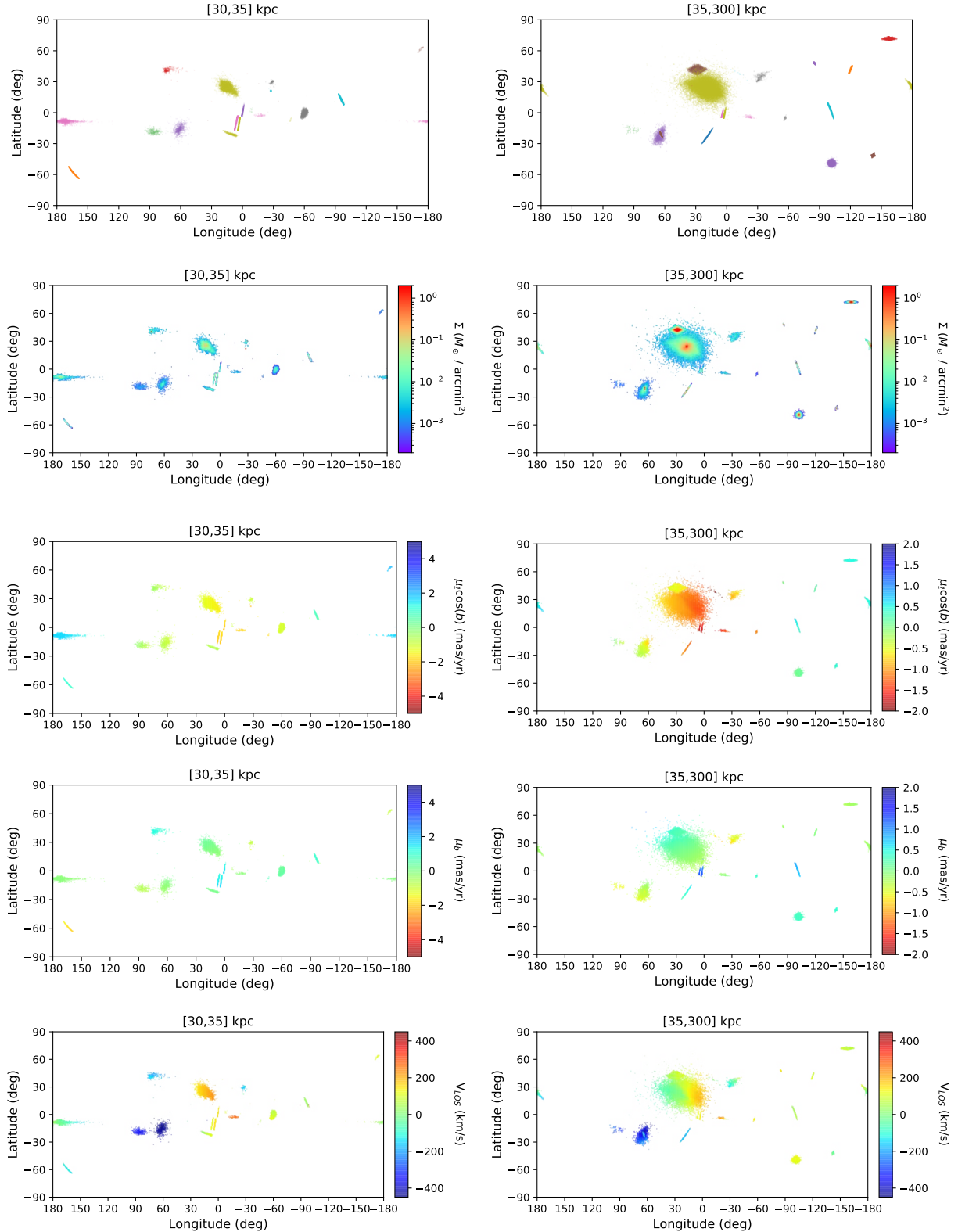


Fig. 5. As for Figs. 2–4, but now we include debris from the most outer extent of the galaxy. The *left column* shows debris at distances between [30, 35] kpc from the Sun while the *right column* shows debris at distances between [35, 300] kpc from the Sun.

system of streams with the disk though there is much dispersion about this value – as shown in bottom right panel of Fig. D.1.

The [5–10] kpc distance range. The [5–10] kpc distance range, which includes the Galactic center, contains much more material. A total of 79 clusters are found in this range, together

with tidal structures associated with 131 different progenitors redistributed among main and secondary structures. Some tiny streams are visible in the density maps as well as in proper motions and line-of-sight velocity spaces (see Fig. 2, right column): the trailing portion of the tail of the globular cluster Pal 1,

Table 2. Tidal structures found in different intervals of distance to the Sun.

Distance (kpc)	Main tidal structures	Secondary tidal structures
[0–2]	(1,2) NGC6121 , UKS1	(4) BH140, Djor1, NGC6333, NGC6356
[2–5]	(11,30) NGC6397 , NGC6544 , NGC3201 , BH140 , NGC104 , NGC6838 , NGC6366 , NGC6752 , IC1276 , NGC6656 , 2MASS-GC01 , NGC6284, NGC6356, NGC6287, VVV-CL001, NGC6254, NGC5927, E3, NGC6121, VVV-CL001, Djor1, UKS1, Ter10, 2MASS-GC02, Pal10, NGC5139, NGC6333, NGC6441, NGC6541, NGC288	(29) FSR1716, FSR1758, NGC1851, NGC1904, NGC2298, NGC2808, NGC362, NGC4372, NGC4833, NGC5897, NGC5986, NGC6205, NGC6218, NGC6235, NGC6273, NGC6316, NGC6352, NGC6388, NGC6496, NGC6681, NGC6749, NGC6760, NGC6809, NGC6864, NGC7078, Pal2, Pal8, Ter12, Ton2
[5–10]	(79,124) VVV-CL001 , NGC7099 , NGC6362 , Ton2 , Djor1 , VVV-CL001 , NGC6496 , Djor2 , NGC6535 , NGC6528 , NGC6539 , NGC6540 , NGC6553 , 2MASS-GC02 , Ter12 , BH261 , Ter9 , NGC6712 , NGC6717 , NGC6723 , NGC6749 , NGC6760 , Pal10 , HP1 , Ter4 , Ter2 , Ter3 , NGC2298 , E3 , NGC4372 , NGC4833 , NGC5904 , NGC5927 , FSR1716 , Lynga7 , NGC6144 , NGC6171 , NGC6352 , ESO452-SC11 , NGC6218 , FSR1735 , NGC6254 , NGC6256 , NGC6287 , NGC6293 , NGC6304 , NGC6355 , NGC6809 , NGC6637 , NGC6402 , NGC6325 , NGC6341 , NGC6342 , NGC6380 , NGC6401 , NGC6440 , NGC6517 , NGC6522 , NGC6541 , NGC6558 , NGC6624 , NGC6626 , NGC6638 , NGC6642 , NGC6652 , NGC6681 , Pal6 , Ter1 , Ter5 , Ter6 , NGC6333 , NGC288 , NGC362 , NGC6273 , NGC6266 , NGC6205 , NGC5139 , Liller1 , NGC5946 , NGC5897, NGC1904, NGC6752, NGC6656, NGC6121, NGC1851, NGC6864, NGC7078, NGC7089, NGC6316, NGC5272, NGC6779, NGC2808, NGC4590, Rup106, NGC104, NGC4147, NGC3201, Pal11, Pal1, NGC1261, BH140, NGC6235, Ter10, NGC6569, UKS1, NGC6453, NGC6139, NGC6426, NGC6397, NGC6093, NGC6388, FSR1758, IC1276, NGC6838, NGC6366, NGC5986, NGC6441, NGC6356, NGC6584, NGC5286, NGC6544, NGC6284, Pal8, NGC6981	(7) 2MASS-GC01, IC1257, NGC5634, NGC5694, NGC6229, NGC7006, Pal2
[10–15]	(27,115) NGC6453 , NGC5272 , NGC6584 , Pal8 , NGC6316 , NGC5897 , NGC6284 , NGC6139 , NGC6093 , NGC5986 , NGC5286 , NGC6235 , NGC2808 , NGC1904 , NGC1851 , NGC6101 , NGC6779 , NGC6388 , Pal11 , Pal1 , Ter10 , NGC4590 , NGC7089 , NGC6569 , NGC7078 , FSR1758 , NGC6441 , NGC6304, NGC6254, FSR1735, NGC6426, NGC6397, NGC6362, Ton2, NGC6256, NGC6366, NGC6287, NGC6352, NGC6355, NGC6356, NGC6218, NGC6293, VVV-CL001, NGC6171, NGC5024, NGC1261, NGC2298, E3, NGC3201, NGC4147, NGC4372, Rup106, BH140, NGC4833, NGC5053, Ter3, NGC5466, NGC5634, IC4499, NGC5904, NGC5927, FSR1716, UKS1, NGC6121, NGC6144, Lynga7, NGC6553, VVV-CL001, NGC6496, NGC5946, NGC6205, NGC6266, NGC6273, NGC6333, NGC6341, NGC6342, NGC6401, NGC6402, NGC6517, NGC6541, NGC6544, NGC6558, NGC6626, NGC6652, NGC6656, NGC6681, NGC6864, Pal6, Ter1, Ter5, NGC5139, NGC362, NGC104, Ter12, Djor2, NGC6535, NGC6528, NGC6539, NGC6540, 2MASS-GC01, Ter9, 2MASS-GC02, IC1276, BH261, NGC7099, NGC6712, NGC6723, NGC6749, NGC6752, NGC6760, NGC6809, NGC6838, NGC6934, NGC6981, NGC288	(18) Djor1, ESO280-SC06, ESO452-SC11, HP1, IC1257, NGC5694, NGC5824, NGC6229, NGC6325, NGC6380, NGC6638, NGC6642, NGC6717, NGC7006, NGC7492, Pal10, Pal2, Ter6

Notes. The tidal structures are named by their progenitor clusters. If the parent cluster is also in the distance range under consideration, the name of the tidal structure is shown in bold. Second column reports the main structures found in a given distance bin. The third column list secondary structures. The numbers in parenthesis in the second column and third column (numbers with normal font) correspond to the total number of main and secondary structures found in a given distance range. The number of clusters in each distance bin is also reported in the second column (bold numbers in parenthesis).

Table 2. continued.

Distance (kpc)	Main tidal structures	Secondary tidal structures
[15–20]	(11,46) NGC6356 , NGC5466 , NGC1261 , UKS1 , NGC4147 , IC4499 , NGC5024 , NGC5053 , Pal12 , NGC6981 , NGC6934 , NGC6101, NGC5904, Pal5, NGC5824, NGC5634, NGC7089, FSR1758, NGC4833, BH140, NGC4590, Rup106, NGC3201, Pal2, NGC5272, Djor1, NGC6426, NGC7078, NGC6864, NGC6715, NGC6656, NGC6341, NGC6333, NGC5286, NGC362, NGC2808, NGC1851, NGC104, NGC7492, Pal10, Ter7, NGC6779, NGC6584, IC1276, ESO280-SC06, NGC288	(15) 2MASS-GC02, IC1257, NGC1904, NGC2298, NGC4372, NGC5139, NGC5694, NGC6121, NGC6205, NGC6229, NGC6838, NGC7006, NGC7099, Pal13, Ter8
[20–25]	(8,29) Pal5 , NGC7492 , Pal13 , Rup106 , NGC6864 , NGC6426 , ESO280-SC06 , Ter7 , NGC5466, IC4499, NGC5634, NGC7089, NGC5824, NGC5024, NGC4590, NGC4147, NGC3201, NGC5272, IC1257, NGC5904, NGC6101, NGC6584, Arp2, Ter8, NGC6934, NGC6981, Pal12, NGC6229, Pal2	(9) Djor1, FSR1758, NGC1261, NGC1851, NGC1904, NGC2298, NGC2808, NGC5694, NGC7006
[25–30]	(7,20) NGC6715 , Pal2 , AM4 , NGC5634 , Ter8 , Arp2 , IC1257 , NGC5824, Rup106, NGC5694, IC4499, NGC6101, NGC5904, NGC6229, Ter7, NGC6934, NGC6981, Pal13, NGC7492, Whiting1	(10) NGC1851, NGC1904, NGC3201, NGC4147, NGC4590, NGC5466, NGC7006, NGC7089, Pal15, Pyxis
[30–35]	(4,11) NGC6229 , NGC5824 , NGC5694 , Whiting1 , NGC7006, Ter8, Arp2, Ter7, Rup106, Pyxis, Pal2	(3) NGC6101, NGC6934, Pal15
[35–300]	(12,15) Laevens3 , NGC7006 , SagittariusII , Pal15 , Pal14 , Crater , Pal4 , Pal3 , Pyxis , NGC2419 , Eridanus , AM1 , NGC6715, NGC5824, NGC5694	(4) Arp2, NGC6934, Pal2, Ter8

at $(\ell, b) \sim (140^\circ, 25^\circ)$; the most extreme portion of the trailing tail of NGC 3201 at $(\ell, b) \sim (150^\circ, -37^\circ)$; the waterfall-like shape of NGC 288, particularly evident at $b \lesssim -60^\circ$; the thin inverted U-shape of NGC 4590 at positive latitudes spanning a large longitude extent from $\ell \simeq -60^\circ$ to 100° ; the portion of the E 3 tails the closest to the cluster at $(\ell, b) \sim (-75^\circ, -15^\circ)$, which continues from the more easily recognizable portion in the [0–5] kpc bin.

The [10–15] kpc distance range. In the [10–15] kpc range, we find tidal structures associated with 134 progenitors, as listed in Table 2 and reported in Fig. 3 (left column), 27 of which are related to globular clusters that are also found in this distance bin. We note that at these distances from the Sun, the distribution of tidal features in directions towards the Galactic center, from -30° to 30° longitude, appears less fuzzy than the one characterizing the [0–5] and [5–10] kpc distance bins. Tidal features here are beyond the Galactic center, and are mostly associated with disk or halo clusters.

Among the thinnest structures, we find the stream associated with Pal 1, at $(\ell, b) \sim (120^\circ, 15^\circ)$, which is also visible in the distance bin [5–10] kpc (see previous discussion), but which is even more elongated here. NGC 6101 shows the nearest portion of its long thin diagonal tidal tail that spans negative longitudes and ranges from -15° to 45° latitude. Additionally, this stream is also unique against its counter parts in proper motion space. NGC 5053’s nearest portion appears as a vertical tidal tail at -80° longitude. Similarly, NGC 5466 is shown vertically at 25° longitude.

Among the thickest structures, we can recognize general diffuse and bowtie-like shapes. There are also spoke-like structures departing radially from the Galactic center. For instance, we can associated the extra-tidal material with NGC 7078 at $(\ell, b) \sim$

$(60^\circ, -28^\circ)$, as well as NGC 7089, which is nearly parallel to the previous structure, but at lower latitudes at $(\ell, b) \sim (50^\circ, -40^\circ)$.

The [15–20] kpc distance range. At larger distances ([15–20] kpc range, see Fig. 3), some of the most striking features are associated with the clusters NGC 5024 and NGC 5053, whose long thin tails essentially overlap in this distance, with the latter covering the former, and appearing at high latitudes spanning a longitudinal range from $\ell \sim -90^\circ$ to $\ell \sim 45^\circ$. Again, the long thin stream of NGC 5466 appears in this range (as will be the case for the next) and is at high latitudes at roughly 85° and positive longitudes. There is also the thicker extended structure of NGC 4147 whose diffuse structure emanates from about $(\ell, b) \sim (-100^\circ, 80^\circ)$.

In this distance bin, we find long tidal tails emanating from globular clusters associated with the Sagittarius dwarf galaxy, which are particularly visible at negative longitudes: a long thin stream is associated with Pal 12 at positive longitudes and latitudes $b \leq -15^\circ$, as well as two overlapping structures at $0^\circ \lesssim \ell \lesssim 30^\circ$ longitude, namely, Ter 7 (and Ter 8 in the next distance bin). A word of caution is needed here: the mass loss from these clusters may be incorrect, since we do not include the presence of the Sagittarius dwarf galaxy itself. The potential well associated with this latter could change the tidal effects experienced by clusters associated with Sagittarius, especially in the case of NGC 6715, which sits at the center of this dwarf galaxy. The inclusion of the Sagittarius dwarf will be the subject of future investigations. Overall, in this distance bins, we find 11 clusters and 61 streams, all listed in Table 2.

The [20–25] and [25–30] kpc distance ranges. In the following distance bins (at [20–25] kpc and [25–30]; see Fig. 4), globular clusters and extra-tidal structures become less numerous, although some are still visible, such as Pal 5 at

$(\ell, b) \sim (0^\circ, 45^\circ)$. In more detail, in the [20–25] kpc bin we find tidal features associated with 37 different progenitors, 8 of which are associated with globular clusters whose current positions are in the same distance bin; in the [25–30] kpc bin, 7 clusters are found, together with tidal features associated with 30 other progenitor clusters which do not lie in this same distance range. In both bins, the streams emanating from globular clusters associated with the Sagittarius dwarf galaxy are still visible, as well as the most extreme portion of the tail associated with NGC 5466.

The [30–35] and [35–300] kpc distance ranges. Finally, in the last distance bins (see Fig. 5), thin streams become rare. Some small streams are visible: Pyxis at $(\ell, b) \sim (-100^\circ, 0^\circ)$; NGC 2419 at $(\ell, b) \sim (-180^\circ, 30^\circ)$; Pal 4 at $(\ell, b) \sim (-160^\circ, 75^\circ)$; Pal 3 at $(\ell, b) \sim (-120^\circ, 45^\circ)$. Many more have a diffuse and halo-like structure. For instance, the blob associated with Pal 15, centered at $(\ell, b) \sim (15^\circ, 20^\circ)$; AM 1 at $(\ell, b) \sim (-100^\circ, -55^\circ)$; Eridanus at $(\ell, b) \sim (-140^\circ, -45^\circ)$; Pal 14 at $(\ell, b) \sim (30^\circ, 45^\circ)$; Laevens 3 at $(\ell, b) \sim (65^\circ, -20^\circ)$, which is completely enveloped by NGC 7006. In total, in these two distance bins, we find 4 and 12 clusters, respectively, along with their associated streams, together with extra-tidal material associated with 14 and 19 progenitors in total.

3.3. Disks of inner and outer halo clusters: A variety of morphologies and shapes for extra-tidal structures

The analysis presented in the previous section allows us to appreciate the variety of morphologies found for extra tidal structures, from padlocks to “Easter eggs”, disks, ribbons, and canonical streams. Moreover, some structures are limited in latitude and longitude, while some others fill nearly the entire sky.

To more easily capture the similarity and differences in the morphology of the extra-tidal features surrounding Galactic globular clusters, we can group the latter on the basis of their orbital parameters⁸ (see Appendix D for more details), as follows: Disk clusters: A cluster is classified as a disk cluster if $\arctan(z_{\max}/R_{\max}) \leq 10^\circ$, where z_{\max} and R_{\max} are, respectively, the maximum height above or below the Galactic plane reached by its orbit in the last 5 Gyr and its maximum in-plane distance from the Galactic center; Inner clusters: All clusters with $r_{\max} \leq R_\odot$ that are not classified as disk clusters enter this group. Contrary to R_{\max} , which is the maximum in-plane distance that a cluster reaches from the Galactic center, r_{\max} is the maximum 3D distance, that is, $r_{\max} = \max(\sqrt{R^2 + z^2})$, with the maximum calculated over the whole cluster orbit; Outer clusters: All clusters with $r_{\max} > R_\odot$ that are not classified as disk clusters are included in this group.

By using the orbital radius of the Sun as the criterion for inner and outer clusters, debris from outer clusters can span the whole sky while inner clusters must be restricted in longitude and latitude. With these definitions, 21 clusters are disk clusters, 71 are inner clusters, and 67 are outer clusters (see Table D.1). We emphasize that this classification does not aim to suggest any specific origin for these systems (e.g., whether they are in-situ or accreted, see Massari et al. 2019), but it is uniquely based on their current orbital characteristics and helps in capturing some of the properties in the extension (projected in to

the sky) and shape of their extra-tidal material, as we discuss in the following.

3.3.1. Extra-tidal features originating from disk clusters: ribbons in the Galactic plane

Disk clusters are defined on the basis of the flatness of their orbits (i.e., on their z_{\max}/R_{\max} ratio). As a result, they typically are restricted to low latitudes, though the exact distribution depends on the relationship of their orbit to the solar radius. To specify, clusters whose R_{\max} are interior to the Solar radius generate tidal debris in a limited range in longitude and latitude. For instance, the material associated with clusters as Ter 1, Ter 5, Ter 6, and Ter 9 has a disk-like shape and is completely confined to $|\ell| < 30^\circ$ and $|b| < 10^\circ$. If R_{\max} is greater than the solar radius, material can cover the full longitude space and most of the material will still appear at low latitudes. This is the case, for example, of BH 140, whose escaped stars diffusely occupy all longitudes and most of them are found at $|b| \leq 30^\circ$, while for Pal 2 and Pal 10, their extra-tidal stars have a very limited latitudinal extension and appear as ribbons in the sky. In the following, we discuss some of the structures associated with NGC 6121, Pal 2, and Pal 10. We refer to Appendix C for the tidal structures generated by the whole set of disk clusters.

NGC 6121. With a current position at $x = -6.58$, $y = -0.28$ and $z = 0.53$ kpc, NGC 6121 is the closest globular cluster to the Sun in our list. This cluster has a remarkably planar orbit, with a maximal vertical excursion from the Galactic plane of only 0.5 kpc (see Fig. 6), and an eccentricity $e = 0.80 \pm 0.01$, which makes it oscillate between an apo-center at $R_{\max} = 6.81 \pm 0.02$ kpc and a peri-center at $R_{\min} = 0.76 \pm 0.04$ kpc. Because this cluster lies inside the solar circle, its orbit is limited to a longitude interval from -60° to 60° ; because the cluster currently lies very close to the Sun, and is at its highest height above the Galactic plane, the orbit forms a hook-like pattern in longitude-latitude space. This hook-like portion of the orbit, nearest to the cluster, is traced by the recently stripped tidal material (see Fig. 6), with a leading tail oriented mostly in a vertical direction in the (ℓ, b) plane, from the current cluster location, up to approximately 0° latitude. This portion of the stripped material lies at less than 2 kpc from the Sun, and it constitutes the nearest stream found in our simulations.

To our knowledge, no extra-tidal structure has been discovered around NGC 6121 thus far. Recently, Kundu et al. (2019) used RR-Lyrae stars to trace the extra-tidal material around NGC 6121, without finding any clear evidence of structures. The current position of the cluster in the sky, at a latitude of roughly 20° and at a longitude close to 0° , makes this search difficult due to the strong contamination of field disk stars, despite the fact that this portion of the stream is expected to be very close to the Sun.

Pal 10 and Pal 2. Pal 10 and Pal 2 are two disk clusters whose orbit crosses the solar radius. While for Pal 10, the maximal in-plane distance, R_{\max} , is approximately 12 kpc, in the case of Pal 2, the orbit can reach about 40 kpc from the Galactic center. The fact that both these clusters have a radial excursion of the orbit which is beyond the solar radius implies that their stripped stars can redistribute over the whole longitudinal range and, thus, is also in the anti-center direction. The fact that both clusters have orbits confined close to the disk plane implies that the escaped material redistributes in very thin structures (i.e., confined in a limited latitude interval), which resemble typical “ribbons” in the sky. Our models predict that both clusters are

⁸ We caution the reader that the classification of disk, inner and outer clusters made in this section is based on the orbital parameters of the clusters, as found when their orbits are integrated in model PII. This classification may slightly change if model PI or model PII-0.3-SLOW were adopted.

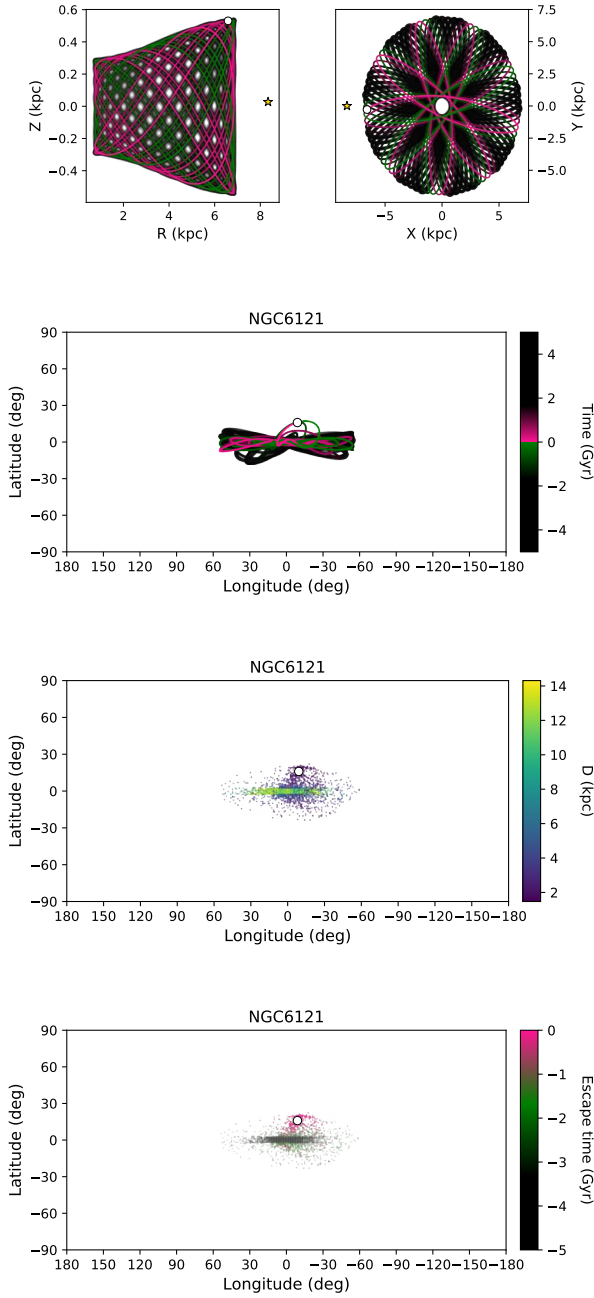


Fig. 6. *Top-left panel:* projection of the orbit of NGC 6121 in the meridional $R - z$ plane. Colors trace time, from 5 Gyr ago (negative values) to 5 Gyr forward in time (positive values). *Top-right panel:* projection of the orbit of NGC 6121 in the Galactic $x - y$ plane. *Second panel:* projection of the NGC 6121 orbit for the past and future 5 Gyr, in the longitude-latitude plane. *Third panel:* projection in the longitude-latitude plane of the extra-tidal material lost by NGC 6121. Colors indicate the average distance of the stripped material from the Sun. *Bottom panel:* projection in the longitude-latitude plane of the extra-tidal material lost by NGC 6121. Colors indicate the average time at which stellar particles become gravitationally unbound to the cluster, from 5 Gyr ago (negative time) to the current time (escape time = 0). In the bottom and middle panels, only the reference simulation without errors is shown for clarity. In all plots, the current position of the cluster is given by the white circle with a black outline. The yellow star, when present, indicates the position of the Sun.

surrounded by a long stream of tidal material, which is however probably very difficult to identify because in both cases, these

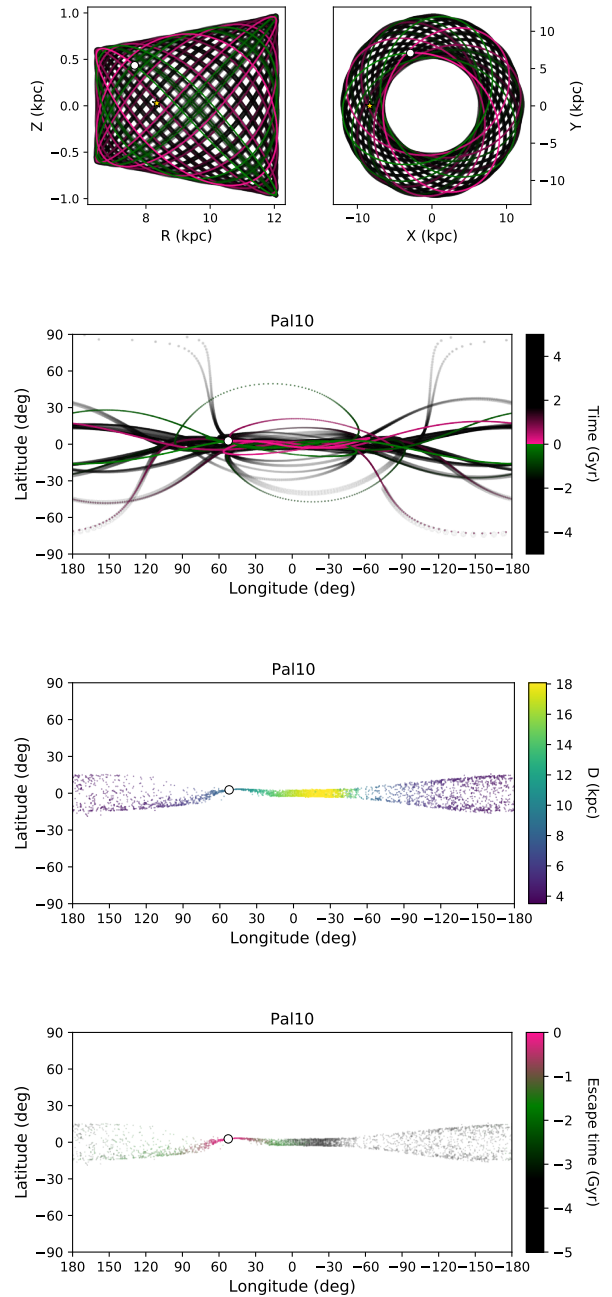


Fig. 7. Various projections of the host globular cluster orbit with its accompanying tidal debris as Fig. 6, but for the cluster Pal 10.

extra-tidal stars are confined close to the Galactic plane. No tidal streams emanating from these two clusters, to our knowledge, have been identified in the observational data so far. Because the tidal structures associated with these two clusters have similar properties, we report only the case of Pal 10 in Fig. 7.

3.3.2. Extra-tidal features originating from inner clusters: Bow-ties and more complex shapes

We have defined inner globular clusters as systems that are not disk clusters (their orbit is not confined close to the Galactic plane) but that are confined inside the solar radius. Seventy-one clusters are found in this category (see Table D.1). We discuss some of them in the following.

NGC 5946 & NGC 5986. These are inner-non disk clusters whose escaped stars redistribute in a characteristic “bow-tie” shape. These stars are all confined in a relatively narrow longitudinal range (typically within -30° to 30°). Towards the edges of the longitude interval, the distribution of extra-tidal stars tends to flare, whereas it instead shrinks at zero longitude. These trends can be explained as an effect of the projection of the orbits of these clusters in the (ℓ, b) plane. Moreover, because these clusters always stay in the inner region of the Galaxy, where the dynamical timescales are short, their orbit – and consequently their stripped stars – can experience many disk crossings over the whole duration of the simulation, filling the whole (ℓ, b) space allowed by their orbital parameters. An example of such a distribution is given in Fig. 8 for the extra-tidal material associated with the cluster NGC 5986.

NGC 104. There are also clusters such as NGC 104 (47 Tuc) for which the morphology of the extra-tidal material can take on more complex shapes. This cluster has an orbit confined inside the solar radius, but which, at its apocenter, can reach a distance of less than 1 kpc from the Sun (see Fig. 9). The projection of the past and future orbit in the (ℓ, b) plane gives rise to a kind of figure-eight shape, with the stars stripped more recently from the cluster tracing the portion of this shape that extends to negative latitudes. Our model of NGC 104 is in agreement with the conclusions reached by Lane et al. (2012), who suggested that two clear tidal tails should emanate from this cluster, however, the orientation of these tails in the (ℓ, b) plane differs slightly between the two works. The models of Lane et al. (2012) do indeed suggest that the leading tail of NGC 104 should extend a bit beyond $\ell < -70^\circ$ (see Fig. 4 in their paper, as an example), while our model predicts a minimum longitude of about -60° . The exact comparison between these two works is however difficult, since the model of the Galactic potential, the distance to the Sun, proper motions, and line-of-sight velocities of NGC 104 used in their study are different from ours. To date, clear tails around NGC 104 have not been found yet, with the most recent observational works pointing to the possibility of the presence of a diffuse extended halo-like structure around this cluster (see Piatti 2017). We note that we only find a more diffuse distribution of extra-tidal material in the case of the PII-0.3-SLOW model. Additional work for comparing the current observational data with simulations will be needed to resolve this apparent discrepancy between theoretical predictions and observational findings.

Other shapes found in this category include “Easter eggs”, which are generated by clusters whose orbits are confined to the innermost kpc of the Galaxy and show significant variations in the z -coordinates that are at least as large as those found in the radial direction. Among clusters whose extra-tidal material shows these peculiar shapes we have found: HP1, NGC 6093, NGC 6273, NGC 6293, NGC 6723, and NGC 6809.

3.3.3. Extra-tidal features originating from outer clusters: “canonical” tidal tails

Caveat. In this group, there are some elongated streams emanating from such clusters as NGC 6715, Pal 12, Ter 7, and Ter 8, which are associated with the Sagittarius dwarf galaxy. As a caution, we add that for these clusters the elongation and shape of the streams may be severely modified if the gravitational potential generated by the Sagittarius dwarf galaxy itself was included in the model. For completeness, we decided to include these streams in the paper, and to report them in Appendix C. In future

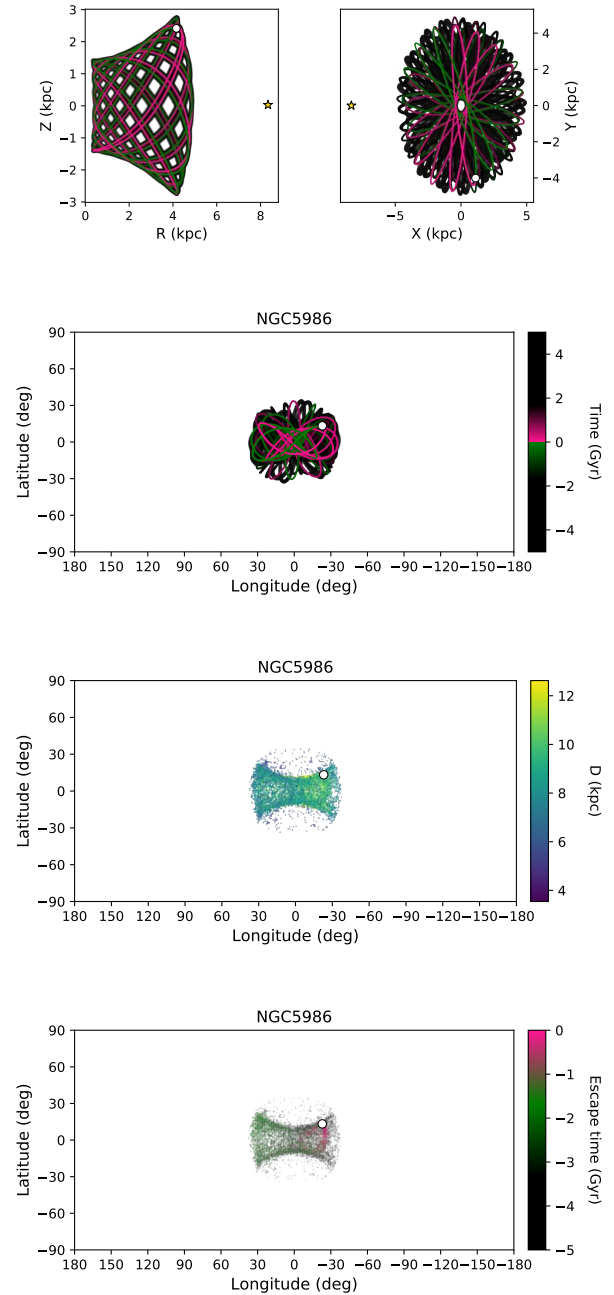


Fig. 8. Various projections of the host globular cluster orbit with its accompanying tidal debris as in Figs. 6 and 7, but for the cluster NGC 5986.

works, we plan to investigate how the inclusion of the Sagittarius dwarf may alter these streams and possibly affect also those of other clusters that are not necessarily associated with this dwarf galaxy.

Among the extra-tidal structures emanating from outer globular clusters, we find some of the most beautiful and elongated tidal tails, of which those associated with Pal 5 were the first to be discovered (Odenkirchen et al. 2001). In this category, we note the stream associated with the E 3 cluster that extends about 120° in longitude based on our models prediction; the thin stream emanating from IC 4499, which we predict has an extension of about 150° in longitude. To recap, the finest and thinnest stellar streams have been predicted from: AM 4, Arp 2, IC 4499, NGC 1261, NGC 3201, NGC 4590, NGC 5024,

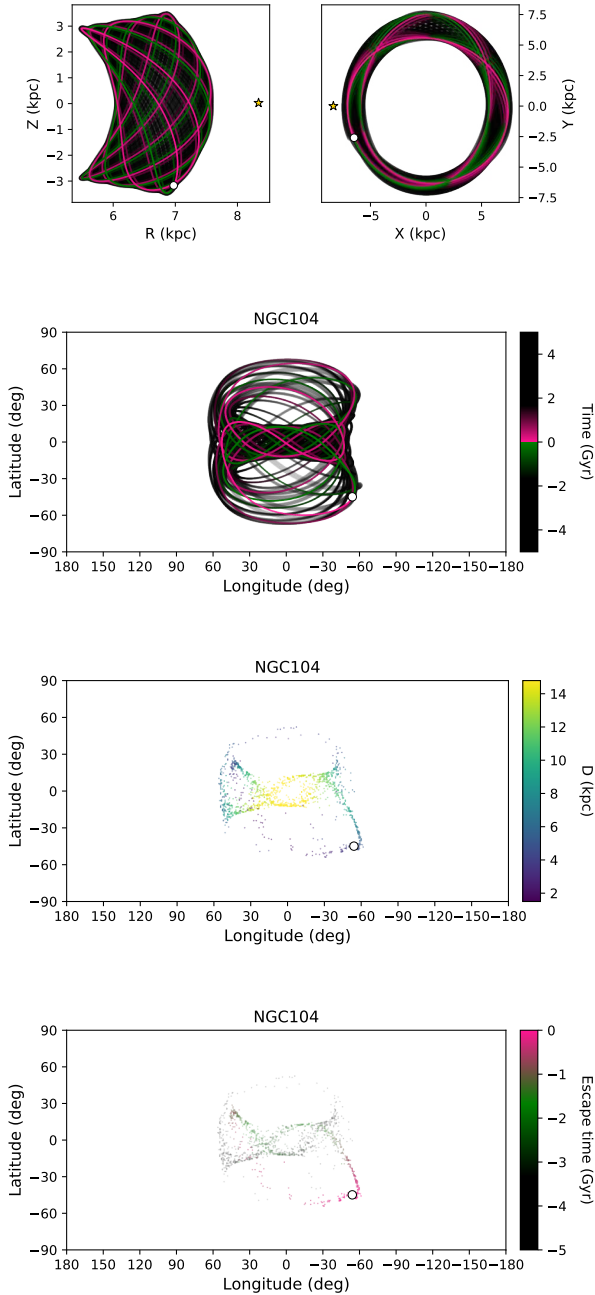


Fig. 9. Various projections of the host globular cluster orbit with its accompanying tidal debris as in Figs. 6–8, but for the cluster NGC 104.

NGC 5053, NGC 5272, NGC 5466, NGC 5694, NGC 5824, NGC 5904, NGC 6101, NGC 6426, NGC 6584, NGC 6934, Pal 1, Pal 5, Pyxis, Rup 106, Sagittarius II, Ter 7, Ter 8, and Whiting 1.

Many of the above-cited streams have been discovered and also found in observational data, but in many cases, the extent of the tails, as predicted by our models, is larger. Of these observed streams, many tracks are available in the galstreams (Mateu 2023) library. In the following, we compare our model predictions to some of these tracks in the three different Galactic potentials adopted in this paper. More specifically, we compare the projected density distribution of the simulated stream to observations in the (ℓ, b) , $(\ell, \mu_\ell \cos(b))$, (ℓ, μ_b) , and (ℓ, D) planes. As for the projected density distributions derived from the models, we calculated them by taking into account all the 51 simulations

realized for each cluster, that is, both the reference simulation and those realized by a Monte-Carlo sampling of the uncertainties. Overall, the agreement between models and observational data is excellent for all Galactic models used. By looking at more extended regions in the sky than those covered by current observations, it should be possible to better constrain the streams, as well as favor or otherwise disfavor some of these models.

NGC 3201. NGC 3201 is an outer cluster at a distance of about 4.7 kpc from the Sun. It has received a great deal of attention in the last couple of years, following the suggestion by Riley & Strigari (2020) that part of its tidal tails could be associated with the Gjöll stream, discovered by Ibata et al. (2019b). The association of the Gjöll and NGC 3201 streams has been further confirmed by Hansen et al. (2020) on the basis of the similarity of the chemical abundances of stars in the Gjöll stream and in NGC 3201. More recently, Palau & Miralda-Escudé (2021) conducted an extensive study of the tidal tails emanating from this cluster, discovering a long stream, with an overall length of 140° in the sky. Our models suggest that the tails emanating from NGC 3201 may, in fact, be even more extended than those found by Palau & Miralda-Escudé (2021). To further illustrate this point, in Fig. 10 we compared our model predictions to the tracks available for this stream in the galstreams library as well as those taken from Ibata et al. (2021), from Palau & Miralda-Escudé (2021), and from the Gjöll stream, as reported by Ibata et al. (2021). All models represent the portion of the stream discovered so far very well, specifically, in terms of the distribution of the stream in the sky, distance, and proper motion spaces. Our models indeed predict that for this cluster, the differences in the stream properties change very little with the mass model adopted. The most striking difference is found for the elongation of the stream at $\ell > 0$: in the case of the barred potential, the stream associated with NGC 3201 does extend to smaller values of ℓ (up to $\ell \sim 70^\circ$), which are not reached in the case of the axisymmetric models. This portion of the stream is expected to be found at distances greater than 20 kpc from the Sun (see bottom panels in Fig. 10).

NGC 4590. NGC 4590 (M 68) is an outer cluster at a current distance of about 10 kpc from the Sun. This cluster is surrounded by a very extended stream (Palau & Miralda-Escudé 2019; Ibata et al. 2021), a long portion of which is represented by the Fjörm stream, discovered by Ibata et al. (2019b). The comparison between our model predictions and the tracks available in galstreams is shown in Fig. 11. Interestingly (and differently from the case of NGC 3201), not all the Galactic potentials adopted in this paper seem to represent the stream distribution in the sky equally well. While the axisymmetric models PI and PII predict generally a good match – with model PI describing the stream at positive longitudes even more accurately than model PII – the model PII-0.3-SLOW fails to reproduce the stream in its observed extension: the modeled stream in this case appears quite thick in the (ℓ, b) plane and, moreover, it is much shorter than the stream found in the observational data. Interestingly, the axisymmetric models capture very well also the proper motions and distance-to-the-Sun trends as a function of longitude, as found by Ibata et al. (2021; for Fjörm) and by Palau & Miralda-Escudé (2019), while the NGC 4590 as reported by Ibata et al. (2021; and named “M68-I21” in Fig. 11) tends to be off in all models – and also off when compared to the other observational tracks. As suggested by Mateu (2023), it is possible that the stellar stream that was associated with NGC 4590 by Ibata et al. (2021) does indeed have a different progenitor. Finally, the failure of the barred model to reproduce

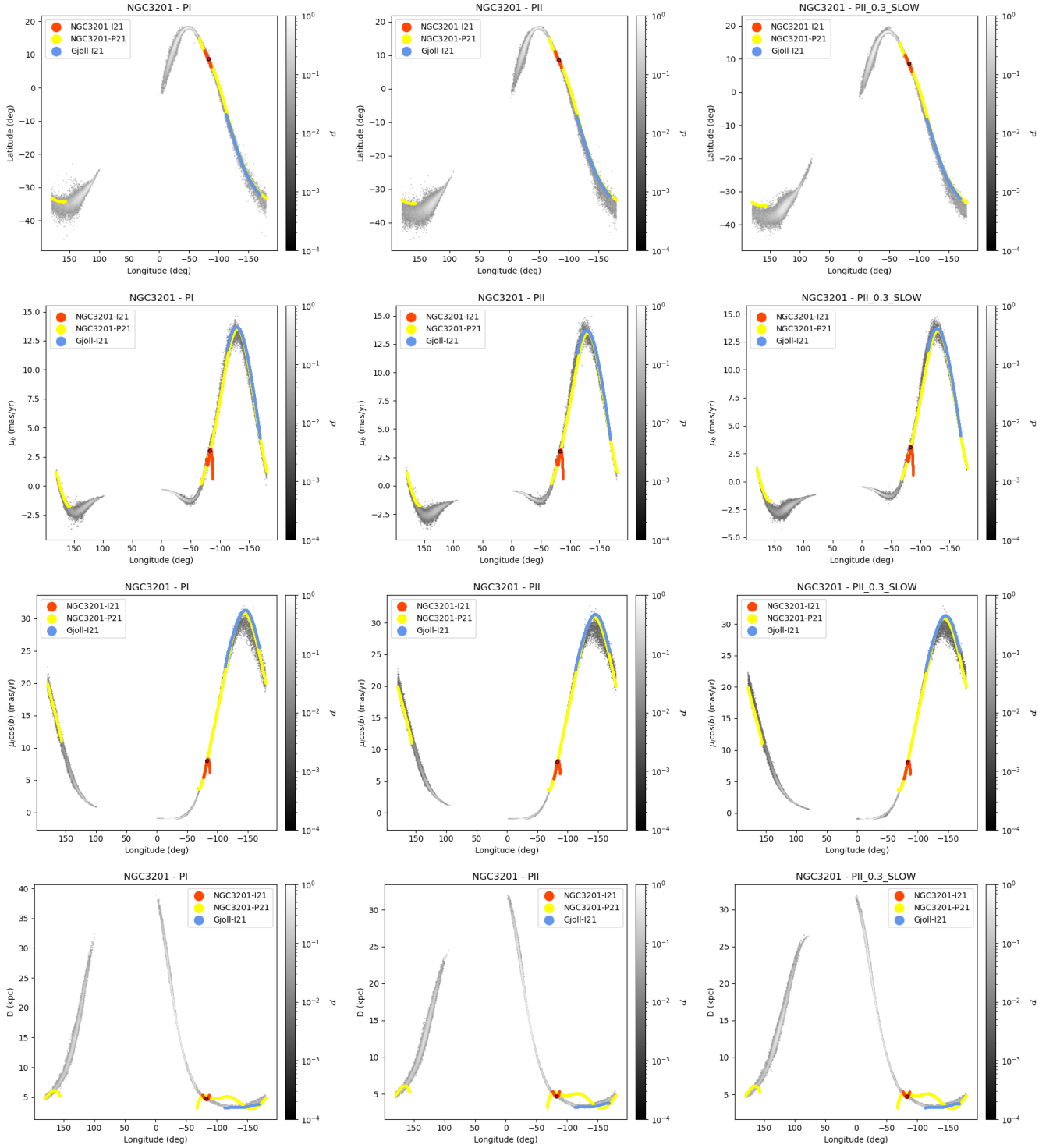


Fig. 10. Projected density distribution of the NGC 3201 stream, as predicted by our simulations, in the (ℓ, b) , (ℓ, μ_b) , $(\ell, \mu_\ell \cos(b))$ and (ℓ, D) planes, shown from top to bottom. The model predictions are shown for the three Galactic potentials PI (left column), PII (middle column), and PII-0.3-SLOW (right column) and are compared to the tracks available in the galstreams library for this cluster, and which are taken from [Ibata et al. \(2021, NGC3201-I21, red lines\)](#), [Palau & Miralda-Escudé \(2021, NGC3201-P21, yellow lines\)](#) and from [Ibata et al. \(2021\)](#), as for the Gjöll stream (Gjöll-I21, blue lines). For each panel, the color bar indicates the 2D probability density quantified by taking into account all the particles from the 51 realizations, which is then normalized to its maximum value. In all panels, the current position of the cluster is indicated by a red dot.

the extension of the NGC 4590 stream (and in particular Fjörm) might be due to the choice of the pattern speed adopted or that of the bar length. We will explore these topics in future work. Here, we simply note that given the sensitivity of NGC 4590 stream to the choice of the barred potential, this stream is poten-

tially very interesting for determining the parameters of the latter.

NGC 5466. NGC 5466 is another cluster known to be surrounded by a thin and very extended stream, as shown by [Grillmair & Johnson \(2006\)](#) and [Belokurov et al. \(2006\)](#). More

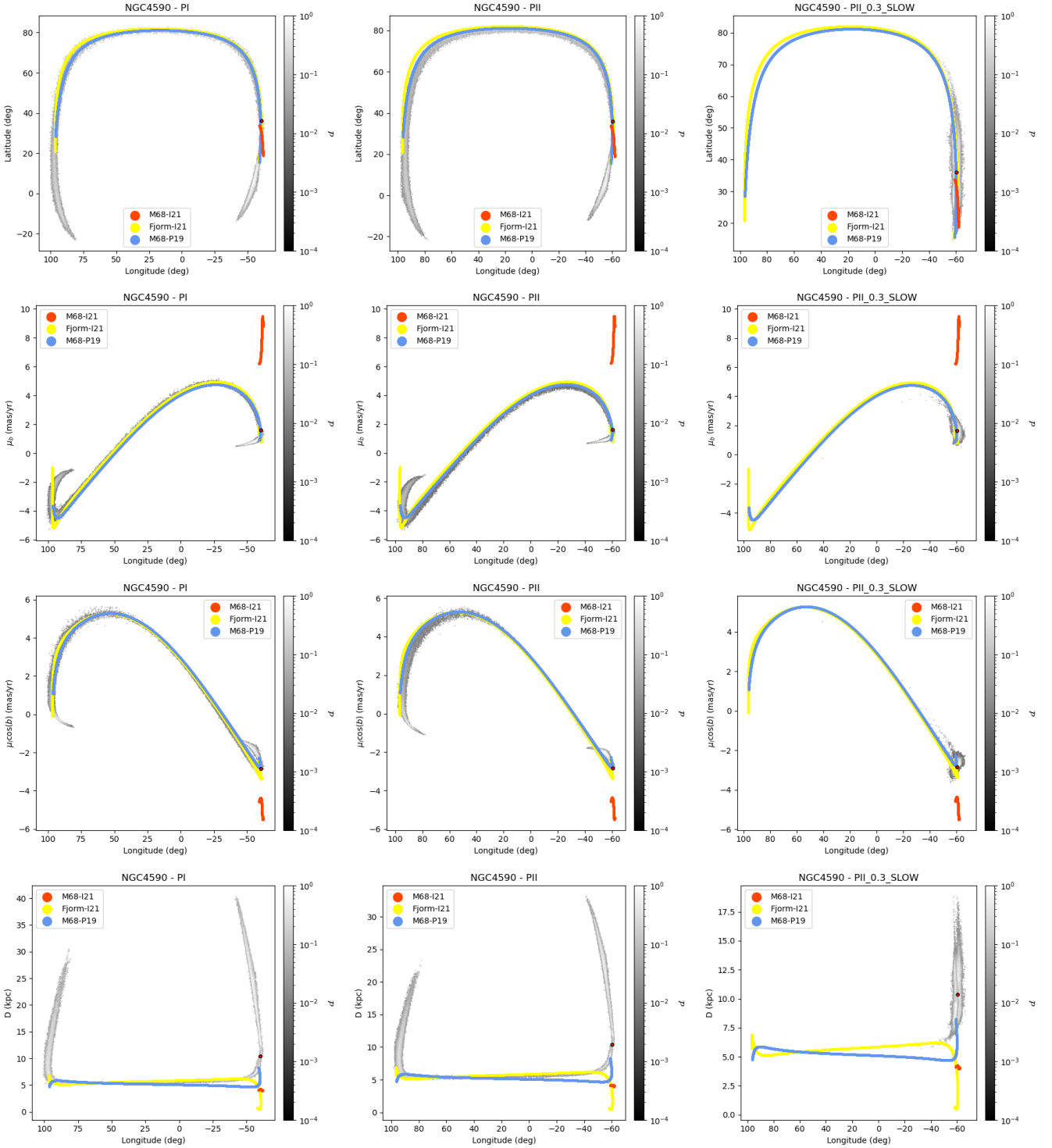


Fig. 11. Probability density maps arising from our simulations plotted against observed stellar streams as in Fig. 10, but for the NGC 4590 cluster. The tracks come from the work by Palau & Miralda-Escudé (2019, M68-P19, blue lines), Ibata et al. (2021, M68-I21, red lines) and from Ibata et al. (2021) as for the Fjorm stream (Fjorm-I21, yellow lines).

recently, Jensen et al. (2021) used *Gaia* DR2 data to study the stream, finding an extension of about 30 degrees on the sky and a somewhat different orientation than that suggested by Grillmair & Johnson (2006). Also, Ibata et al. (2021) confirmed the existence of an elongated stream around this cluster, even if it appears somewhat less extended than what was found by Grillmair & Johnson (2006). In Fig. 12, we show the comparison of our model predictions to the tracks available in gal-

streams, taken from the works by Grillmair & Johnson (2006) and Ibata et al. (2021). The comparison is excellent for all the Galactic potentials used in this paper. We note that there is a slight offset between the modeled streams and the track by Ibata et al. (2021) in the $(\ell - D)$ plane (of about 1 kpc at a fixed longitude) – which is maybe less evident for the case of the PII-0.3-SLOW potential than in the axisymmetric cases. We emphasize that all our models predict that the stream should be more

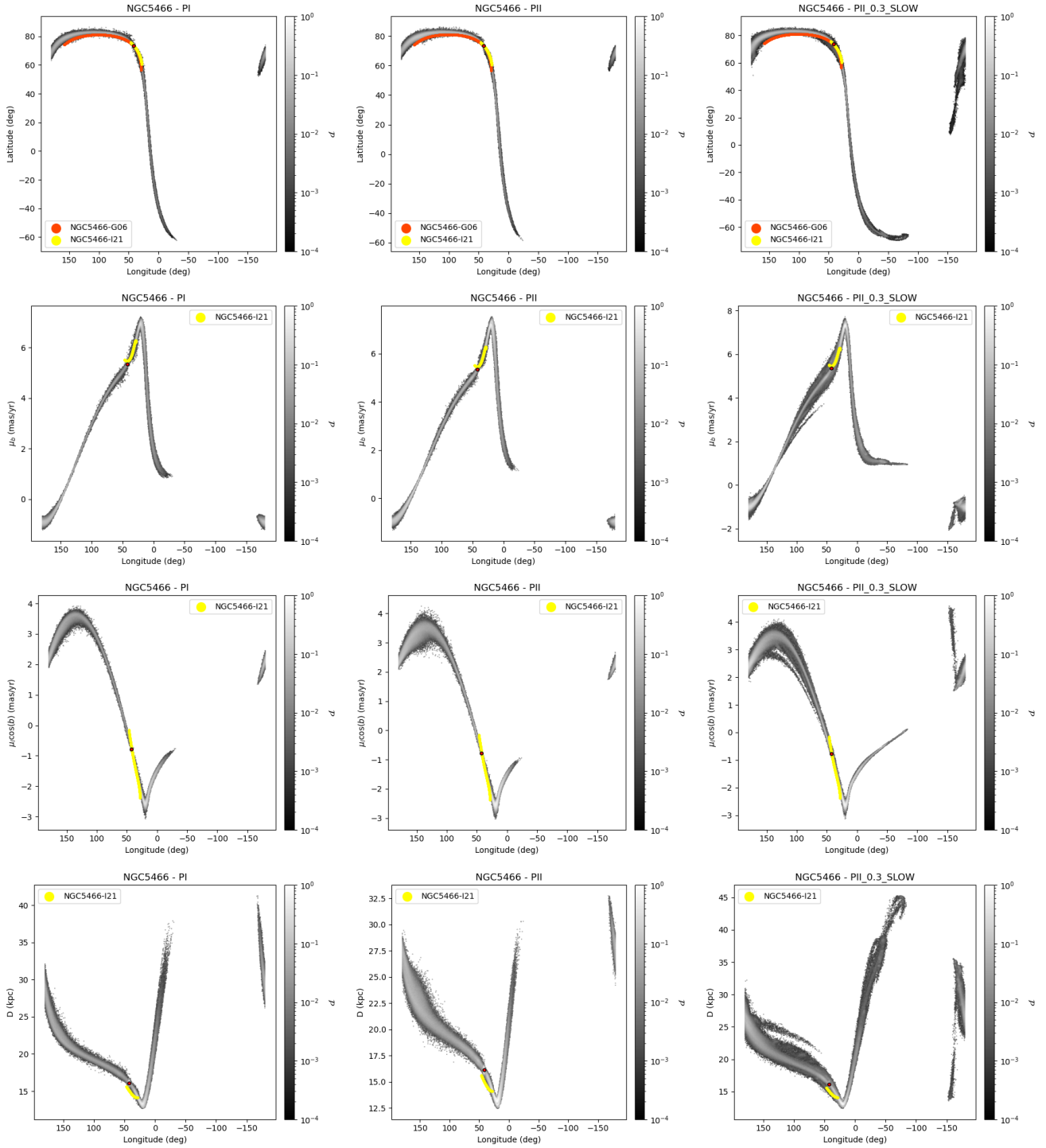


Fig. 12. Probability density maps arising from our simulations plotted against observed stellar streams as in Figs. 10 and 11, but for the case of the NGC 5466 cluster. Model predictions are compared to the tracks available in the galstreams library and those coming from the work by Grillmair & Johnson (2006, red lines) and Ibata et al. (2021, yellow lines). Note: proper motions and distances are available only for the NGC5466-I21 track. We also note that the variations in the streams, specifically the different stripes, originate from the errors considered in the simulations.

extended than that discovered so far in the observations. In particular, there is a portion of the leading tail at $0 < \ell < 42^\circ$ that has not yet been discovered, lying at distances from the Sun closer or similar to that of the known stream.

Pal 5. About 20 yr after the discovery of its tidal tails (Odenkirchen et al. 2001, 2003), Pal 5 still represents the prototype cluster surrounded by thin and extended streams of stars.

The extension, morphology, kinematics, and chemical composition of its tails have been extensively studied, both observationally and numerically (Odenkirchen et al. 2002, 2009; Rockosi et al. 2002; Dehnen et al. 2004; Koch et al. 2004; Grillmair & Dionatos 2006a; Mastrobuono-Battisti et al. 2012; Küpper et al. 2015; Kuzma et al. 2015, 2022; Fritz & Kallivayalil 2015; Ibata et al. 2016, 2017, 2021; Ishigaki et al. 2016; Thomas et al. 2016; Koch & Côté 2017; Pearson et al. 2017; Price-Whelan et al. 2019;

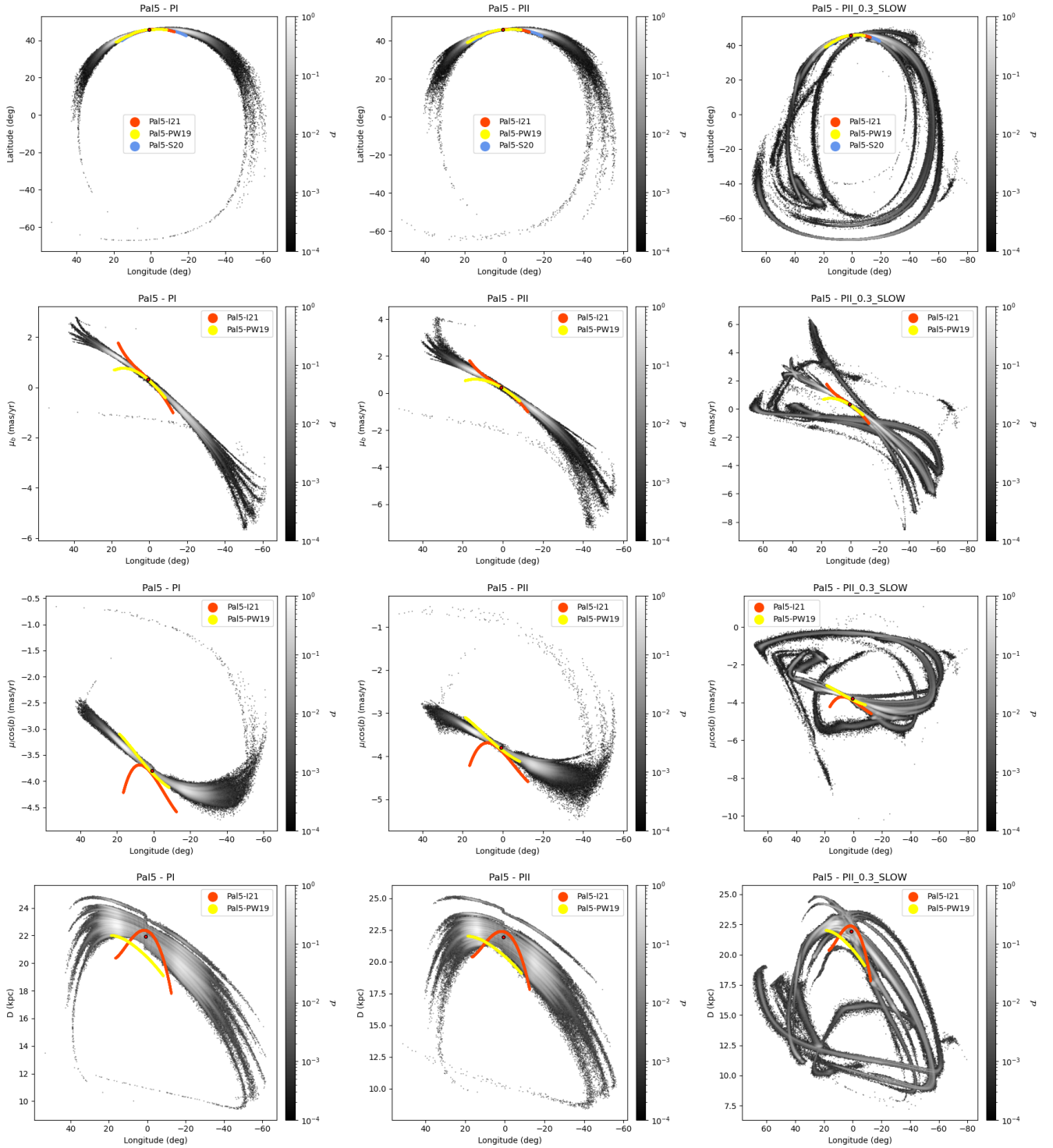


Fig. 13. Probability density maps arising from our simulations plotted against observed stellar streams as in Figs. 10–12, but for the case of the Palomar 5 cluster. Model predictions are compared to the tracks available in the galstreams library and those coming from the work by [Ibata et al. \(2021\)](#), [Price-Whelan et al. \(2019\)](#), [Starkman et al. \(2020\)](#), and [Ibata et al. \(2021\)](#). Note: proper motions and distances are not available for the Pal5-S20 track.

[Starkman et al. 2020](#); [Bonaca et al. 2020b](#); [Phillips et al. 2022](#)). In Fig. 13, we report the comparison of our model predictions to the tracks available for this cluster in galstreams and those coming from the work by [Price-Whelan et al. \(2019\)](#), [Starkman et al. \(2020\)](#), and [Ibata et al. \(2021\)](#). Projected in the (ℓ, b) plane, the observed streams are in excellent agreement with the model predictions for all the Galactic potentials adopted. Interestingly, all

potentials suggest more extended streams than those discovered so far. In the case of the barred potential, we note that the prediction of the stream position in the sky at large angular distances from the cluster center is still highly uncertain. This is due to the fact that the uncertainties are still affecting the current distance of Pal 5 to the Sun, combined with the impact of the rotating bar, which can be more or less efficient in perturbing the stream

depending on the torques experienced by the latter at pericenter; these, in turn, depend on the orbital parameters of the cluster itself. Pearson et al. (2017) already explored the effect of a rotating bar on the extension and morphology of Pal 5 tails. While we can confirm the Pearson et al. (2017) findings, namely, that both characteristics are affected by a rotating bar, we also emphasize that both the extension of the leading tail (i.e., the portion of the stream at negative longitudes) and its morphology depend on the choice of the bar pattern speed. For example, we do not find a density drop in the leading tail as reported by Pearson et al. (2017). These authors adopted a higher bar pattern speed than the one adopted in this work ($\Omega_b = 60 \text{ km s}^{-1} \text{ kpc}^{-1}$ for the example discussed in Fig. 2 of their work, right panel, while $\Omega_b = 38 \text{ km s}^{-1} \text{ kpc}^{-1}$ in our PII-0.3-SLOW model). Additionally, taking into account the uncertainties in the cluster distance, proper motions, and line-of-sight velocity is also important for obtaining robust predictions on the stream characteristics. Some of our solutions, for example, predict a very extended leading tail that is significantly more extended than those found for the axisymmetric potentials.

4. Conclusion

In this work, we have presented the first simulated catalogue of all Galactic globular clusters for which 6D phase-space information, along with masses and sizes are available. A total of 159 globular clusters has been simulated in three Milky Way-like potentials, modeling the process of tidal stripping that these clusters have experienced over the past 5 Gyr. As a result, for all clusters, we can predict the distribution of the extra-tidal material in the sky, their proper motions, distances to the Sun, and line-of-sight velocities. Errors on 6D phase-space information have been taken into account by generating 50 complementary simulations for each cluster, with a Monte-Carlo sampling of the uncertainties. This catalogue currently contains 24 327 simulations, for a total volume of about 370 Gb. It will be made publicly available⁹, with the intention to provide the community with an instrument that allows for: a more complete view of the expected distribution of globular clusters tidal structures in the sky, helping in formulating the interpretation of recent and future discoveries, supporting the search for new extra-tidal features in the data, and offering the community a repository of all these models to be compared to other theoretical and numerical predictions, which employ different Galactic potentials and/or gravity laws.

In this first paper, we have presented the distribution in the (ℓ, b) plane of all the simulated extra-tidal features. A striking result is the variety of extra-tidal shapes that globular clusters can give rise to. The canonical tidal tails of la Palomar 5 are only some of the multiple morphologies these structures can have. Ribbons, bow-ties, padlocks, and halo-shapes are also common. This variety of shapes that these stripped stars can show in the sky depends on the characteristics of the cluster orbit, on its current position in the orbit itself, and on the distance of the extra-tidal material from the Sun. Any search for the left-overs of globular clusters in the field should take into account this richness of distributions and morphologies.

These simulations have also allowed us to derive an estimate of the expected mass of stars that have escaped from the clus-

ters in the last 5 Gyr and now in the field. Although these are approximations, given the limitation of our models, our estimate of the mass lost from the Galactic globular cluster system over the last 5 Gyr is between $2-21 \times 10^6 M_\odot$, which is comparable to up to half of the total stellar mass found nowadays in the Galactic globular cluster system itself.

This work is intended to be the first of a series which investigates the properties of globular clusters streams in a variety of realistic Galactic potentials, including the perturbations induced by close dwarf satellites (Sagittarius and the Large and Small Magellanic Clouds), as well as more complex and time-varying distributions for the dark matter component.

Acknowledgements. The authors are grateful to Nicolas Leclerc for his help in the construction of the e-TidalGCs project website. The authors wish to thank H. Baumgardt and E. Vasiliev for making the globular cluster data used in this paper publicly available, as well as C. Mateu for developing the galstreams library and making it available to the community. SF and PDM would also like to thank P. Bianchini, P. Bonifacio, R. Ibata, D. Katz, N. Martin, for their interest in this work and their comments. Finally, the authors are grateful to the referee for their suggestions and remarks, which greatly improved the paper and the presentation of the results. This work has made use of the computational resources available at the Paris Observatory, as well as those obtained through the DARI grant A1020410154 (PI: P. Di Matteo), and of the Astropy, Numpy and Matplotlib libraries (Astropy Collaboration 2013, 2018; Harris et al. 2020; Hunter 2007). Salvatore Ferrone and Paola Di Matteo would like to thank the Graduate Program in Astrophysics of the Paris Sciences et Lettres University for funding this research. Alessandra Mastrobuono-Battisti acknowledges funding from the European Union's Horizon 2020 research and innovation program under the Marie Skłodowska-Curie grant agreement No 895174.

References

- Allen, C., & Santillan, A. 1991, *Rev. Mex. Astron. Astrophys.*, **22**, 255
 Amorisco, N. C., Gómez, F. A., Vegetti, S., & White, S. D. M. 2016, *MNRAS*, **463**, L17
 Astropy Collaboration (Robitaille, T. P. et al.) 2013, *A&A*, **558**, A33
 Astropy Collaboration (Price-Whelan, A. M. et al.) 2018, *AJ*, **156**, 123
 Banik, N., & Bovy, J. 2019, *MNRAS*, **484**, 2009
 Banik, N., Bovy, J., Bertone, G., Erkal, D., & de Boer, T. J. L. 2021a, *MNRAS*, **502**, 2364
 Banik, N., Bovy, J., Bertone, G., Erkal, D., & de Boer, T. J. L. 2021b, *JCAP*, **2021**, 043
 Baumgardt, H., & Hilker, M. 2018, *MNRAS*, **478**, 1520
 Baumgardt, H., & Sollima, S. 2017, *MNRAS*, **472**, 744
 Baumgardt, H., & Vasiliev, E. 2021, *MNRAS*, **505**, 5957
 Belokurov, V., Evans, N. W., Irwin, M. J., Hewett, P. C., & Wilkinson, M. I. 2006, *ApJ*, **637**, L29
 Belokurov, V., Erkal, D., Evans, N. W., Koposov, S. E., & Deason, A. J. 2018, *MNRAS*, **478**, 611
 Bianchini, P., Ibata, R., & Famaey, B. 2019, *ApJ*, **887**, L12
 Bland-Hawthorn, J., & Gerhard, O. 2016, *ARA&A*, **54**, 529
 Boldrini, P., & Vitral, E. 2021, *MNRAS*, **507**, 1814
 Bonaca, A., Hogg, D. W., Price-Whelan, A. M., & Conroy, C. 2019, *ApJ*, **880**, 38
 Bonaca, A., Conroy, C., Hogg, D. W., et al. 2020a, *ApJ*, **892**, L37
 Bonaca, A., Pearson, S., Price-Whelan, A. M., et al. 2020b, *ApJ*, **889**, 70
 Bovy, J. 2014, *ApJ*, **795**, 95
 Caldwell, N., Bonaca, A., Price-Whelan, A. M., Sesar, B., & Walker, M. G. 2020, *AJ*, **159**, 287
 Capuzzo Dolcetta, R., Di Matteo, P., & Miocchi, P. 2005, *AJ*, **129**, 1906
 Carlberg, R. G. 2018, *ApJ*, **861**, 69
 Carlberg, R. G. 2020, *ApJ*, **889**, 107
 Chemin, L., Renaud, F., & Soubiran, C. 2015, *A&A*, **578**, A14
 Chen, B., Stoughton, C., Smith, J. A., et al. 2001, *ApJ*, **553**, 184
 Combes, F., Leon, S., & Meylan, G. 1999, *A&A*, **352**, 149
 Dehnen, W., Odenkirchen, M., Grebel, E. K., & Rix, H.-W. 2004, *AJ*, **127**, 2753
 Di Matteo, P., Capuzzo Dolcetta, R., & Miocchi, P. 2005, *Celest. Mech. Dyn. Astron.*, **91**, 59
 Di Matteo, P., Gómez, A., Haywood, M., et al. 2015, *A&A*, **577**, A1
 Di Matteo, P., Haywood, M., Lehnert, M. D., et al. 2019, *A&A*, **632**, A4
 Erkal, D., Belokurov, V., Bovy, J., & Sanders, J. L. 2016, *MNRAS*, **463**, 102
 Fall, S. M., & Zhang, Q. 2001, *ApJ*, **561**, 751

⁹ All data will be available on a dedicated website (<http://etidal-project.obspm.fr/>).

- Fritz, T. K., & Kallivayalil, N. 2015, *ApJ*, **811**, 123
- Gaia Collaboration (Brown, A. G. A. et al.) 2016, *A&A*, **595**, A2
- Gaia Collaboration (Brown, A. G. A. et al.) 2018, *A&A*, **616**, A1
- Gaia Collaboration (Brown, A. G. A. et al.) 2021a, *A&A*, **649**, A1
- Gaia Collaboration (Brown, A. G. A. et al.) 2021b, *A&A*, **650**, C3
- Gallart, C., Bernard, E. J., Brook, C. B., et al. 2019, *Nat. Astron.*, **3**, 932
- Garro, E. R., Minniti, D., Gómez, M., et al. 2020, *A&A*, **642**, L19
- Garro, E. R., Minniti, D., Gómez, M., et al. 2021, *A&A*, **649**, A86
- Garro, E., Minniti, D., Alessi, B., et al. 2022a, *A&A*, **659**, A155
- Garro, E., Minniti, D., Gómez, M., et al. 2022b, *A&A*, **658**, A120
- Gnedin, O. Y., & Ostriker, J. P. 1997, *ApJ*, **474**, 223
- Gómez, A., Di Matteo, P., Schultheis, M., et al. 2018, *A&A*, **615**, A100
- Gran, F., Zoccali, M., Contreras Ramos, R., et al. 2019, *A&A*, **628**, A45
- Gran, F., Zoccali, M., Saviane, I., et al. 2022, *MNRAS*, **509**, 4962
- GRAVITY Collaboration (Abuter, R., et al.) 2018, *A&A*, **615**, L15
- Grillmair, C. J. 1998, *ASP Conf. Ser.*, **136**, 45
- Grillmair, C. J. 2022, *ApJ*, **929**, 89
- Grillmair, C. J., & Dionatos, O. 2006a, *ApJ*, **641**, L37
- Grillmair, C. J., & Dionatos, O. 2006b, *ApJ*, **643**, L17
- Grillmair, C. J., & Johnson, R. 2006, *ApJ*, **639**, L17
- Grillmair, C. J., Freeman, K. C., Irwin, M., & Quinn, P. J. 1995, *AJ*, **109**, 2553
- Hansen, T. T., Riley, A. H., Strigari, L. E., et al. 2020, *ApJ*, **901**, 23
- Harris, C. R., Millman, K. J., van der Walt, S. J., et al. 2020, *Nature*, **585**, 357
- Haywood, M., Di Matteo, P., Lehnert, M., et al. 2018, *A&A*, **618**, A78
- Heggie, D., & Hut, P. 2003, *The Gravitational Million-Body Problem: A Multidisciplinary Approach to Star Cluster Dynamics* (Cambridge University Press)
- Helmi, A., Babusiaux, C., Koppelman, H. H., et al. 2018, *Nature*, **563**, 85
- Hunter, J. D. 2007, *Comput. Sci. Eng.*, **9**, 90
- Ibata, R. A., Lewis, G. F., Irwin, M. J., & Quinn, T. 2002, *MNRAS*, **332**, 915
- Ibata, R. A., Lewis, G. F., & Martin, N. F. 2016, *ApJ*, **819**, 1
- Ibata, R. A., Lewis, G. F., Thomas, G., Martin, N. F., & Chapman, S. 2017, *ApJ*, **842**, 120
- Ibata, R. A., Malhan, K., Martin, N. F., & Starkenburg, E. 2018, *ApJ*, **865**, 85
- Ibata, R. A., Bellazzini, M., Malhan, K., Martin, N., & Bianchini, P. 2019a, *Nat. Astron.*, **3**, 667
- Ibata, R. A., Malhan, K., & Martin, N. F. 2019b, *ApJ*, **872**, 152
- Ibata, R., Thomas, G., Famaey, B., et al. 2020, *ApJ*, **891**, 161
- Ibata, R., Malhan, K., Martin, N., et al. 2021, *ApJ*, **914**, 123
- Irgang, A., Wilcox, B., Tucker, E., & Schiefelbein, L. 2013, *A&A*, **549**, A137
- Ishigaki, M. N., Hwang, N., Chiba, M., & Aoki, W. 2016, *ApJ*, **823**, 157
- Jensen, J., Thomas, G., McConnachie, A. W., et al. 2021, *MNRAS*, **507**, 1923
- Johnston, K. V., Spergel, D. N., & Haydn, C. 2002, *ApJ*, **570**, 656
- Kaderali, S., Hunt, J. A. S., Webb, J. J., Price-Jones, N., & Carlberg, R. 2019, *MNRAS*, **484**, L114
- Katz, D., Sartoretti, P., Guerrier, A., et al. 2023, *A&A*, in press, <https://doi.org/10.1051/0004-6361/202244220>
- Keenan, D. W., & Innanen, K. A. 1975, *AJ*, **80**, 290
- Koch, A., & Côté, P. 2017, *A&A*, **601**, A41
- Koch, A., Grebel, E. K., Odenkirchen, M., Martínez-Delgado, D., & Caldwell, J. A. R. 2004, *AJ*, **128**, 2274
- Kruijssen, J. M. D., Pfeffer, J. L., Chevance, M., et al. 2020, *MNRAS*, **498**, 2472
- Kunder, A., Koch, A., Rich, R. M., et al. 2012, *AJ*, **143**, 57
- Kundu, R., Minniti, D., & Singh, H. P. 2019, *MNRAS*, **483**, 1737
- Küpper, A. H. W., Kroupa, P., Baumgardt, H., & Heggie, D. C. 2010, *MNRAS*, **401**, 105
- Küpper, A. H. W., Lane, R. R., & Heggie, D. C. 2012, *MNRAS*, **420**, 2700
- Küpper, A. H. W., Balbinot, E., Bonaca, A., et al. 2015, *ApJ*, **803**, 80
- Kuzma, P. B., Da Costa, G. S., Keller, S. C., & Maunder, E. 2015, *MNRAS*, **446**, 3297
- Kuzma, P. B., Ferguson, A. M. N., Varri, A. L., et al. 2022, *MNRAS*, **512**, 315
- Lane, R. R., Kiss, L. L., Lewis, G. F., et al. 2010, *MNRAS*, **406**, 2732
- Lane, R. R., Küpper, A. H. W., & Heggie, D. C. 2012, *MNRAS*, **423**, 2845
- Leon, S., Meylan, G., & Combes, F. 2000, *A&A*, **359**, 907
- Long, K., & Murali, C. 1992, *ApJ*, **397**, 44
- Malhan, K., & Ibata, R. A. 2019, *MNRAS*, **486**, 2995
- Malhan, K., Ibata, R. A., Goldman, B., et al. 2018a, *MNRAS*, **478**, 3862
- Malhan, K., Ibata, R. A., & Martin, N. F. 2018b, *MNRAS*, **481**, 3442
- Malhan, K., Ibata, R. A., Carlberg, R. G., et al. 2019, *ApJ*, **886**, L7
- Malhan, K., Yuan, Z., Ibata, R. A., et al. 2021, *ApJ*, **920**, 51
- Mancillas, B., Duc, P.-A., Combes, F., et al. 2019, *A&A*, **632**, A122
- Massari, D., Koppelman, H. H., & Helmi, A. 2019, *A&A*, **630**, L4
- Mastrobuono-Battisti, A., Di Matteo, P., Montuori, M., & Haywood, M. 2012, *A&A*, **546**, L7
- Mateu, C. 2023, *MNRAS*, **520**, 5225
- Meylan, G., & Heggie, D. C. 1997, *A&ARv*, **8**, 1
- Minniti, D., Hempel, M., Toledo, I., et al. 2011, *A&A*, **527**, A81
- Minniti, D., Geisler, D., Alonso-García, J., et al. 2017a, *ApJ*, **849**, L24
- Minniti, D., Palma, T., Dékány, I., et al. 2017b, *ApJ*, **838**, L14
- Minniti, D., Schlafly, E. F., Palma, T., et al. 2018, *ApJ*, **866**, 12
- Minniti, D., Fernández-Trincado, J. G., Gómez, M., et al. 2021a, *A&A*, **650**, L11
- Minniti, D., Palma, T., Camargo, D., et al. 2021b, *A&A*, **652**, A129
- Mirabal, N., & Bonaca, A. 2021, *JCAP*, **2021**, 033
- Moni Bidin, C., Mauro, F., Geisler, D., et al. 2011, *A&A*, **535**, A33
- Montuori, M., Capuzzo-Dolcetta, R., Di Matteo, P., Lepinette, A., & Miocchi, P. 2007, *ApJ*, **659**, 1212
- Murali, C., & Weinberg, M. D. 1997a, *MNRAS*, **288**, 749
- Murali, C., & Weinberg, M. D. 1997b, *MNRAS*, **291**, 717
- Naik, A. P., Evans, N. W., Puchwein, E., Zhao, H., & Davis, A. C. 2020, *Phys. Rev. D*, **102**, 084066
- Navarrete, C., Belokurov, V., & Koposov, S. E. 2017, *ApJ*, **841**, L23
- Nie, J., Tian, H., Li, J., et al. 2022, *ApJ*, **930**, 23
- Odenkirchen, M., Grebel, E. K., Rockosi, C. M., et al. 2001, *ApJ*, **548**, L165
- Odenkirchen, M., Grebel, E. K., Dehnen, W., Rix, H.-W., & Cudworth, K. M. 2002, *AJ*, **124**, 1497
- Odenkirchen, M., Grebel, E. K., Dehnen, W., et al. 2003, *AJ*, **126**, 2385
- Odenkirchen, M., Grebel, E. K., Kayser, A., Rix, H.-W., & Dehnen, W. 2009, *AJ*, **137**, 3378
- Oh, K. S., & Lin, D. N. C. 1992, *ApJ*, **386**, 519
- Oh, K. S., Lin, D. N. C., & Aarseth, S. J. 1992, *ApJ*, **386**, 506
- Palau, C. G., & Miralda-Escudé, J. 2019, *MNRAS*, **488**, 1535
- Palau, C. G., & Miralda-Escudé, J. A. 2021, *MNRAS*, **504**, 2727
- Pearson, S., Price-Whelan, A. M., & Johnston, K. V. 2017, *Nat. Astron.*, **1**, 633
- Phillips, S. G., Schiavon, R. P., Mackereth, J. T., et al. 2022, *MNRAS*, **510**, 3727
- Piatti, A. E. 2017, *ApJ*, **846**, L10
- Piatti, A. E. 2018, *MNRAS*, **473**, 492
- Piatti, A. E. 2021, *MNRAS*, **505**, 3033
- Piatti, A. E. 2022, *MNRAS*, **509**, 3709
- Piatti, A. E., & Carballo-Bello, J. A. 2019, *MNRAS*, **485**, 1029
- Piatti, A. E., & Carballo-Bello, J. A. 2020, *A&A*, **637**, L2
- Piatti, A. E., & Fernández-Trincado, J. G. 2020, *A&A*, **635**, A93
- Piatti, A. E., Carballo-Bello, J. A., Mora, M. D., et al. 2020, *A&A*, **643**, A15
- Piatti, A. E., Mestre, M. F., Carballo-Bello, J. A., et al. 2021, *A&A*, **646**, A176
- Pouliasis, E., Di Matteo, P., & Haywood, M. 2017, *A&A*, **598**, A66
- Price-Whelan, A. M., Mateu, C., Iorio, G., et al. 2019, *AJ*, **158**, 223
- Reid, M. J., Menten, K. M., Brunthaler, A., et al. 2014, *ApJ*, **783**, 130
- Riley, A. H., & Strigari, L. E. 2020, *MNRAS*, **494**, 983
- Rockosi, C. M., Odenkirchen, M., Grebel, E. K., et al. 2002, *AJ*, **124**, 349
- Sanders, J. L., & Binney, J. 2013, *MNRAS*, **433**, 1813
- Sanders, J. L., Bovy, J., & Erkal, D. 2016, *MNRAS*, **457**, 3817
- Schönrich, R., Binney, J., & Dehnen, W. 2010, *MNRAS*, **403**, 1829
- Shen, J., Rich, R. M., Kormendy, J., et al. 2010, *ApJ*, **720**, L72
- Shipp, N., Drlica-Wagner, A., Balbinot, E., et al. 2018, *ApJ*, **862**, 114
- Shipp, N., Price-Whelan, A. M., Tavangar, K., Mateu, C., & Drlica-Wagner, A. 2020, *AJ*, **160**, 244
- Siegal-Gaskins, J. M., & Valluri, M. 2008, *ApJ*, **681**, 40
- Sofue, Y. 2012, *PASJ*, **64**, 75
- Sollima, A., Martínez-Delgado, D., Valls-Gabaud, D., & Peñarrubia, J. 2011, *ApJ*, **726**, 47
- Starkman, N., Bovy, J., & Webb, J. J. 2020, *MNRAS*, **493**, 4978
- Thomas, G. F., Ibata, R., Famaey, B., Martin, N. F., & Lewis, G. F. 2016, *MNRAS*, **460**, 2711
- Thomas, G. F., Famaey, B., Ibata, R., et al. 2018, *A&A*, **609**, A44
- Thomas, G. F., Jensen, J., McConnachie, A., et al. 2020, *ApJ*, **902**, 89
- Vasiliev, E., & Baumgardt, H. 2021, *MNRAS*, **505**, 5978
- Vasiliev, E., Belokurov, V., & Erkal, D. 2021, *MNRAS*, **501**, 2279
- Vesperini, E., & Heggie, D. C. 1997, *MNRAS*, **289**, 898
- Vitral, E., & Boldrini, P. 2022, *A&A*, **667**, A112
- Webb, J. J., & Bovy, J. 2019, *MNRAS*, **485**, 5929
- Wegg, C., & Gerhard, O. 2013, *MNRAS*, **435**, 1874
- Wegg, C., Gerhard, O., & Portail, M. 2015, *MNRAS*, **450**, 4050
- Yim, K.-J., & Lee, H. M. 2002, *J. Korean Astron. Soc.*, **35**, 75
- Yuan, Z., Malhan, K., Sestito, F., et al. 2022, *ApJ*, **930**, 103
- Zhang, S., Mackey, D., & Da Costa, G. S. 2022, *MNRAS*, **513**, 3136

Appendix A: Additional table
Table A.1. Current positions in the sky, proper motions, line-of-sight velocities, distances and relative uncertainties, masses, and half-mass radii for all globular clusters analyzed in this study.

Cluster	D kpc	err D kpc	α degrees	δ degrees	μ_α mas/yr	err μ_α mas/yr	μ_δ mas/yr	err μ_δ mas/yr	$v_{\ell os}$ km/s	err $v_{\ell os}$ km/s	M_{GC} M_\odot	r_h pc
2MASS-GC01	3.37	0.62	272.0909	-19.8297	-1.121	0.296	-1.881	0.235	-31.28	0.50	35100	4.70
2MASS-GC02	5.50	0.44	272.4021	-20.7789	4.000	0.900	-4.700	0.800	-237.75	10.10	15800	2.85
AM1	118.91	3.40	58.7596	-49.6153	0.291	0.107	-0.177	0.086	118.00	14.14	19200	19.86
AM4	29.01	0.94	209.0891	-27.1652	-0.291	0.445	-2.512	0.344	151.19	2.85	756	15.00
Arp2	28.73	0.34	292.1838	-30.3556	-2.331	0.031	-1.475	0.029	122.64	0.29	37000	18.45
BH140	4.81	0.25	193.4729	-67.1773	-14.848	0.024	1.224	0.024	90.30	0.35	59900	9.53
BH261	6.12	0.26	273.5275	-28.6350	3.566	0.043	-3.590	0.037	-45.00	15.00	22000	4.66
Crater	147.23	4.27	174.0687	-10.8770	-0.059	0.125	-0.116	0.116	148.10	0.65	10800	25.74
Djor1	9.88	0.65	266.8696	-33.0664	-4.693	0.046	-8.468	0.041	-359.18	1.64	79700	5.57
Djor2	8.76	0.18	270.4544	-27.8258	0.662	0.042	-2.983	0.037	-149.75	1.10	125000	5.16
E3	7.88	0.25	140.2378	-77.2819	-2.727	0.027	7.083	0.027	11.71	0.34	2890	6.14
ESO280-SC06	20.95	0.65	272.2750	-46.4233	-0.688	0.039	-2.777	0.033	93.20	0.34	7800	9.65
ESO452-SC11	7.39	0.20	249.8542	-28.3992	-1.423	0.031	-6.472	0.030	16.37	0.44	8260	3.68
Eridanus	84.68	2.89	66.1856	-21.1868	0.510	0.039	-0.301	0.041	-23.15	0.73	11600	17.91
FSR1716	7.43	0.27	242.6250	-53.7489	-4.354	0.033	-8.832	0.031	-30.70	0.98	64300	5.16
FSR1735	9.08	0.53	253.0442	-47.0581	-4.439	0.054	-1.534	0.048	-69.85	4.88	72300	2.97
FSR1758	11.09	0.74	262.8000	-39.8080	-2.881	0.026	2.519	0.025	227.31	0.59	628000	17.04
HP1	7.00	0.14	262.7717	-29.9817	2.523	0.039	-10.093	0.037	39.76	1.22	124000	3.74
IC1257	26.59	1.43	261.7854	-7.0931	-1.007	0.040	-1.492	0.032	-137.97	2.04	18100	5.54
IC1276	4.55	0.25	272.6844	-7.2076	-2.553	0.026	-4.568	0.026	155.06	0.69	73900	5.21
IC4499	18.89	0.25	225.0772	-82.2138	0.466	0.025	-0.489	0.025	38.41	0.31	155000	14.96
Laevens3	61.77	1.65	316.7267	14.9805	0.172	0.101	-0.666	0.080	-70.30	0.82	2120	9.46
Liller1	8.06	0.34	263.3523	-33.3896	-5.403	0.109	-7.431	0.077	60.36	2.44	915000	2.01
Lynga7	7.90	0.16	242.7652	-55.3178	-3.851	0.027	-7.050	0.027	17.86	0.83	79600	5.16
NGC104	4.52	0.03	6.0238	-72.0813	5.252	0.021	-2.551	0.021	-17.45	0.16	895000	6.30
NGC1261	16.40	0.19	48.0675	-55.2162	1.596	0.025	-2.064	0.025	71.34	0.21	182000	5.23
NGC1851	11.95	0.13	78.5282	-40.0466	2.145	0.024	-0.650	0.024	321.40	1.55	318000	2.90
NGC1904	13.08	0.18	81.0458	-24.5244	2.469	0.025	-1.594	0.025	205.76	0.20	139000	3.21
NGC2298	9.83	0.17	102.2475	-36.0053	3.320	0.025	-2.175	0.026	147.15	0.57	55800	3.31
NGC2419	88.47	2.40	114.5353	38.8819	0.007	0.028	-0.523	0.026	-21.10	0.31	971000	26.50
NGC2808	10.06	0.11	138.0129	-64.8635	0.994	0.024	0.273	0.024	103.57	0.27	864000	3.89
NGC288	8.99	0.09	13.1885	-26.5826	4.164	0.024	-5.705	0.024	-44.45	0.13	93400	8.37
NGC3201	4.74	0.04	154.4034	-46.4125	8.348	0.022	-1.958	0.022	493.65	0.21	160000	6.78
NGC362	8.83	0.10	15.8094	-70.8488	6.694	0.025	-2.535	0.024	223.12	0.28	284000	3.79
NGC4147	18.54	0.21	182.5263	18.5426	-1.707	0.027	-2.090	0.027	179.35	0.31	39000	4.03
NGC4372	5.71	0.21	186.4391	-72.6591	-6.409	0.024	3.297	0.024	75.59	0.30	198000	8.53
NGC4590	10.40	0.10	189.8666	-26.7441	-2.739	0.024	1.779	0.024	-93.11	0.18	122000	7.58
NGC4833	6.48	0.08	194.8913	-70.8765	-8.377	0.025	-0.963	0.025	201.99	0.40	206000	4.76
NGC5024	18.50	0.18	198.2302	18.1682	-0.133	0.024	-1.331	0.024	-63.37	0.25	455000	10.18
NGC5053	17.54	0.23	199.1129	17.7003	-0.329	0.025	-1.213	0.025	42.82	0.25	74200	17.31
NGC5139	5.43	0.05	201.6970	-47.4795	-3.250	0.022	-6.746	0.022	232.78	0.21	3640000	10.36
NGC5272	10.18	0.08	205.5484	28.3773	-0.152	0.023	-2.670	0.022	-147.20	0.27	406000	6.34
NGC5286	11.10	0.14	206.6117	-51.3742	0.198	0.025	-0.153	0.025	62.38	0.40	353000	3.79
NGC5466	16.12	0.16	211.3637	28.5344	-5.342	0.025	-0.822	0.024	106.82	0.20	59800	14.03
NGC5634	25.96	0.62	217.4053	-5.9764	-1.692	0.027	-1.478	0.026	-16.07	0.60	228000	7.39
NGC5694	34.84	0.74	219.9012	-26.5388	-0.464	0.029	-1.105	0.029	-139.55	0.49	317000	4.86
NGC5824	31.71	0.60	225.9942	-33.0681	-1.189	0.026	-2.234	0.026	-25.24	0.52	762000	6.51
NGC5897	12.55	0.24	229.3517	-21.0101	-5.422	0.025	-3.393	0.025	101.31	0.22	157000	10.99
NGC5904	7.48	0.06	229.6384	2.0810	4.086	0.023	-9.870	0.023	53.50	0.25	394000	5.68
NGC5927	8.27	0.11	232.0029	-50.6730	-5.056	0.025	-3.217	0.025	-104.09	0.28	275000	5.28
NGC5946	9.64	0.51	233.8691	-50.6597	-5.331	0.028	-1.657	0.027	137.60	0.94	93100	2.59

Table A.1. continued.

Cluster	D kpc	err D kpc	α degrees	δ degrees	μ_α mas/yr	err μ_α mas/yr	μ_δ mas/yr	err μ_δ mas/yr	v_{los} km/s	err v_{los} km/s	M_{GC} M_\odot	r_h pc
NGC5986	10.54	0.13	236.5125	-37.7864	-4.192	0.026	-4.568	0.026	101.18	0.43	334000	4.25
NGC6093	10.34	0.12	244.2600	-22.9761	-2.934	0.027	-5.578	0.026	10.93	0.39	338000	2.62
NGC6101	14.45	0.19	246.4505	-72.2022	1.756	0.024	-0.258	0.025	366.33	0.32	178000	14.06
NGC6121	1.85	0.02	245.8967	-26.5257	-12.514	0.023	-19.022	0.023	71.21	0.15	87100	3.69
NGC6139	10.04	0.45	246.9185	-38.8488	-6.081	0.027	-2.711	0.026	24.41	0.95	323000	2.47
NGC6144	8.15	0.13	246.8078	-26.0235	-1.744	0.026	-2.607	0.026	194.79	0.58	79200	4.91
NGC6171	5.63	0.08	248.1328	-13.0538	-1.939	0.025	-5.979	0.025	-34.71	0.18	74900	3.94
NGC6205	7.42	0.08	250.4218	36.4599	-3.149	0.023	-2.574	0.023	-244.90	0.30	545000	5.26
NGC6218	5.11	0.05	251.8091	-1.9485	-0.191	0.024	-6.802	0.024	-41.67	0.14	107000	4.05
NGC6229	30.11	0.47	251.7452	47.5278	-1.171	0.026	-0.467	0.027	-137.89	0.71	286000	4.41
NGC6235	11.94	0.38	253.3557	-22.1774	-3.931	0.027	-7.587	0.027	126.68	0.33	107000	4.78
NGC6254	5.07	0.06	254.2877	-4.1003	-4.758	0.024	-6.597	0.024	74.21	0.23	205000	4.81
NGC6256	7.24	0.29	254.8861	-37.1210	-3.715	0.031	-1.637	0.030	-99.75	0.66	125000	4.82
NGC6266	6.41	0.10	255.3042	-30.1134	-4.978	0.026	-2.947	0.026	-73.98	0.67	610000	2.43
NGC6273	8.34	0.16	255.6575	-26.2680	-3.249	0.026	1.660	0.025	145.54	0.59	697000	4.21
NGC6284	14.21	0.42	256.1201	-24.7648	-3.200	0.029	-2.002	0.028	28.62	0.73	129000	3.78
NGC6287	7.93	0.37	256.2889	-22.7080	-5.010	0.029	-1.883	0.028	-294.74	1.65	145000	3.65
NGC6293	9.19	0.28	257.5425	-26.5821	0.870	0.028	-4.326	0.028	-143.66	0.39	205000	4.05
NGC6304	6.15	0.15	258.6344	-29.4620	-4.070	0.029	-1.088	0.028	-108.62	0.39	126000	4.26
NGC6316	11.15	0.39	259.1554	-28.1401	-4.969	0.031	-4.592	0.030	99.65	0.84	318000	4.77
NGC6325	7.53	0.32	259.4963	-23.7677	-8.289	0.030	-9.000	0.029	29.54	0.58	58900	2.05
NGC6333	8.30	0.14	259.7991	-18.5163	-2.180	0.026	-3.222	0.026	310.75	2.12	323000	4.17
NGC6341	8.50	0.07	259.2808	43.1359	-4.935	0.024	-0.625	0.024	-120.55	0.27	352000	4.49
NGC6342	8.01	0.23	260.2916	-19.5877	-2.903	0.027	-7.116	0.026	115.75	0.90	42200	2.06
NGC6352	5.54	0.07	261.3713	-48.4222	-2.158	0.025	-4.447	0.025	-125.63	1.01	64700	4.56
NGC6355	8.65	0.22	260.9935	-26.3528	-4.738	0.031	-0.572	0.030	-195.85	0.55	101000	3.55
NGC6356	15.66	0.92	260.8958	-17.8130	-3.750	0.026	-3.392	0.026	48.18	1.82	600000	6.86
NGC6362	7.65	0.07	262.9791	-67.0483	-5.506	0.024	-4.763	0.024	-14.58	0.18	127000	7.23
NGC6366	3.44	0.05	261.9344	-5.0799	-0.332	0.025	-5.160	0.024	-120.65	0.19	37600	5.56
NGC6380	9.61	0.30	263.6186	-39.0695	-2.183	0.031	-3.233	0.030	-1.48	0.73	334000	4.40
NGC6388	11.17	0.16	264.0718	-44.7355	-1.316	0.026	-2.709	0.026	83.11	0.45	1250000	4.34
NGC6397	2.48	0.02	265.1754	-53.6743	3.260	0.023	-17.664	0.022	18.51	0.08	96600	3.90
NGC6401	8.06	0.24	264.6522	-23.9096	-2.748	0.035	1.444	0.034	-105.44	2.50	145000	3.28
NGC6402	9.14	0.25	264.4007	-3.2459	-3.590	0.025	-5.059	0.025	-60.71	0.45	592000	5.14
NGC6426	20.71	0.35	266.2280	3.1701	-1.828	0.026	-2.999	0.026	-210.51	0.51	71700	8.00
NGC6440	8.25	0.24	267.2202	-20.3604	-1.187	0.036	-4.020	0.035	-69.39	0.93	489000	2.14
NGC6441	12.73	0.16	267.5544	-37.0514	-2.551	0.028	-5.348	0.028	18.47	0.56	1320000	3.47
NGC6453	10.07	0.22	267.7155	-34.5985	0.203	0.036	-5.934	0.037	-99.23	1.24	165000	3.85
NGC6496	9.64	0.15	269.7654	-44.2659	-3.060	0.027	-9.271	0.026	-134.72	0.26	68900	6.42
NGC6517	9.23	0.56	270.4608	-8.9588	-1.551	0.029	-4.470	0.028	-35.06	1.65	195000	2.29
NGC6522	7.29	0.21	270.8920	-30.0340	2.566	0.039	-6.438	0.036	-15.23	0.49	211000	3.08
NGC6528	7.83	0.24	271.2067	-30.0558	-2.157	0.043	-5.649	0.039	211.86	0.43	56700	2.73
NGC6535	6.36	0.12	270.9604	-0.2976	-4.214	0.027	-2.939	0.026	-214.85	0.46	21900	3.65
NGC6539	8.16	0.39	271.2073	-7.5859	-6.896	0.026	-3.537	0.026	35.19	0.50	209000	5.18
NGC6540	5.91	0.27	271.5357	-27.7653	-3.702	0.032	-2.791	0.032	-16.50	0.78	34500	5.32
NGC6541	7.61	0.10	272.0098	-43.7149	0.287	0.025	-8.847	0.025	-163.97	0.46	293000	4.34
NGC6544	2.58	0.06	271.8338	-24.9982	-2.304	0.031	-18.604	0.030	-38.46	0.67	91400	2.07
NGC6553	5.33	0.13	272.3153	-25.9078	0.344	0.030	-0.454	0.029	-0.27	0.34	285000	4.56
NGC6558	7.47	0.29	272.5740	-31.7645	-1.720	0.036	-4.144	0.034	-195.12	0.73	26500	1.70
NGC6569	10.53	0.26	273.4117	-31.8269	-4.125	0.028	-7.354	0.028	-49.83	0.50	236000	3.85
NGC6584	13.61	0.17	274.6566	-52.2158	-0.090	0.026	-7.202	0.025	260.64	1.58	102000	5.37
NGC6624	8.02	0.11	275.9188	-30.3610	0.124	0.029	-6.936	0.029	54.79	0.40	156000	3.69
NGC6626	5.37	0.10	276.1370	-24.8698	-0.278	0.028	-8.922	0.028	11.11	0.60	299000	2.26

Table A.1. continued.

Cluster	D kpc	err D kpc	α degrees	δ degrees	μ_α mas/yr	err μ_α mas/yr	μ_δ mas/yr	err μ_δ mas/yr	$v_{\ell os}$ km/s	err $v_{\ell os}$ km/s	M_{GC} M_\odot	r_h pc
NGC6637	8.90	0.10	277.8463	-32.3481	-5.034	0.028	-5.832	0.028	47.48	1.00	155000	3.69
NGC6638	9.78	0.34	277.7337	-25.4975	-2.518	0.029	-4.076	0.029	8.63	2.00	118000	2.20
NGC6642	8.05	0.20	277.9760	-23.4756	-0.173	0.030	-3.892	0.030	-60.61	1.35	34400	1.51
NGC6652	9.46	0.14	278.9401	-32.9907	-5.484	0.027	-4.274	0.027	-95.37	0.86	48100	1.96
NGC6656	3.30	0.04	279.0998	-23.9047	9.851	0.023	-5.617	0.023	-148.72	0.78	476000	5.29
NGC6681	9.36	0.11	280.8032	-32.2921	1.431	0.027	-4.744	0.026	216.62	0.84	116000	2.89
NGC6712	7.38	0.24	283.2680	-8.7060	3.363	0.027	-4.436	0.027	-107.45	0.29	96300	3.21
NGC6715	26.28	0.33	283.7639	-30.4799	-2.679	0.025	-1.387	0.025	143.13	0.43	1780000	5.20
NGC6717	7.52	0.13	283.7752	-22.7015	-3.125	0.027	-5.008	0.027	30.25	0.90	35800	4.23
NGC6723	8.27	0.10	284.8881	-36.6322	1.028	0.025	-2.418	0.025	-94.39	0.26	177000	5.06
NGC6749	7.59	0.21	286.3141	1.8998	-2.829	0.028	-6.006	0.027	-58.44	0.96	211000	7.09
NGC6752	4.12	0.04	287.7171	-59.9846	-3.161	0.022	-4.027	0.022	-26.01	0.12	276000	5.27
NGC6760	8.41	0.43	287.8003	1.0305	-1.107	0.026	-3.615	0.026	-2.37	1.27	269000	5.22
NGC6779	10.43	0.14	289.1482	30.1835	-2.018	0.025	1.618	0.025	-136.97	0.45	186000	4.51
NGC6809	5.35	0.05	294.9988	-30.9647	-3.432	0.024	-9.311	0.024	174.70	0.17	193000	6.95
NGC6838	4.00	0.05	298.4437	18.7792	-3.416	0.025	-2.656	0.024	-22.72	0.20	65600	6.57
NGC6864	20.52	0.45	301.5198	-21.9212	-0.598	0.026	-2.810	0.026	-189.08	1.12	370000	2.96
NGC6934	15.72	0.17	308.5474	7.4045	-2.655	0.026	-4.689	0.026	-406.22	0.73	136000	5.16
NGC6981	16.66	0.18	313.3654	-12.5373	-1.274	0.026	-3.361	0.026	-331.39	1.47	68900	5.96
NGC7006	39.32	0.56	315.3726	16.1873	-0.128	0.027	-0.633	0.027	-383.47	0.73	136000	6.99
NGC7078	10.71	0.10	322.4930	12.1670	-0.659	0.024	-3.803	0.024	-106.84	0.30	633000	4.30
NGC7089	11.69	0.11	323.3626	-0.8233	3.435	0.025	-2.159	0.024	-3.78	0.30	620000	4.77
NGC7099	8.46	0.09	325.0921	-23.1799	-0.737	0.025	-7.299	0.024	-185.19	0.17	143000	4.99
NGC7492	24.39	0.57	347.1112	-15.6115	0.756	0.028	-2.320	0.028	-176.70	0.27	26600	9.89
Pal1	11.18	0.32	53.3335	79.5811	-0.252	0.034	0.007	0.037	-75.72	0.29	1030	3.56
Pal10	8.94	1.18	289.5069	18.5790	-4.322	0.029	-7.173	0.029	-31.70	0.23	162000	6.33
Pal11	14.02	0.51	296.3100	-8.0072	-1.766	0.030	-4.971	0.028	-67.64	0.76	11900	7.72
Pal12	18.49	0.30	326.6618	-21.2526	-3.220	0.029	-3.333	0.028	27.91	0.28	6270	10.52
Pal13	23.48	0.40	346.6852	12.7715	1.748	0.049	0.104	0.047	25.30	0.22	3020	16.95
Pal14	73.58	1.63	242.7525	14.9578	-0.463	0.038	-0.413	0.038	72.30	0.14	18900	36.70
Pal15	44.10	1.14	254.9626	-0.5390	-0.592	0.037	-0.901	0.034	72.27	1.74	50900	26.86
Pal2	26.17	1.28	71.5246	31.3815	1.045	0.034	-1.522	0.031	-135.97	1.55	231000	8.06
Pal3	94.84	3.23	151.3816	0.0717	0.086	0.060	-0.148	0.071	94.04	0.80	18900	27.44
Pal4	101.39	2.57	172.3183	28.9734	-0.188	0.042	-0.476	0.041	72.40	0.24	12900	21.30
Pal5	21.94	0.51	229.0192	-0.1210	-2.730	0.028	-2.654	0.027	-58.61	0.15	9980	27.64
Pal6	7.05	0.45	265.9258	-26.2250	-9.222	0.038	-5.347	0.036	177.00	1.35	94500	2.89
Pal8	11.32	0.63	280.3773	-19.8289	-1.987	0.027	-5.694	0.027	-31.54	0.21	67400	5.86
Pyxis	36.53	0.66	136.9869	-37.2266	1.030	0.032	0.138	0.035	40.46	0.21	24600	22.83
Rup106	20.71	0.36	189.6675	-51.1503	-1.254	0.026	0.401	0.026	-38.36	0.26	34200	11.57
SagittariusII	66.53	1.56	298.1647	-22.0653	-0.804	0.044	-0.882	0.028	-175.73	0.37	18500	39.31
Ter1	5.67	0.17	263.9467	-30.4818	-2.806	0.055	-4.861	0.055	56.75	1.61	150000	2.15
Ter10	10.21	0.40	270.7408	-26.0669	-6.827	0.059	-2.588	0.050	211.37	2.27	302000	4.60
Ter12	5.17	0.38	273.0658	-22.7419	-6.222	0.037	-3.052	0.034	95.61	1.21	87200	3.28
Ter2	7.75	0.33	261.8879	-30.8023	-2.170	0.041	-6.263	0.038	134.56	0.96	136000	4.16
Ter3	7.64	0.31	247.1625	-35.3398	-5.577	0.027	-1.760	0.026	-135.76	0.57	40400	7.19
Ter4	7.59	0.31	262.6625	-31.5955	-5.462	0.060	-3.711	0.048	-48.96	1.57	200000	6.06
Ter5	6.62	0.15	267.0202	-24.7791	-1.989	0.068	-5.243	0.066	-82.57	0.73	935000	3.77
Ter6	7.27	0.35	267.6932	-31.2754	-4.979	0.048	-7.431	0.039	136.45	1.50	104000	1.33
Ter7	24.28	0.49	289.4330	-34.6577	-3.002	0.029	-1.651	0.029	159.85	0.14	24000	13.21
Ter8	27.54	0.42	295.4350	-33.9995	-2.496	0.027	-1.581	0.026	148.43	0.17	62100	21.53
Ter9	5.77	0.34	270.4117	-26.8397	-2.121	0.052	-7.763	0.049	68.49	0.56	120000	1.90
Ton2	6.99	0.34	264.0393	-38.5409	-5.904	0.031	-0.755	0.029	-184.72	1.12	69100	4.60
UKS1	15.58	0.56	268.6133	-24.1453	-2.040	0.095	-2.754	0.063	59.38	2.63	77000	3.84
VVV-CL001	8.08	1.48	268.6771	-24.0147	-3.487	0.144	-1.652	0.107	-327.28	0.90	135000	2.94
WhitingI	30.59	1.17	30.7375	-3.2528	-0.228	0.065	-2.046	0.056	-130.41	1.79	1970	15.49

Appendix B: Choice of the time-step for orbit integration

To choose the optimal time-step Δt for the simulations, we quantified the energy conservation of the orbit integration, in the case where the 159 clusters evolve in isolation, that is, the case where each test-particle in a cluster feels the gravitational attraction of the cluster itself – but not that of the Galaxy. Since in the case of an isolated cluster, the gravitational potential is time-independent, the total energy, E_i , of each particle in the system (sum of the particle kinetic and potential energy) must be conserved. Any departure from energy conservation is thus a check of the quality of the integration and in particular of the choice of the adopted time-step.

For the isolated simulations, we thus proceeded as follows. We modeled each cluster as a set of $N=100\,000$ test-particles, subject to the cluster potential, only. To model this latter, for each cluster we adopted the same Plummer sphere distribution, with same characteristic radius r_c and total masse M_{GC} , as those adopted for the simulations described in Sect. 2 (see in particular Sect. 2.2). A first set of 159 isolated simulations was run adopting a $\Delta t = 10^5$ yr and a total number of steps $N_{steps} = 50000$ for all clusters, for a total simulated time interval of 5 Gyr. We then

quantified the energy conservation by calculating the median error per time-step, m_{err} , of $(\Delta E/E)_i = |(E_{fin,i} - E_{ini,i})/E_{ini,i}|$, where $E_{ini,i}$ and $E_{fin,i}$ are, respectively, the initial (time $t = 0$) and final (time $t=5$ Gyr) energy of each particle in the system. While for most of the simulated clusters (109 over 159), this choice of the time-step was sufficient to guarantee an excellent energy conservation (with m_{err} typically of the order of $10^{-11} - 10^{-12}$) for 50 clusters the corresponding m_{err} values were found to be above 10^{-10} . This was the case for all clusters with crossing times $t_{cross} = \sqrt{r_c^3/GM_{GC}}$ lower than 2×10^5 yr, that is about twice the time-step. For these clusters, we hence reduced the Δt of a factor 10, rerunning the simulations with $\Delta t = 10^4$ yr and $N_{steps} = 500000$. With such a choice, the corresponding energy conservation turned out to be excellent (below 10^{-10} per step). In Table B.1, we summarize the result of this study, reporting the cluster name, crossing time, and median error, m_{err} , in energy conservation obtained for all isolated cluster simulations. Clusters for which a $\Delta t = 10^4$ yr, and a corresponding number N_{steps} have been used, are indicated in the Table with an asterisk. The values of Δt adopted for the isolated simulations, and the associated number of time steps, N_{steps} , are also those used to run the simulations of the same clusters orbiting in the gravitational field of the Milky Way.

Table B.1. Crossing time, t_{cross} , and median error in energy conservation, m_{err} , for all 159 clusters evolved in isolation. All “isolated” simulations have been run with a $\Delta t = 10^5$ yr, and for a total of $N_{steps} = 50000$ steps, except for clusters marked with (*), for which a $\Delta t = 10^4$ yr and a total of $N_{steps} = 500000$ steps have been used.

Cluster	t_{cross}	m_{err}	Cluster	t_{cross}	m_{err}	Cluster	t_{cross}	m_{err}
2MASS-GC01	5.6×10^5	2.1×10^{-12}	2MASS-GC02	3.9×10^5	4.4×10^{-12}	AM1	6.5×10^6	5.4×10^{-13}
AM4	2.2×10^7	8.6×10^{-13}	Arp2	4.2×10^6	6.1×10^{-13}	BH140	1.2×10^6	5.3×10^{-13}
BH261	6.9×10^5	1.7×10^{-12}	Crater	1.3×10^7	4.4×10^{-13}	Djor1	4.8×10^5	1.0×10^{-12}
Djor2	3.4×10^5	3.9×10^{-12}	E3	2.9×10^6	3.3×10^{-14}	ESO280-SC06	3.5×10^6	1.1×10^{-13}
ESO452-SC11	7.9×10^5	7.9×10^{-13}	Eridanus	7.2×10^6	1.3×10^{-12}	FSR1716	4.7×10^5	3.4×10^{-13}
FSR1735	1.9×10^5	4.9×10^{-11}	FSR1758	9.1×10^5	7.4×10^{-13}	HP1	2.1×10^5	4.0×10^{-11}
IC1257	9.9×10^5	1.5×10^{-14}	IC1276	4.5×10^5	3.4×10^{-12}	IC4499	1.5×10^6	9.0×10^{-13}
Laevens3	6.5×10^6	4.7×10^{-13}	Liller1 (*)	3.0×10^4	6.0×10^{-13}	Lynga7	4.2×10^5	2.3×10^{-13}
NGC104 (*)	1.7×10^5	2.4×10^{-13}	NGC1261	2.96×10^5	1.4×10^{-11}	NGC1851 (*)	9.0×10^4	3.8×10^{-13}
NGC1904 (*)	1.6×10^5	6.8×10^{-10}	NGC2298	2.6×10^5	1.2×10^{-11}	NGC2419	1.4×10^6	1.2×10^{-12}
NGC2808 (*)	8.4×10^4	1.6×10^{-12}	NGC288	8.1×10^5	6.5×10^{-13}	NGC3201	4.5×10^5	1.6×10^{-12}
NGC362 (*)	1.4×10^5	1.9×10^{-13}	NGC4147	4.2×10^5	5.2×10^{-14}	NGC4372	5.7×10^5	4.8×10^{-13}
NGC4590	6.1×10^5	4.3×10^{-13}	NGC4833	2.3×10^5	1.8×10^{-12}	NGC5024	4.9×10^5	3.0×10^{-12}
NGC5053	2.7×10^6	4.4×10^{-13}	NGC5139 (*)	1.8×10^5	1.1×10^{-12}	NGC5272	2.6×10^5	2.0×10^{-12}
NGC5286 (*)	1.3×10^5	1.5×10^{-13}	NGC5466	2.2×10^6	1.0×10^{-12}	NGC5634	4.3×10^5	4.6×10^{-12}
NGC5694	1.9×10^5	6.9×10^{-11}	NGC5824	1.9×10^5	5.2×10^{-11}	NGC5897	9.4×10^5	2.5×10^{-13}
NGC5904	2.2×10^5	8.3×10^{-12}	NGC5927	2.4×10^5	1.9×10^{-11}	NGC5946 (*)	1.4×10^5	1.1×10^{-12}
NGC5986 (*)	1.5×10^5	7.7×10^{-13}	NGC6093 (*)	7.5×10^4	7.9×10^{-13}	NGC6101	1.3×10^6	3.5×10^{-13}
NGC6121	2.5×10^5	9.1×10^{-12}	NGC6139 (*)	7.0×10^4	3.9×10^{-13}	NGC6144	4.0×10^5	3.9×10^{-12}
NGC6171	2.9×10^5	1.7×10^{-13}	NGC6205 (*)	1.7×10^5	1.7×10^{-13}	NGC6218	2.5×10^5	3.0×10^{-12}
NGC6229 (*)	1.8×10^5	2.5×10^{-14}	NGC6235	3.3×10^5	3.1×10^{-12}	NGC6254	2.4×10^5	9.0×10^{-12}
NGC6256	3.1×10^5	7.1×10^{-12}	NGC6266 (*)	5.0×10^4	1.1×10^{-13}	NGC6273 (*)	1.1×10^5	8.0×10^{-13}
NGC6284	2.1×10^5	1.3×10^{-11}	NGC6287	1.9×10^5	3.1×10^{-11}	NGC6293	1.8×10^5	9.9×10^{-11}
NGC6304	2.5×10^5	5.9×10^{-12}	NGC6316 (*)	1.9×10^5	1.3×10^{-13}	NGC6325 (*)	1.2×10^5	4.4×10^{-13}
NGC6333 (*)	1.5×10^5	2.2×10^{-13}	NGC6341 (*)	1.6×10^5	5.6×10^{-13}	NGC6342 (*)	1.5×10^5	3.4×10^{-13}

Table B.1. continued.

Cluster	t_{cross}	m_{err}	Cluster	t_{cross}	m_{err}	Cluster	t_{cross}	m_{err}
NGC6352	3.9×10^5	2.2×10^{-12}	NGC6355	2.2×10^5	4.8×10^{-11}	NGC6356	2.4×10^5	3.0×10^{-11}
NGC6362	5.6×10^5	8.1×10^{-13}	NGC6366	6.9×10^5	4.0×10^{-13}	NGC6380 (*)	1.6×10^5	2.1×10^{-13}
NGC6388 (*)	8.3×10^4	6.0×10^{-13}	NGC6397	2.5×10^5	4.1×10^{-12}	NGC6401 (*)	1.6×10^5	6.5×10^{-13}
NGC6402 (*)	1.5×10^5	9.7×10^{-13}	NGC6426	8.6×10^5	8.6×10^{-13}	NGC6440 (*)	4.6×10^4	1.1×10^{-13}
NGC6441 (*)	5.7×10^4	2.6×10^{-14}	NGC6453	1.9×10^5	5.2×10^{-11}	NGC6496	6.3×10^5	2.7×10^{-13}
NGC6517 (*)	8.0×10^4	3.8×10^{-13}	NGC6522 (*)	1.2×10^5	5.9×10^{-13}	NGC6528	1.9×10^5	5.7×10^{-11}
NGC6535	4.8×10^5	2.9×10^{-12}	NGC6539	2.6×10^5	2.5×10^{-12}	NGC6540	6.8×10^5	2.0×10^{-13}
NGC6541 (*)	1.7×10^5	6.1×10^{-13}	NGC6544 (*)	1.0×10^5	6.4×10^{-13}	NGC6553	1.9×10^5	7.8×10^{-11}
NGC6558 (*)	1.4×10^5	7.0×10^{-13}	NGC6569 (*)	1.6×10^5	1.5×10^{-13}	NGC6584	4.0×10^5	4.7×10^{-13}
NGC6624 (*)	1.8×10^5	4.3×10^{-13}	NGC6626 (*)	6.4×10^4	2.5×10^{-12}	NGC6637	1.8×10^5	5.4×10^{-11}
NGC6638 (*)	9.7×10^4	7.8×10^{-13}	NGC6642 (*)	1.0×10^5	1.3×10^{-12}	NGC6652 (*)	1.3×10^5	3.3×10^{-13}
NGC6656 (*)	1.8×10^5	1.5×10^{-13}	NGC6681 (*)	1.5×10^5	4.3×10^{-13}	NGC6712	1.9×10^5	4.5×10^{-11}
NGC6715 (*)	9.1×10^4	1.4×10^{-12}	NGC6717	4.7×10^5	7.4×10^{-13}	NGC6723	2.8×10^5	2.1×10^{-11}
NGC6749	4.2×10^5	7.0×10^{-13}	NGC6752	2.4×10^5	2.9×10^{-11}	NGC6760	2.4×10^5	6.7×10^{-12}
NGC6779	2.3×10^5	1.3×10^{-11}	NGC6809	4.3×10^5	1.7×10^{-12}	NGC6838	6.7×10^5	7.0×10^{-14}
NGC6864 (*)	8.6×10^4	9.1×10^{-13}	NGC6934	3.2×10^5	6.4×10^{-12}	NGC6981	5.7×10^5	7.0×10^{-13}
NGC7006	5.1×10^5	9.1×10^{-13}	NGC7078 (*)	1.1×10^5	4.1×10^{-13}	NGC7089 (*)	1.4×10^5	1.3×10^{-13}
NGC7099	3.0×10^5	5.2×10^{-14}	NGC7492	1.9×10^6	6.0×10^{-13}	Pal1	2.1×10^6	3.0×10^{-13}
Pal10	4.0×10^5	4.6×10^{-13}	Pal11	2.0×10^6	3.5×10^{-13}	Pal12	4.4×10^6	1.1×10^{-12}
Pal13	1.3×10^7	3.0×10^{-13}	Pal14	1.7×10^7	7.4×10^{-13}	Pal15	6.3×10^6	9.2×10^{-14}
Pal2	4.9×10^5	4.1×10^{-13}	Pal3	1.1×10^7	8.1×10^{-13}	Pal4	8.8×10^6	6.6×10^{-13}
Pal5	1.5×10^7	6.2×10^{-13}	Pal6 (*)	1.6×10^5	1.0×10^{-12}	Pal8	5.6×10^5	1.1×10^{-12}
Pyxis	7.2×10^6	6.0×10^{-13}	Rup106	2.2×10^6	9.4×10^{-13}	SagittariusII	1.9×10^7	7.3×10^{-13}
Ter1 (*)	8.3×10^4	7.1×10^{-13}	Ter10	1.8×10^5	7.3×10^{-11}	Ter12	2.1×10^5	3.1×10^{-11}
Ter2	2.4×10^5	1.2×10^{-11}	Ter3	9.8×10^5	1.2×10^{-12}	Ter4	3.4×10^5	5.9×10^{-12}
Ter5 (*)	7.7×10^4	3.5×10^{-13}	Ter6 (*)	4.9×10^4	1.5×10^{-12}	Ter7	3.2×10^6	7.4×10^{-13}
Ter8	4.1×10^6	9.4×10^{-13}	Ter9 (*)	7.7×10^4	4.7×10^{-13}	Ton2	3.8×10^5	1.1×10^{-13}
UKS1	2.8×10^5	2.0×10^{-12}	VVV-CL001 (*)	1.4×10^5	1.1×10^{-12}	Whiting1	1.4×10^7	1.6×10^{-13}

Appendix C: Extra-tidal features generated by all the simulated clusters

In this section, we report all the extra-tidal features as predicted by our models. For each cluster, we show (from Figs. C.1 to C.20) the probability density of finding associated extra-tidal features in the sky, by calculating the 2D histogram of the

escaped particles. Each particle per cluster is present, meaning that all 100,000 particles originating each of the 50 Monte-Carlo realizations are included, plus the case with the best values (see Sect. 2.1). Thus, each map is a 500x500 histogram that bins 5.1×10^6 particles. The retrieved cumulative 2D histogram is then normalized to its maximum value and plotted in the following figures in logarithmic scale.

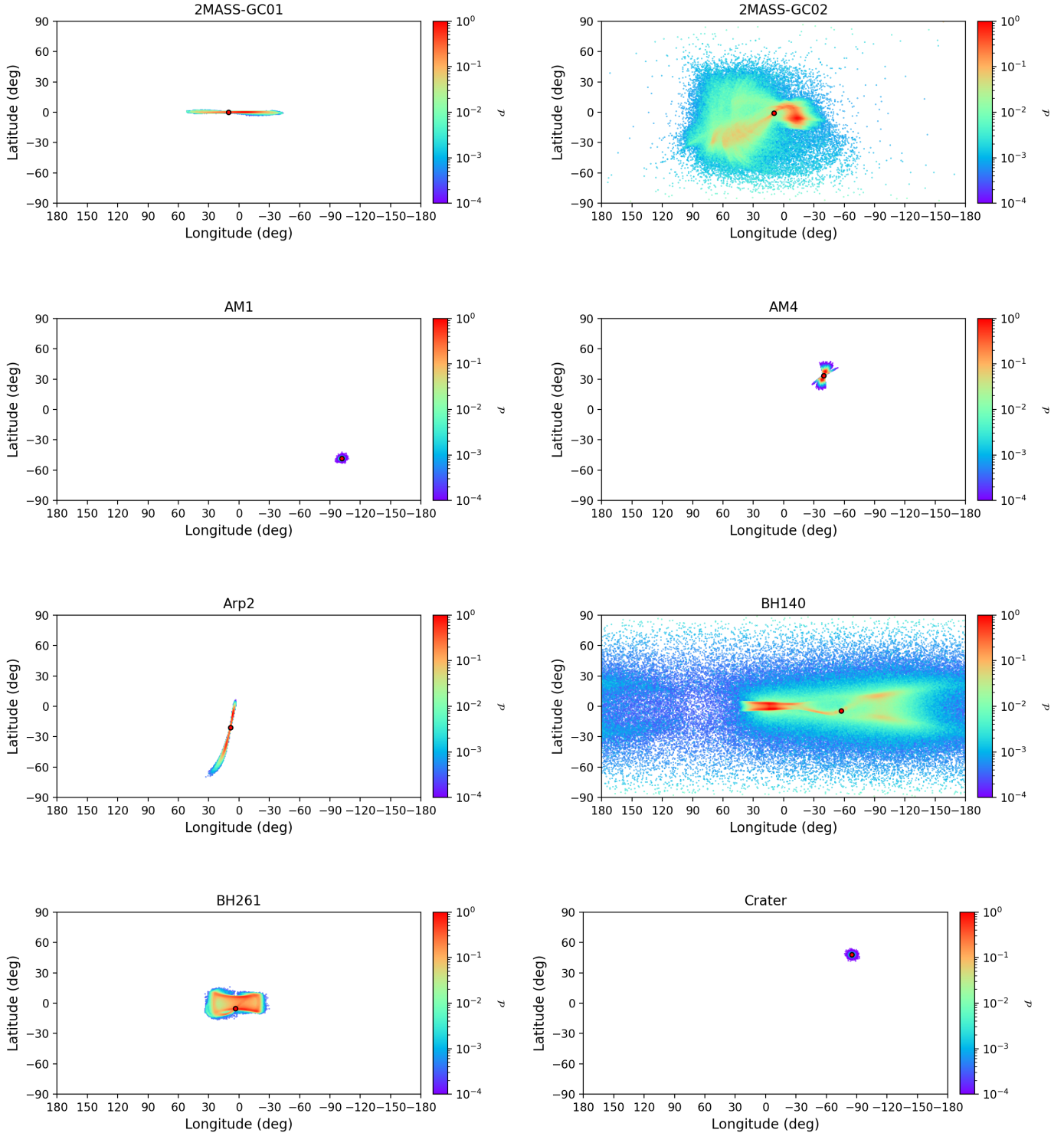


Fig. C.1. Projected density distribution in the (ℓ, b) plane of a subset of simulated globular clusters, as indicated at the top of each panel. In each panel, the red circle indicates the current position of the cluster. The densities have been normalized to their maximum value.

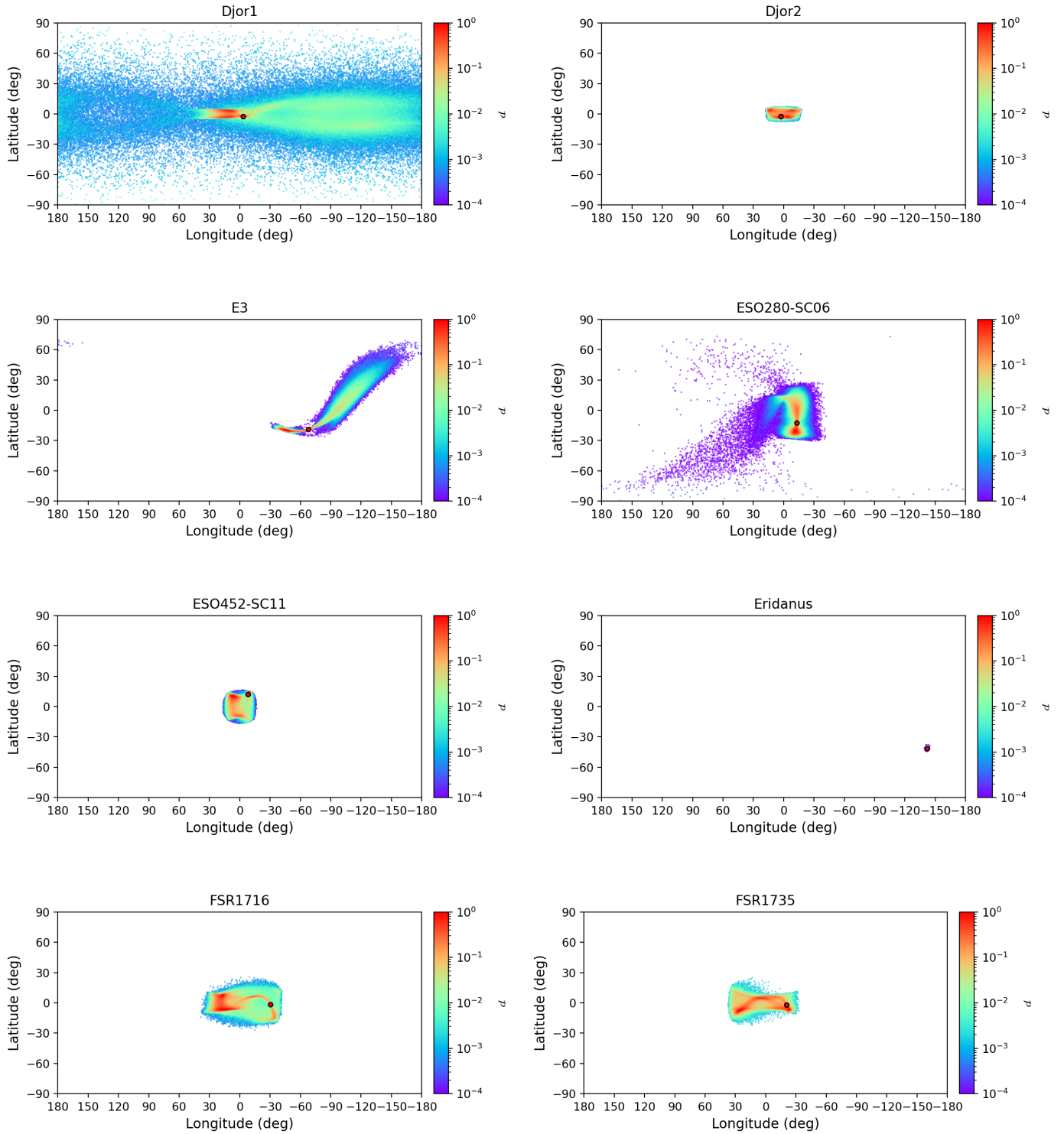


Fig. C.2. Projected density distribution in the (ℓ, b) plane of a subset of simulated globular clusters, as indicated at the top of each panel. In each panel, the red circle indicates the current position of the cluster. The densities have been normalized to their maximum value.

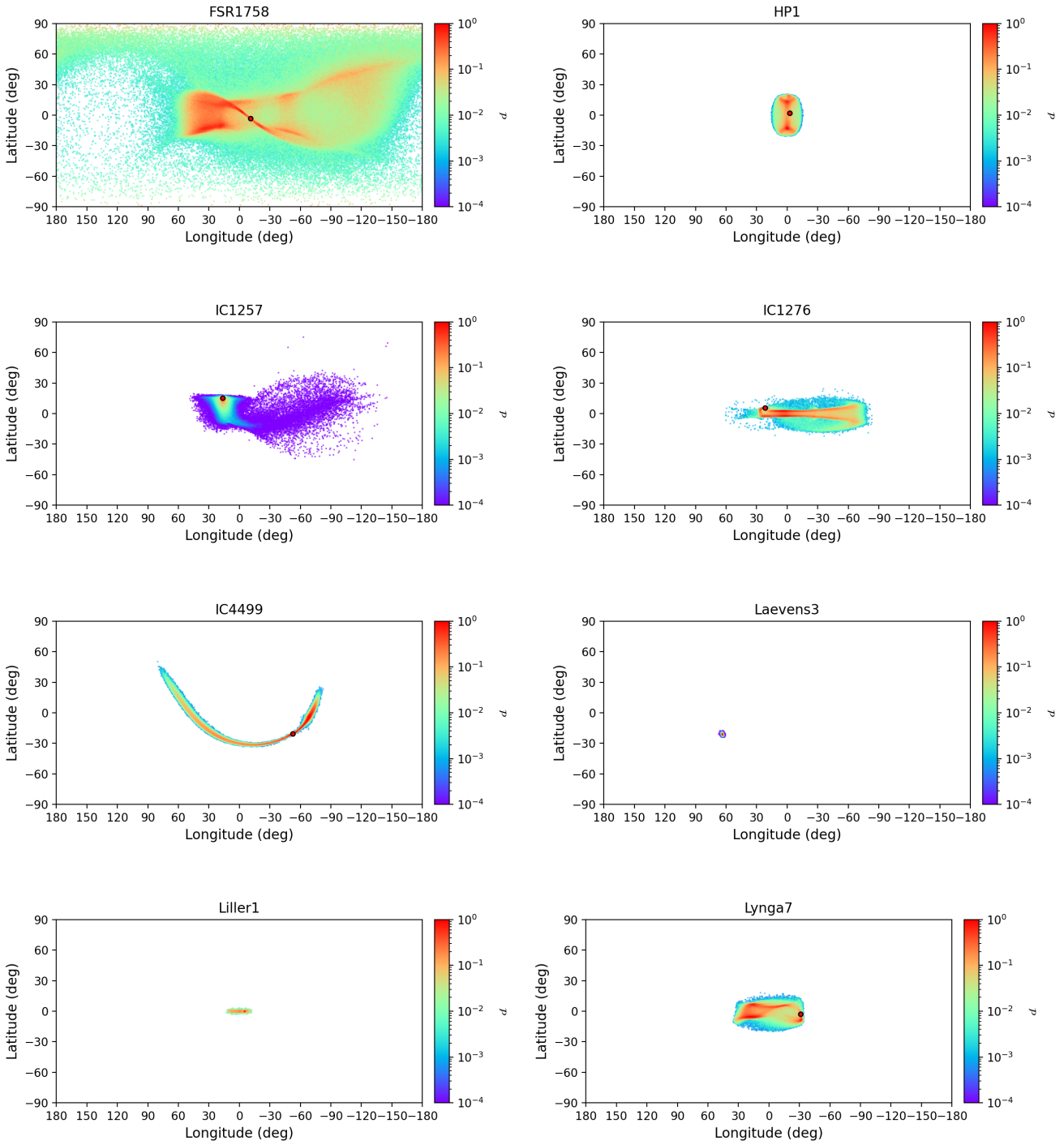


Fig. C.3. Projected density distribution in the (ℓ, b) plane of a subset of simulated globular clusters, as indicated at the top of each panel. In each panel, the red circle indicates the current position of the cluster. The densities have been normalized to their maximum value.

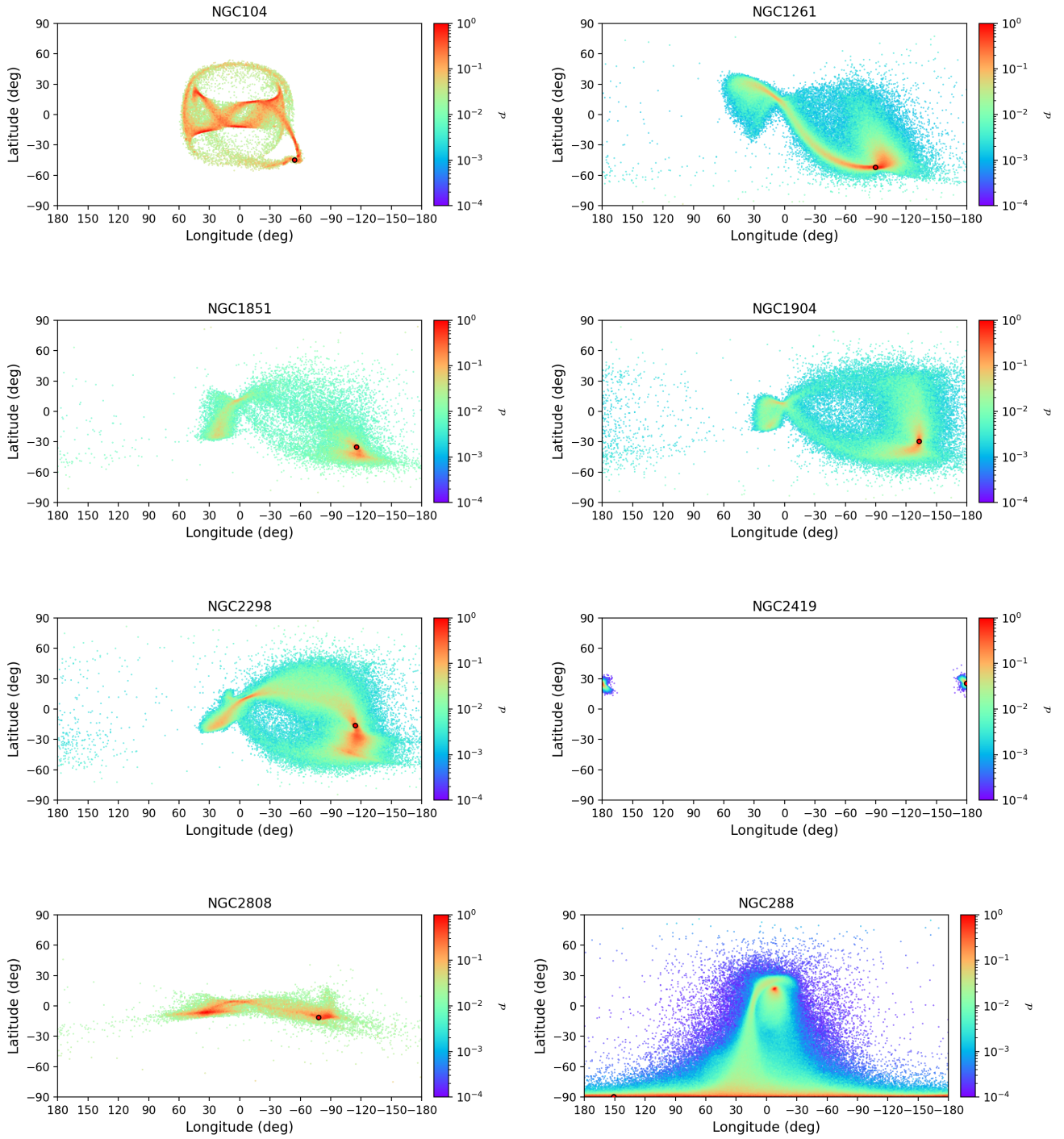


Fig. C.4. Projected density distribution in the (ℓ, b) plane of a subset of simulated globular clusters, as indicated at the top of each panel. In each panel, the red circle indicates the current position of the cluster. The densities have been normalized to their maximum value.

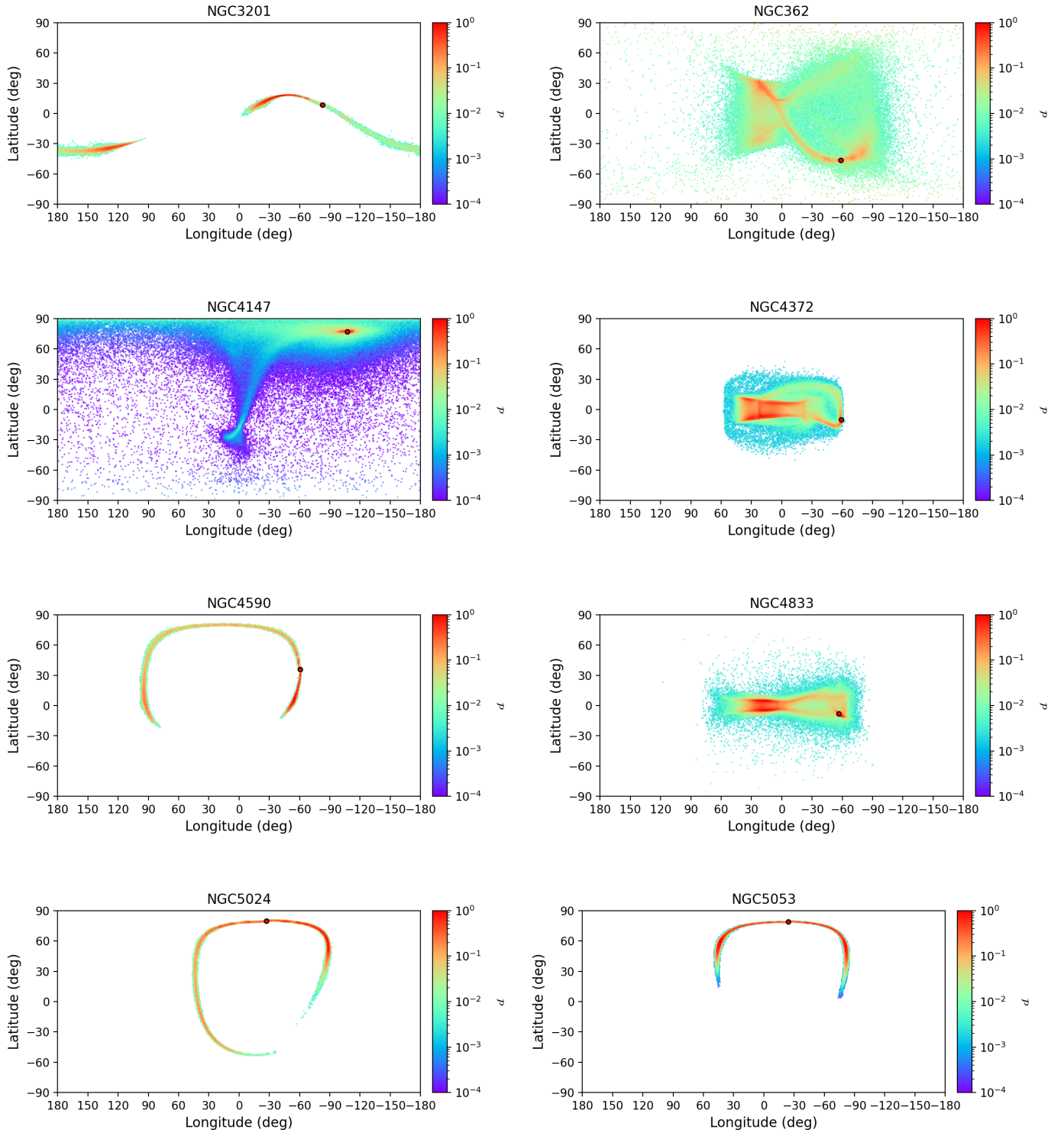


Fig. C.5. Projected density distribution in the (ℓ, b) plane of a subset of simulated globular clusters, as indicated at the top of each panel. In each panel, the red circle indicates the current position of the cluster. The densities have been normalized to their maximum value.

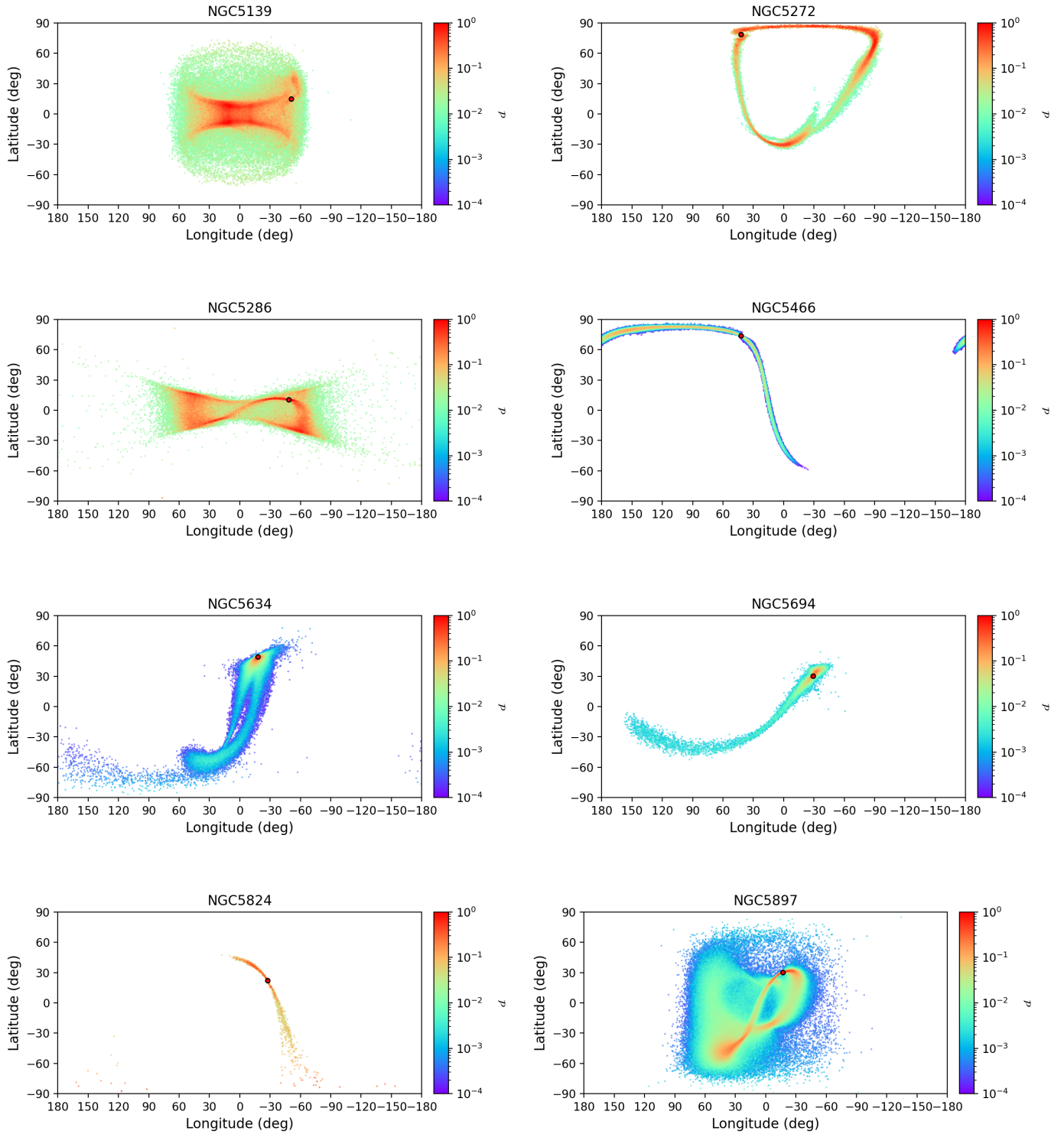


Fig. C.6. Projected density distribution in the (ℓ, b) plane of a subset of simulated globular clusters, as indicated at the top of each panel. In each panel, the red circle indicates the current position of the cluster. The densities have been normalized to their maximum value.

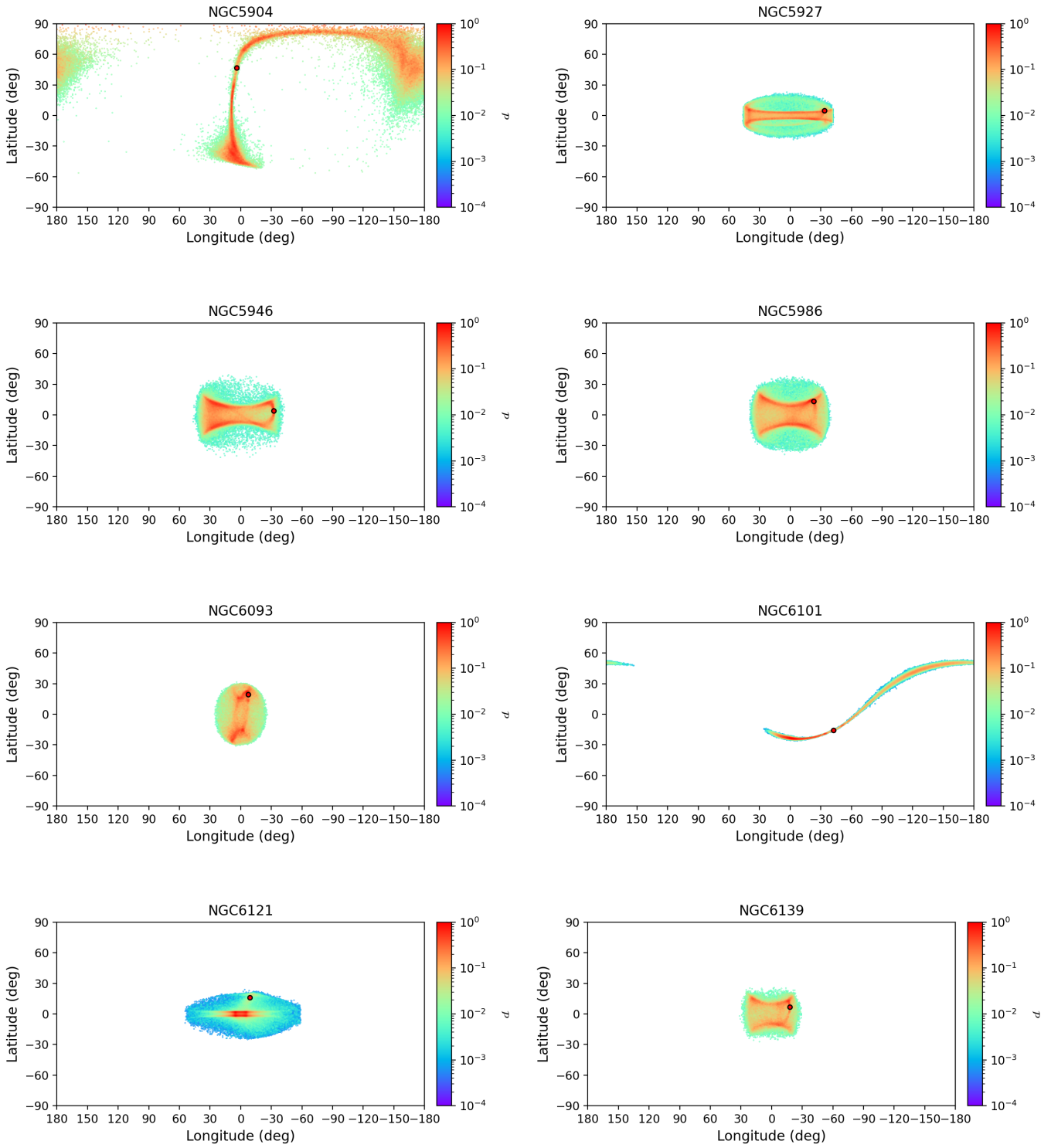


Fig. C.7. Projected density distribution in the (ℓ, b) plane of a subset of simulated globular clusters, as indicated at the top of each panel. In each panel, the red circle indicates the current position of the cluster. The densities have been normalized to their maximum value.

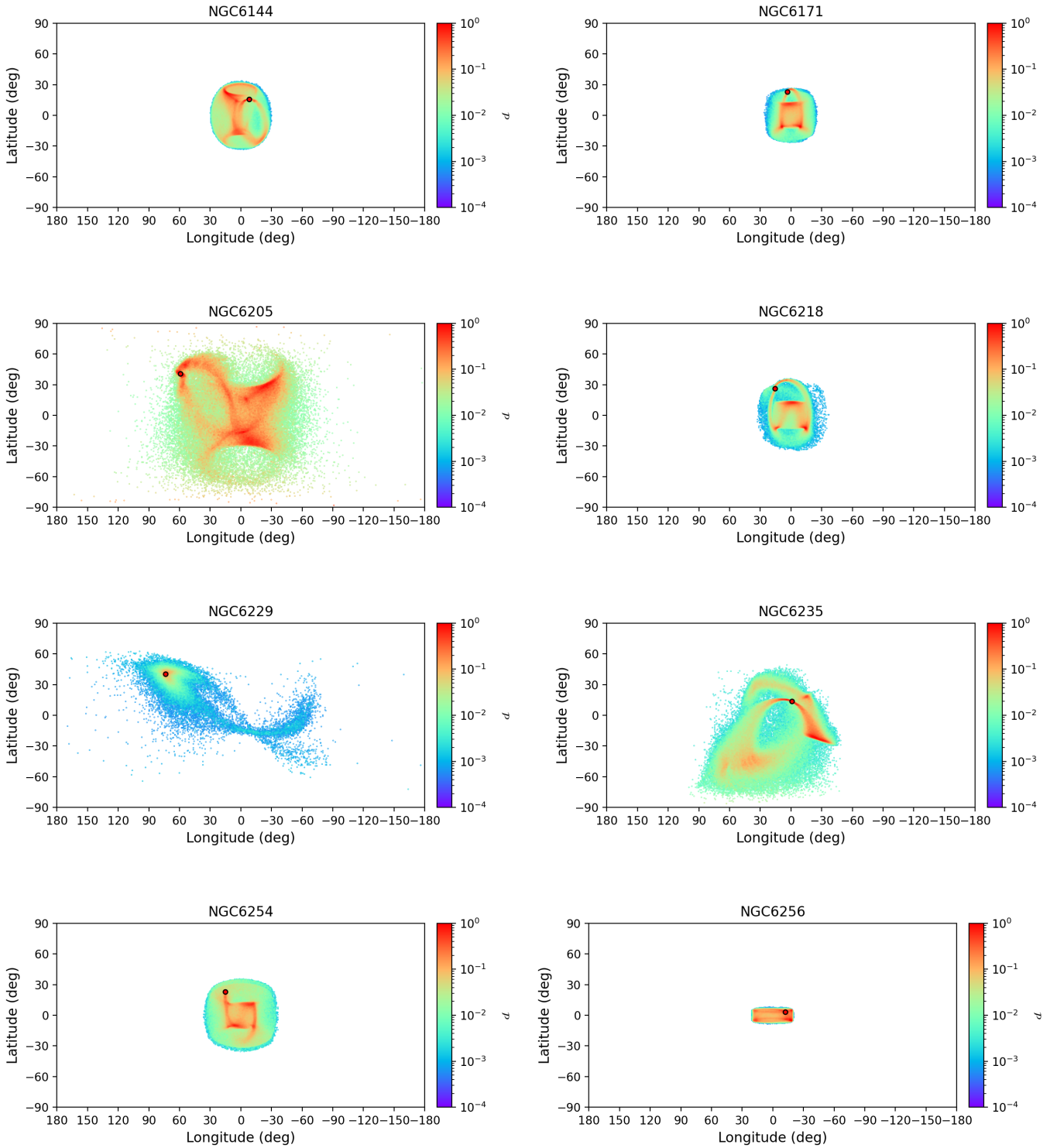


Fig. C.8. Projected density distribution in the (ℓ, b) plane of a subset of simulated globular clusters, as indicated at the top of each panel. In each panel, the red circle indicates the current position of the cluster. The densities have been normalized to their maximum value.

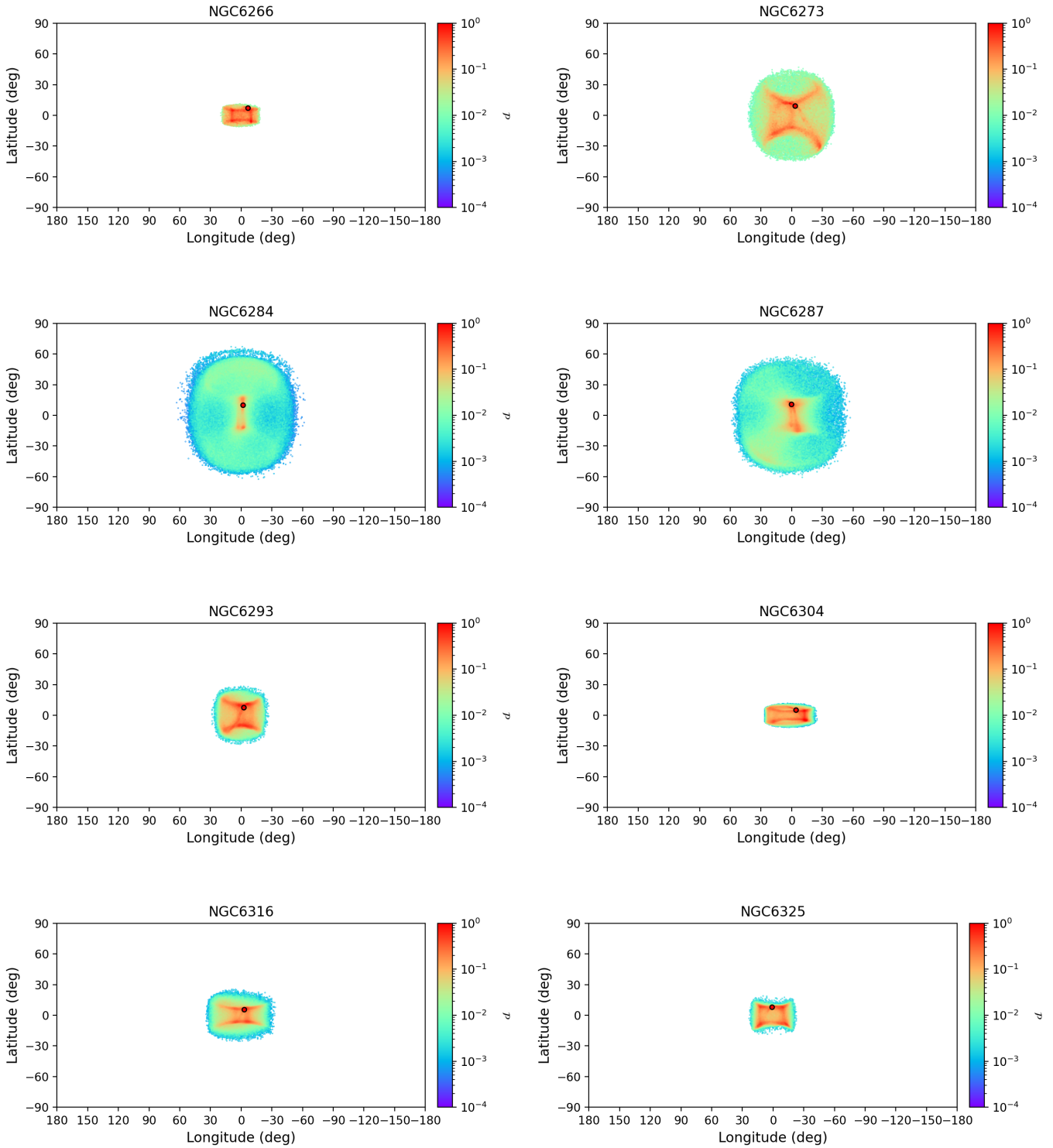


Fig. C.9. Projected density distribution in the (ℓ, b) plane of a subset of simulated globular clusters, as indicated at the top of each panel. In each panel, the red circle indicates the current position of the cluster. The densities have been normalized to their maximum value.

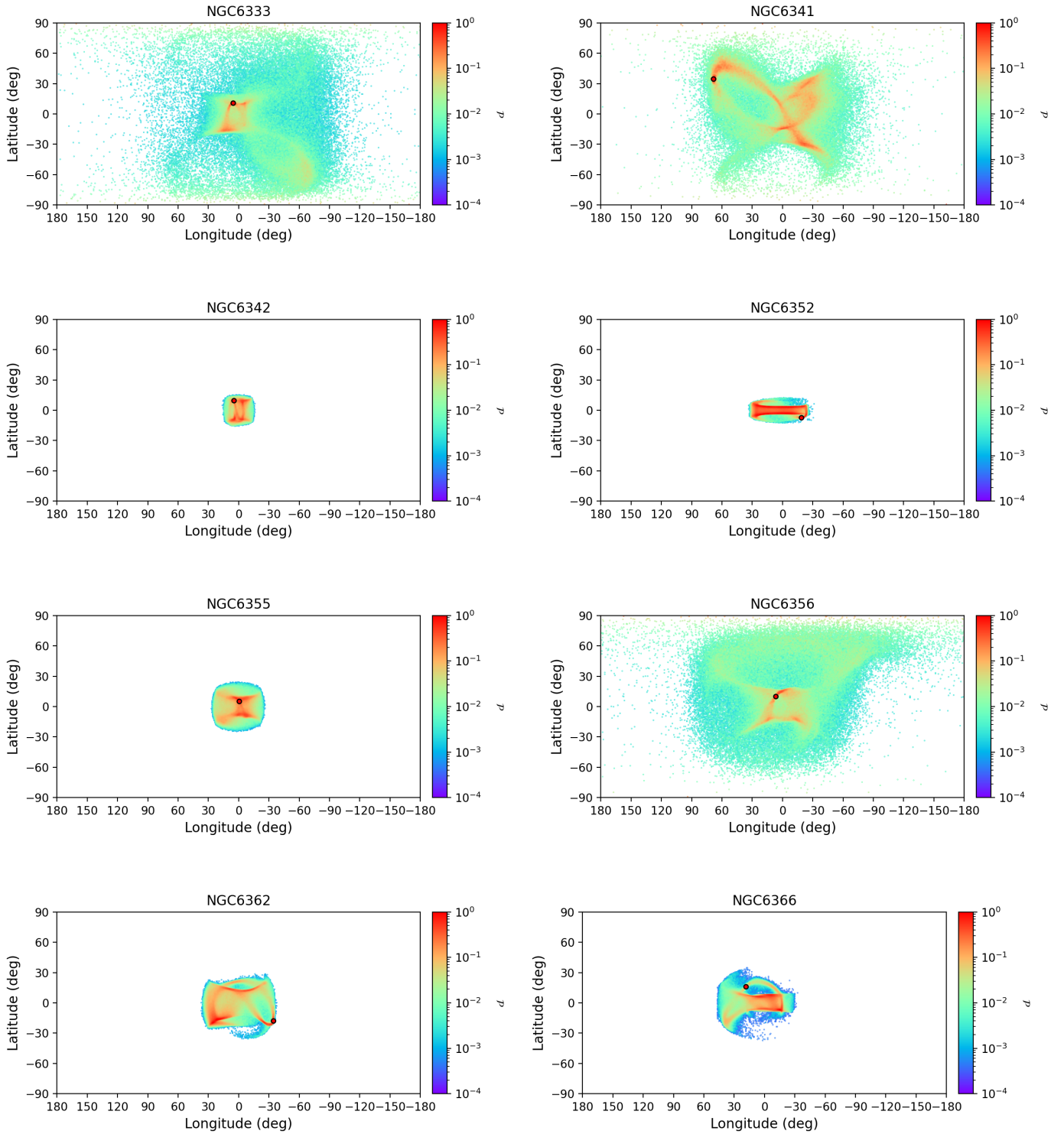


Fig. C.10. Projected density distribution in the (ℓ, b) plane of a subset of simulated globular clusters, as indicated at the top of each panel. In each panel, the red circle indicates the current position of the cluster. The densities have been normalized to their maximum value.

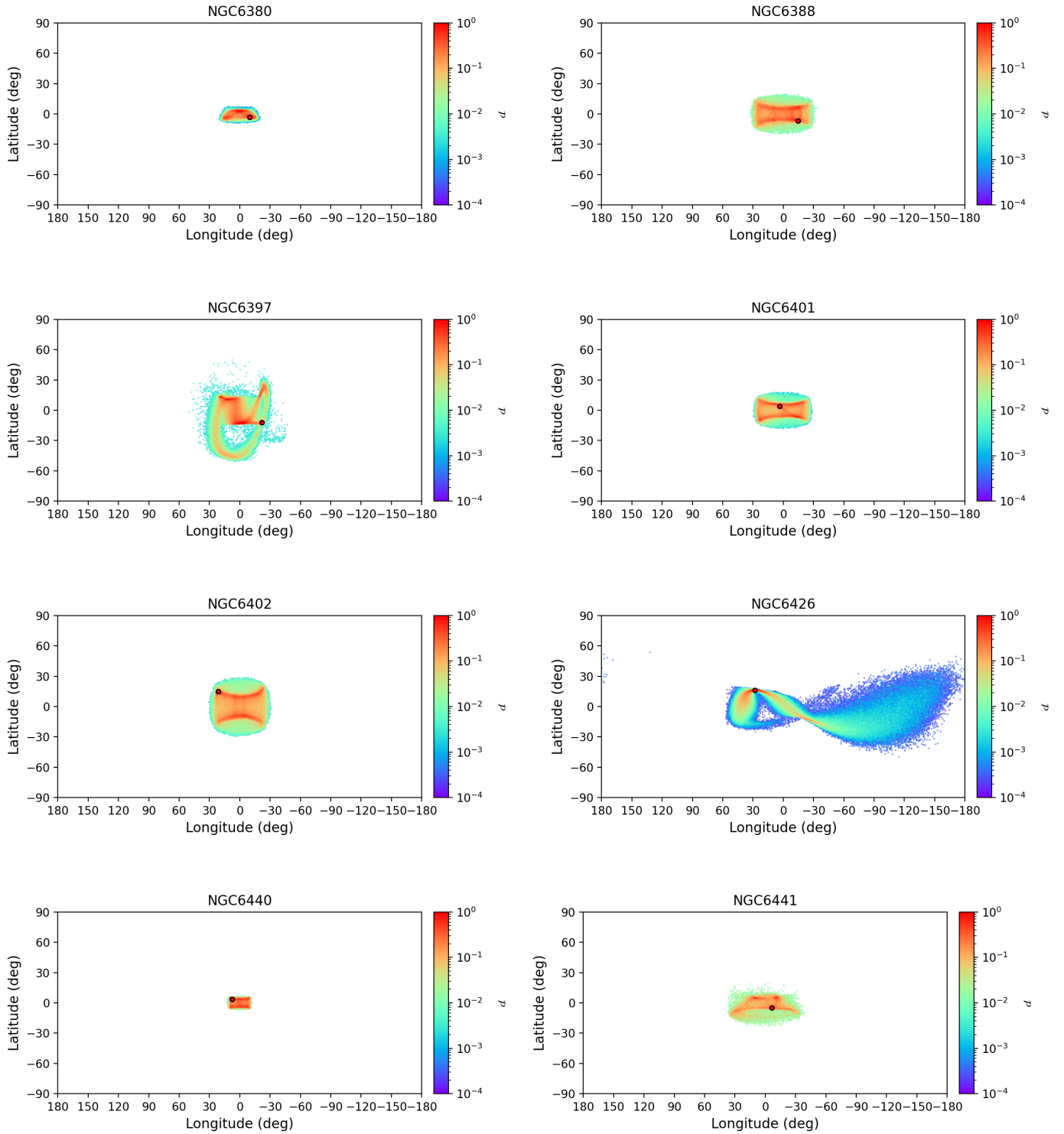


Fig. C.11. Projected density distribution in the (ℓ, b) plane of a subset of simulated globular clusters, as indicated at the top of each panel. In each panel, the red circle indicates the current position of the cluster. The densities have been normalized to their maximum value.

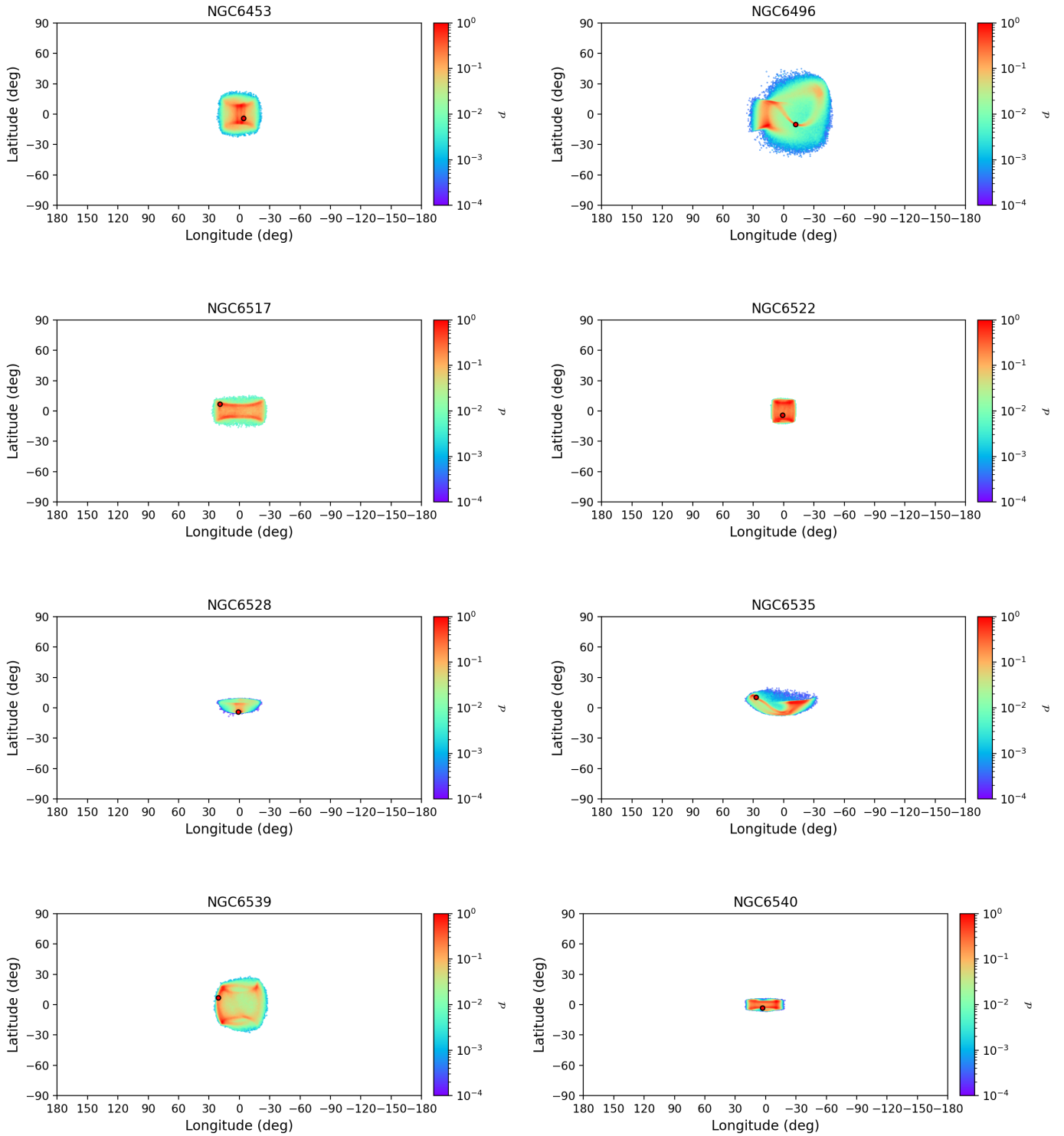


Fig. C.12. Projected density distribution in the (ℓ, b) plane of a subset of simulated globular clusters, as indicated at the top of each panel. In each panel, the red circle indicates the current position of the cluster. The densities have been normalized to their maximum value.

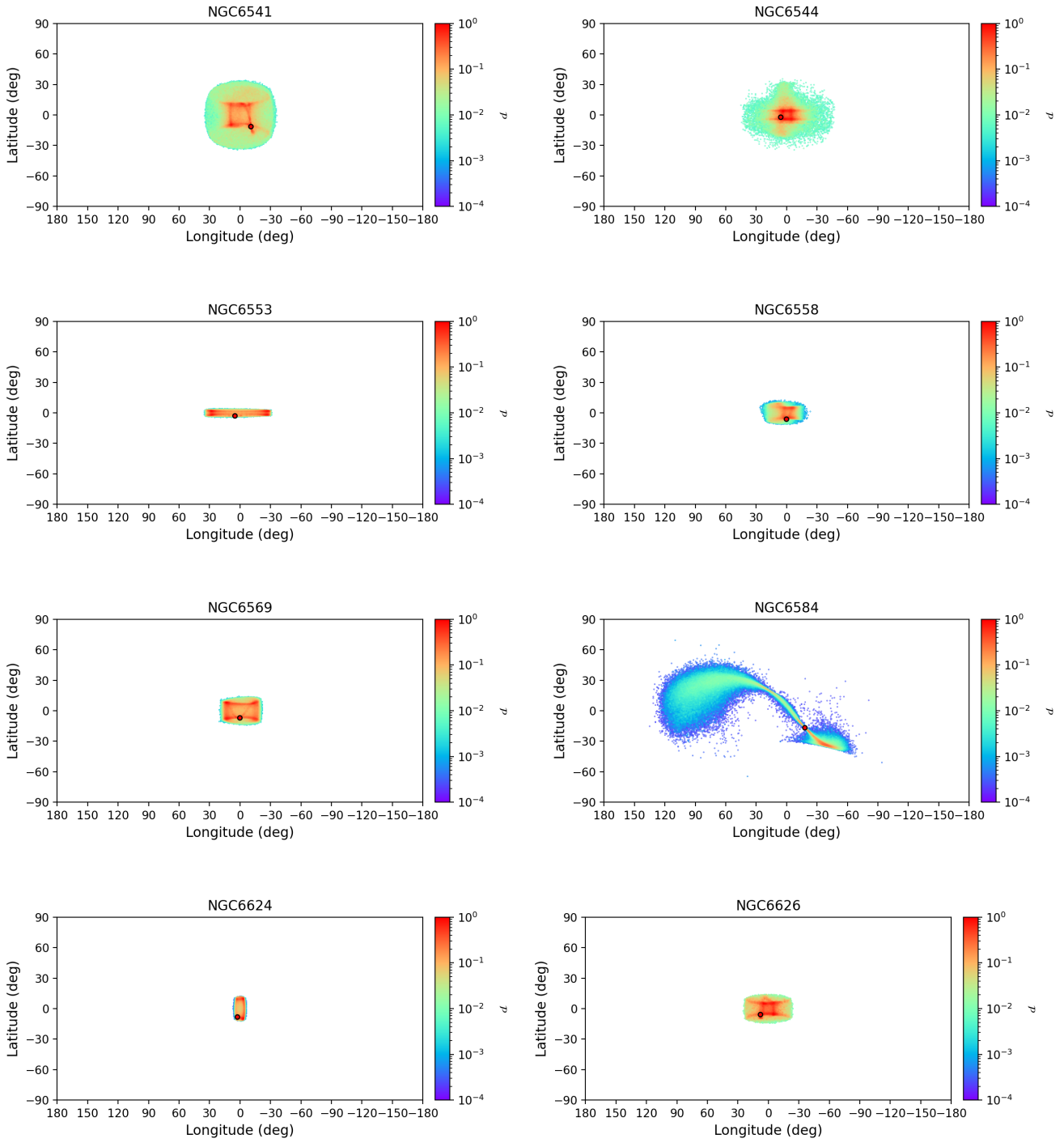


Fig. C.13. Projected density distribution in the (ℓ, b) plane of a subset of simulated globular clusters, as indicated at the top of each panel. In each panel, the red circle indicates the current position of the cluster. The densities have been normalized to their maximum value.

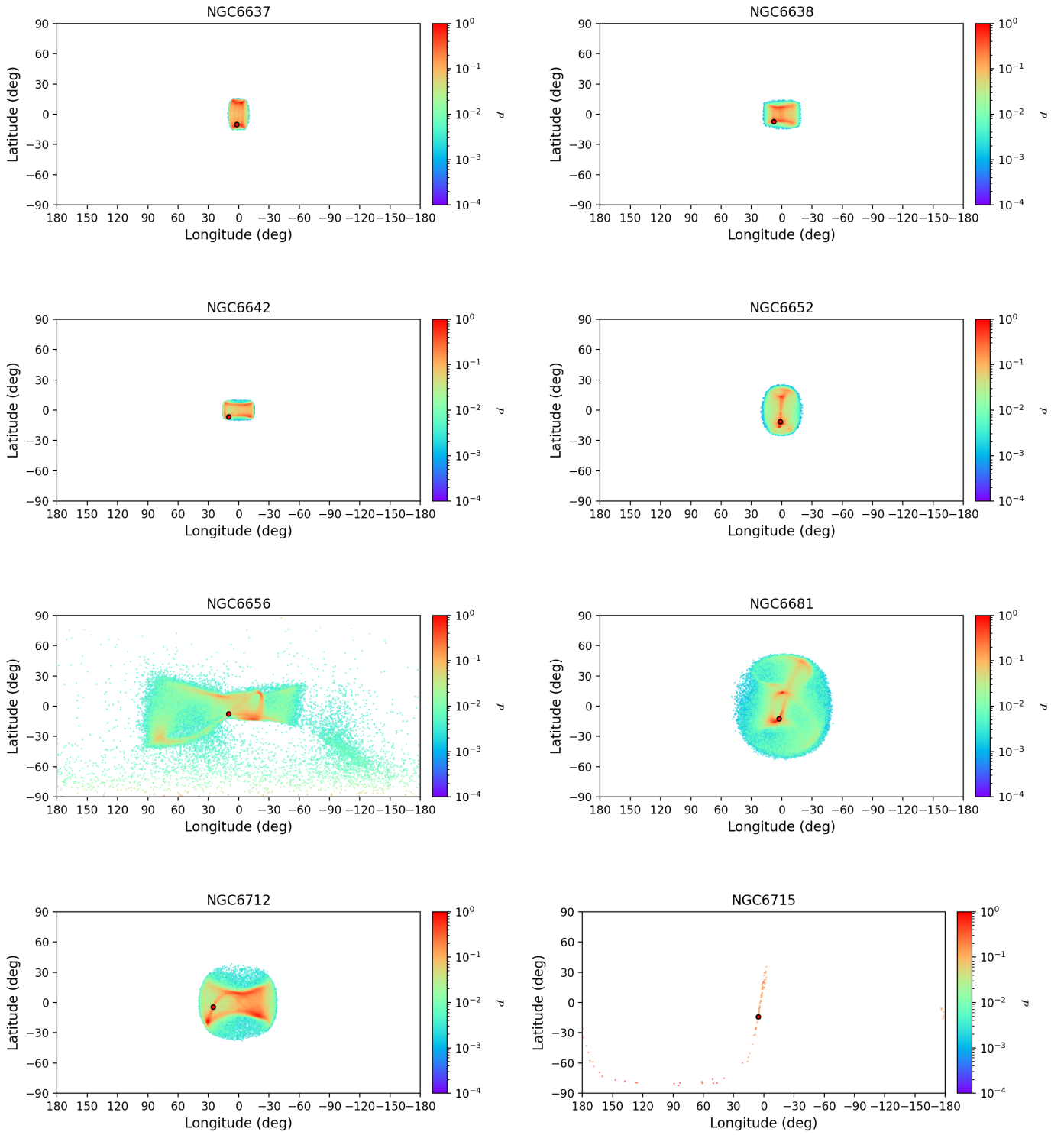


Fig. C.14. Projected density distribution in the (ℓ, b) plane of a subset of simulated globular clusters, as indicated at the top of each panel. In each panel, the red circle indicates the current position of the cluster. The densities have been normalized to their maximum value.

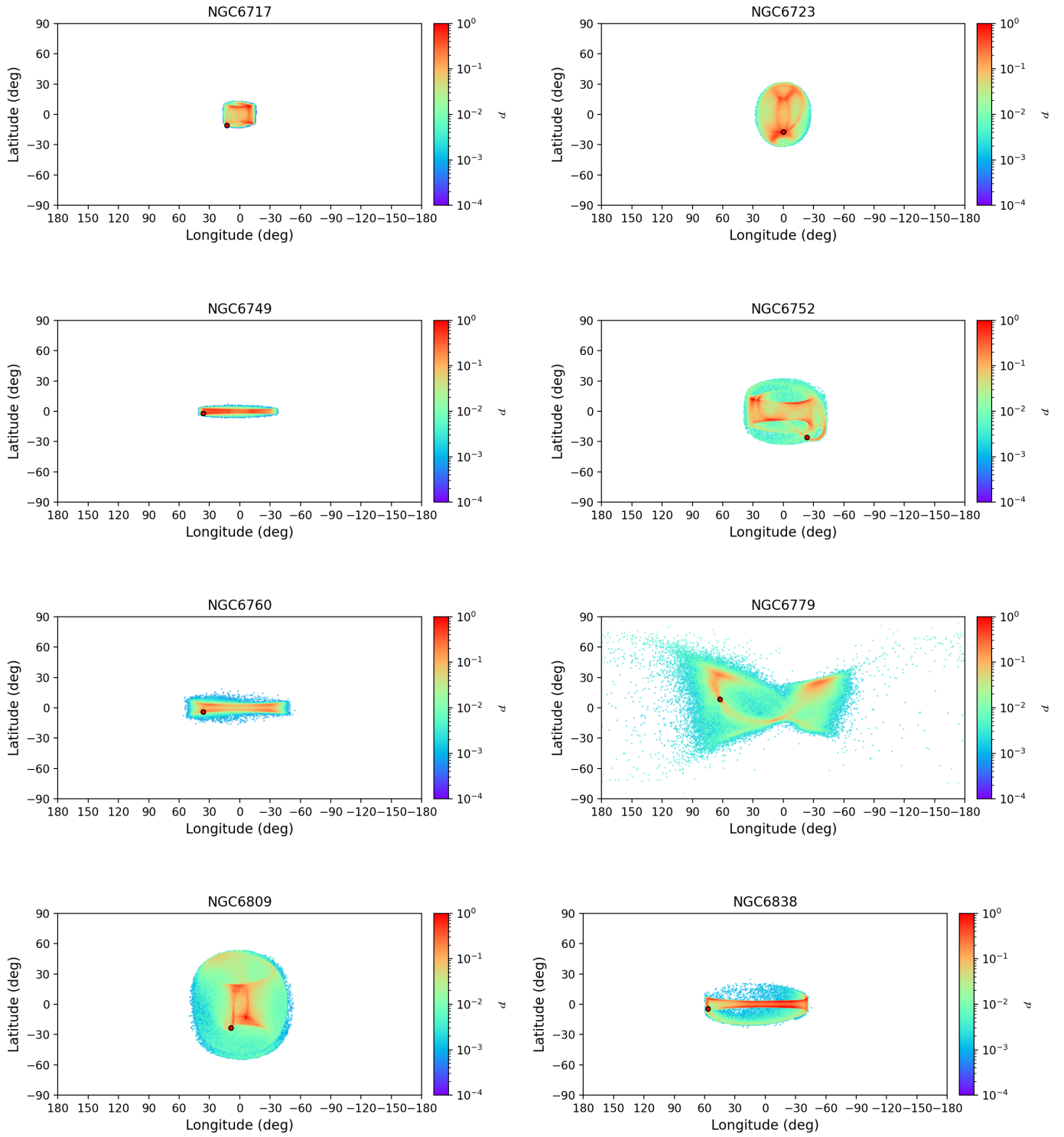


Fig. C.15. Projected density distribution in the (ℓ, b) plane of a subset of simulated globular clusters, as indicated at the top of each panel. In each panel, the red circle indicates the current position of the cluster. The densities have been normalized to their maximum value.

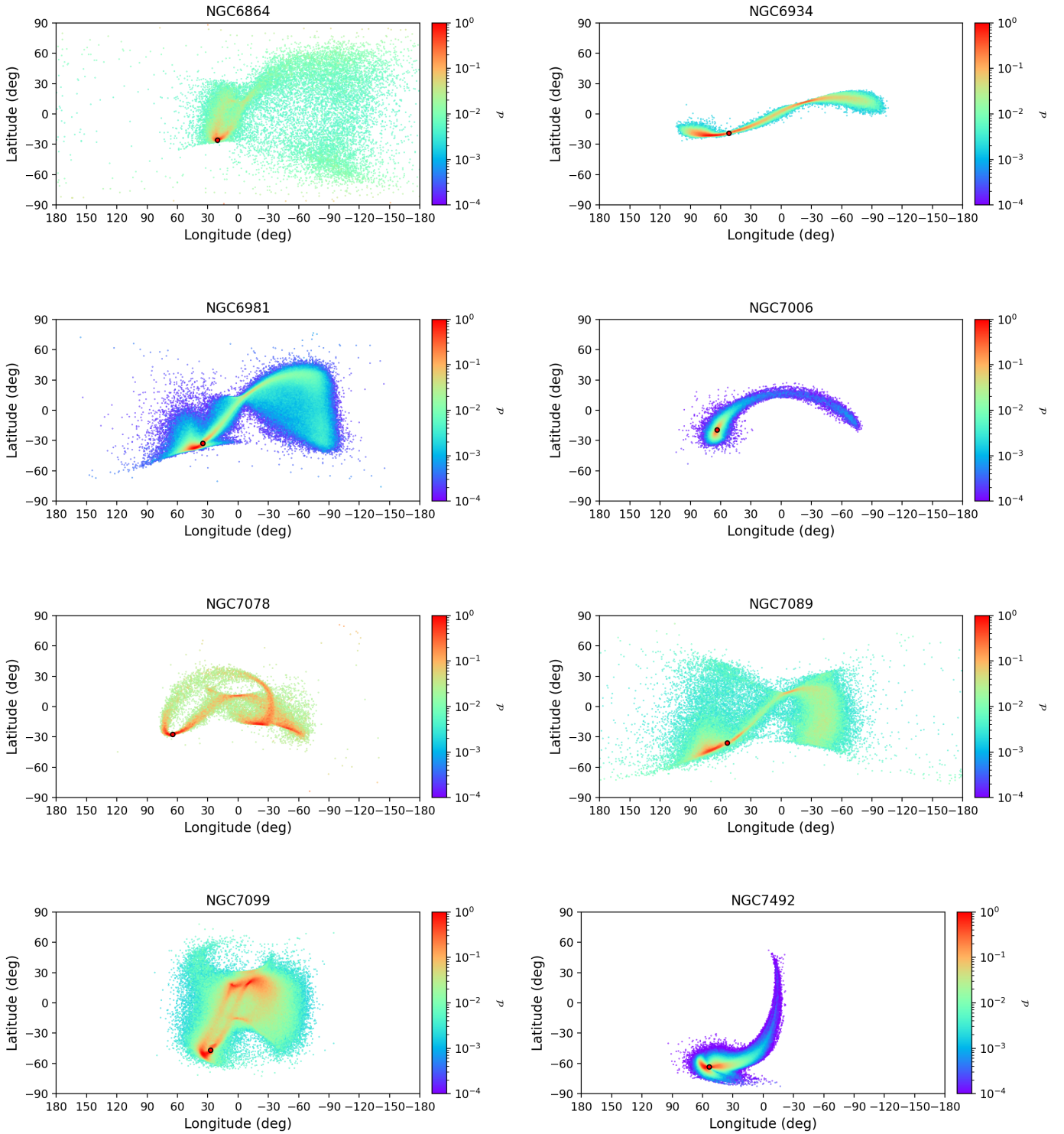


Fig. C.16. Projected density distribution in the (ℓ, b) plane of a subset of simulated globular clusters, as indicated at the top of each panel. In each panel, the red circle indicates the current position of the cluster. The densities have been normalized to their maximum value.

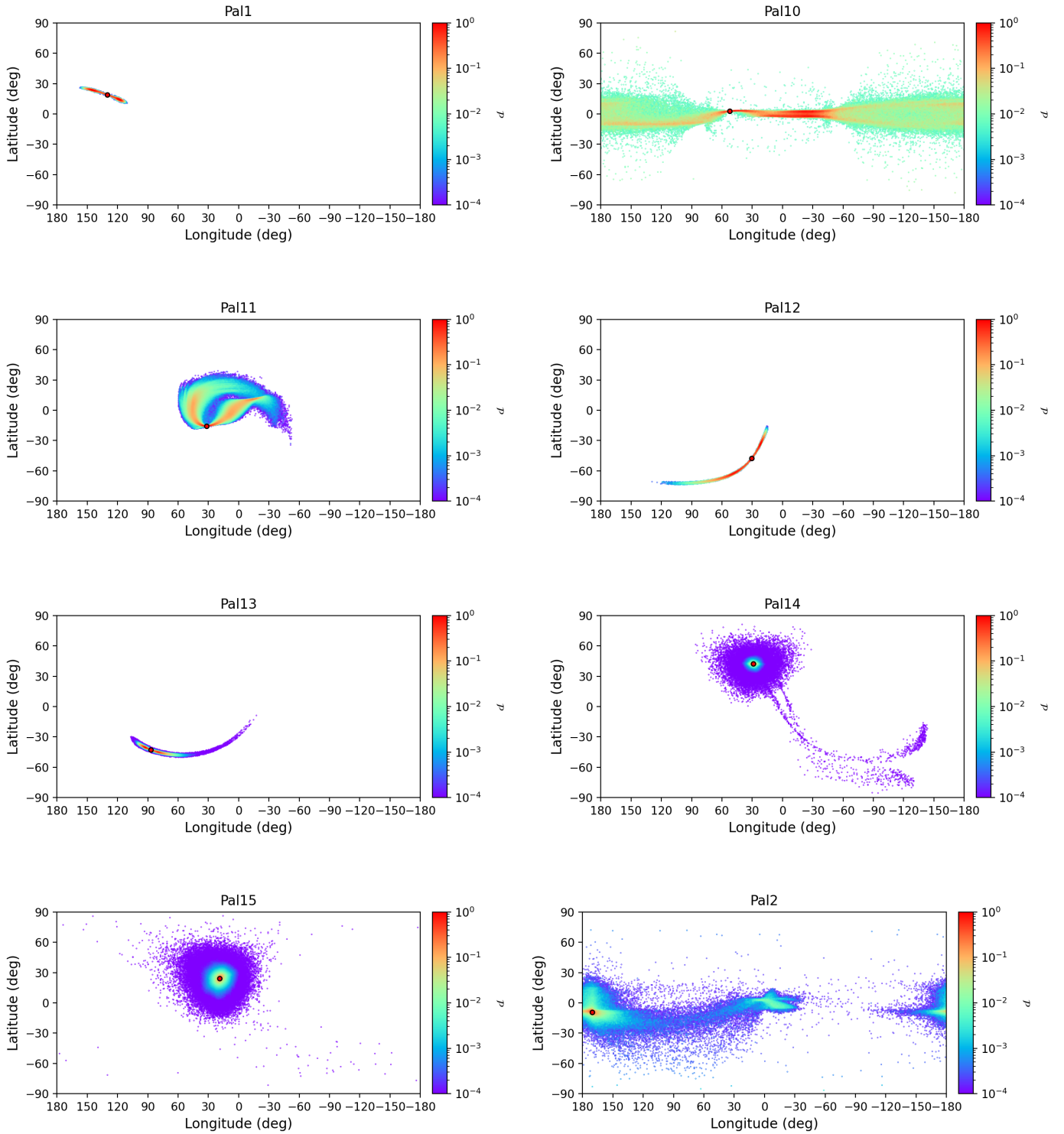


Fig. C.17. Projected density distribution in the (ℓ, b) plane of a subset of simulated globular clusters, as indicated at the top of each panel. In each panel, the red circle indicates the current position of the cluster. The densities have been normalized to their maximum value.

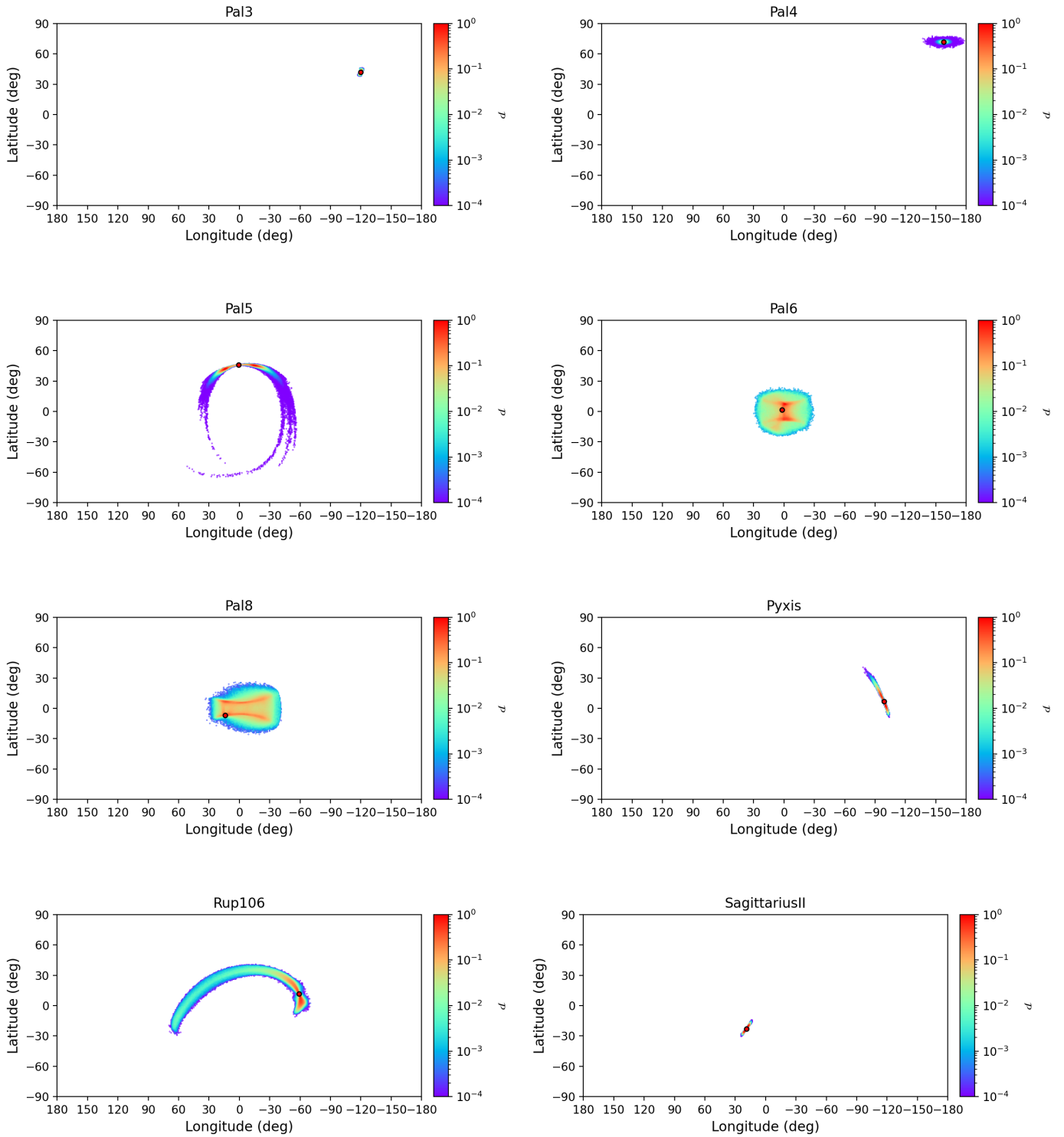


Fig. C.18. Projected density distribution in the (ℓ, b) plane of a subset of simulated globular clusters, as indicated at the top of each panel. In each panel, the red circle indicates the current position of the cluster. The densities have been normalized to their maximum value.

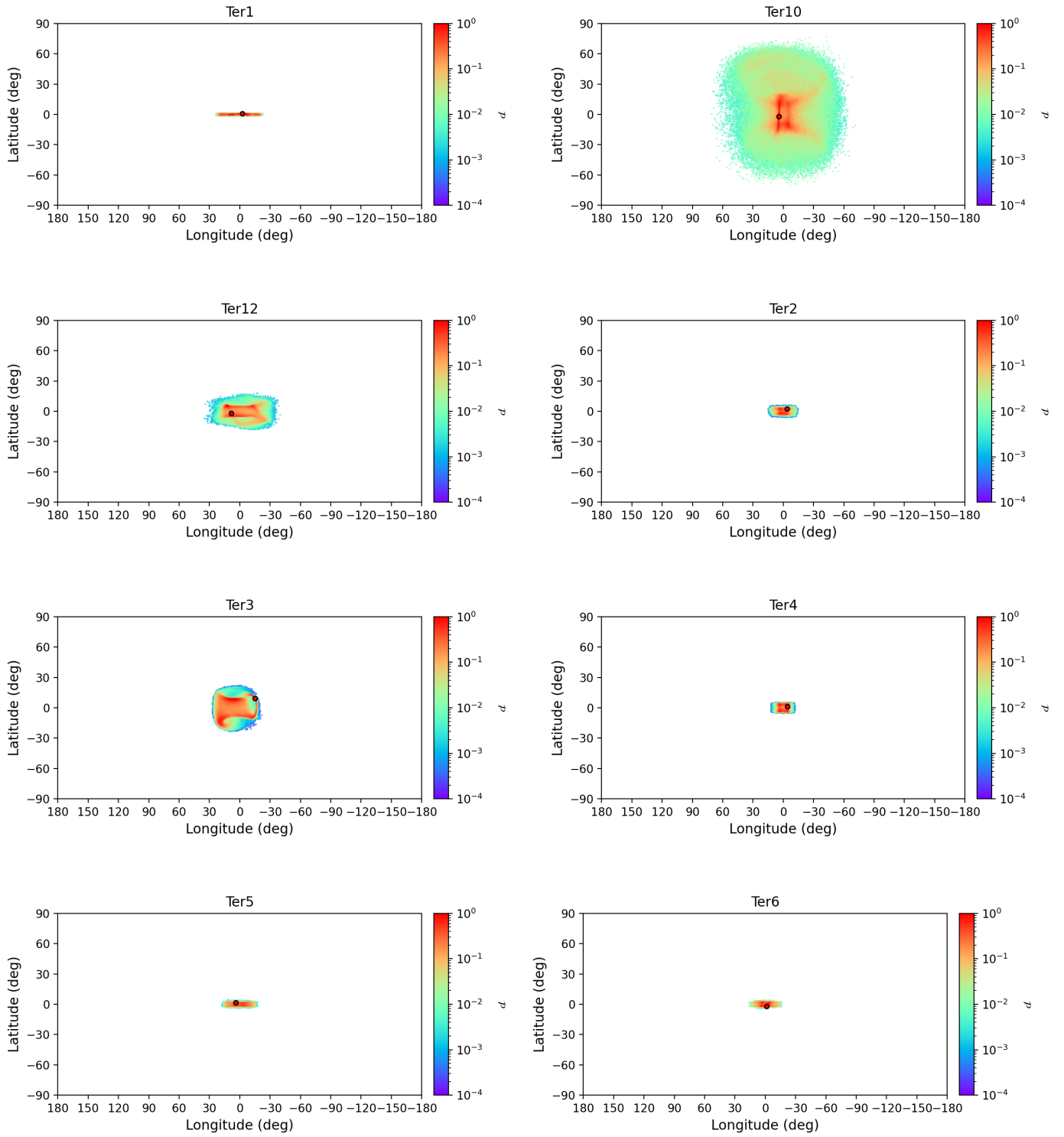


Fig. C.19. Projected density distribution in the (ℓ, b) plane of a subset of simulated globular clusters, as indicated at the top of each panel. In each panel, the red circle indicates the current position of the cluster. The densities have been normalized to their maximum value.

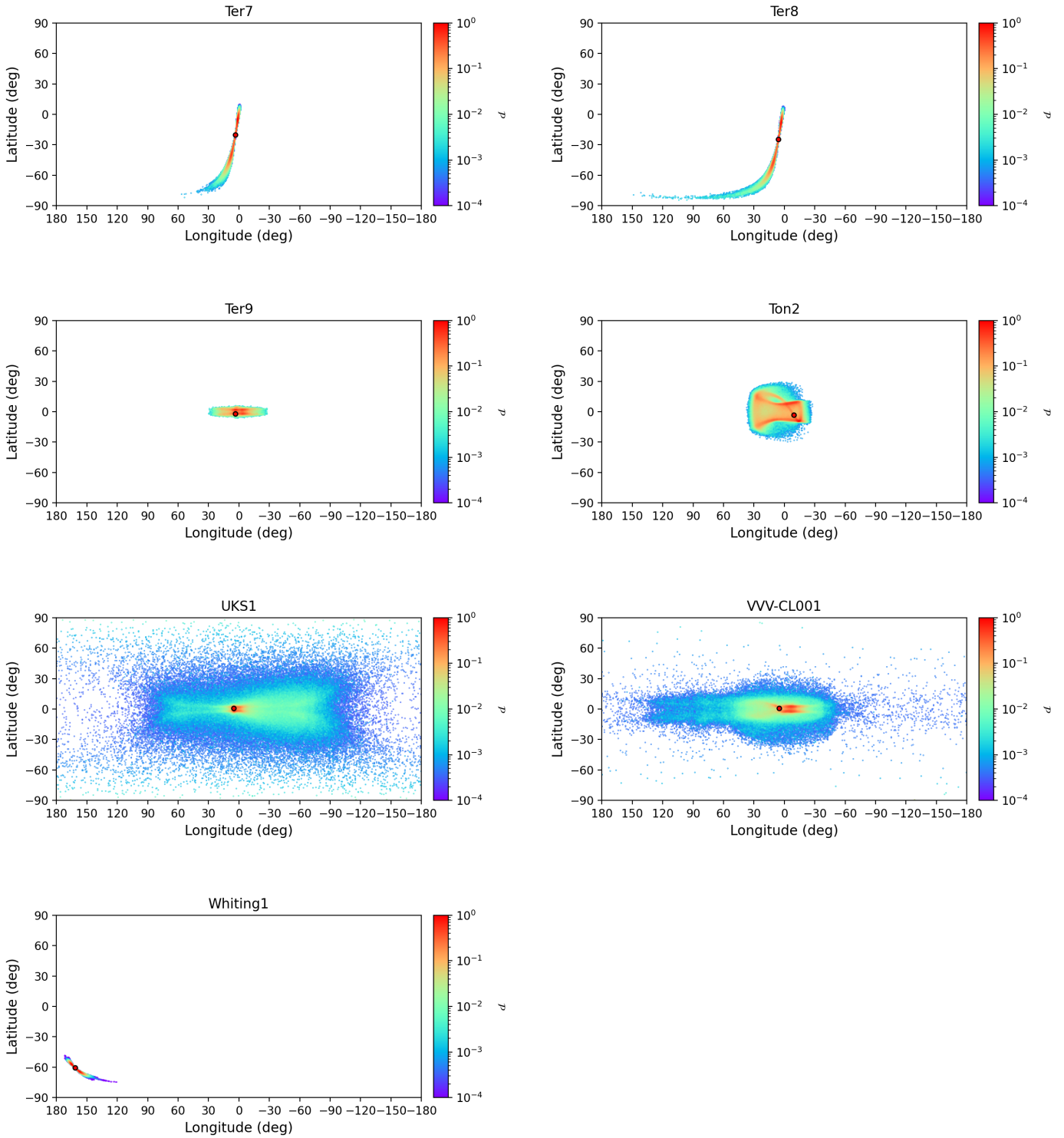


Fig. C.20. Projected density distribution in the (ℓ, b) plane of a subset of simulated globular clusters, as indicated at the top of each panel. In each panel, the red circle indicates the current position of the cluster. The densities have been normalized to their maximum value.

Appendix D: Globular cluster classification

In Fig. D.1 (top panel), we show the distribution of the arctangent of the z_{max}/R_{max} ratio, with z_{max} and R_{max} being (respectively) the maximum height above or below the Galactic plane and their maximum in-plane distance from the Galactic center that was reached in the past 5 Gyr of orbital evolution in the Galactic potential adopted in this paper (see Sect. 2.3). As was already noticed for field stars (see Haywood et al. 2018), the GC distribution also shows a dip at about 10° , which separates clusters with flattened orbits ($\arctan(z_{max}/R_{max}) \leq 10^\circ$) from thicker ones. We thus define a first set of clusters (the *disk GCs*) as that containing all globular clusters with $\arctan(z_{max}/R_{max}) \leq 10^\circ$. This first set contains 21 clusters. Of the remaining 138, we distinguish between an "inner" GCs sample and an "outer" GCs sample, on the basis of the maximum 3D distance (r_{max}) that the cluster reaches from the Galactic center. Inner GCs

are those with $r_{max} \leq 10$ kpc and outer GCs are those with $r_{max} > 8.34$ kpc, which is the value of the distance of the Sun to the Galactic Center used in this experiment. Such a value allows us to discriminate between two classes of tidal debris, for inner clusters are necessarily restricted in latitude and longitude, whereas outer cluster can fill the sky.

Finally, the third and bottom panels of Fig. D.1 show the distribution of these three defined groups in the $R_{max} - z_{max}$ and $E - L_z$ planes. We note that since disk clusters are uniquely defined on the basis of the ratio between the maximum vertical and in-plane orbital excursion – and not on the circularity of their orbits (as seen, e.g., in Massari et al. 2019), some of our disk GCs have elongated (i.e., radial) orbits ($L_z \sim 0$) or even retrograde ones ($L_z > 0$). Our definition of disk clusters is purely related to a morphological criterium: disk GCs are those whose orbits are confined close to the Galactic plane, independently of their eccentricity.

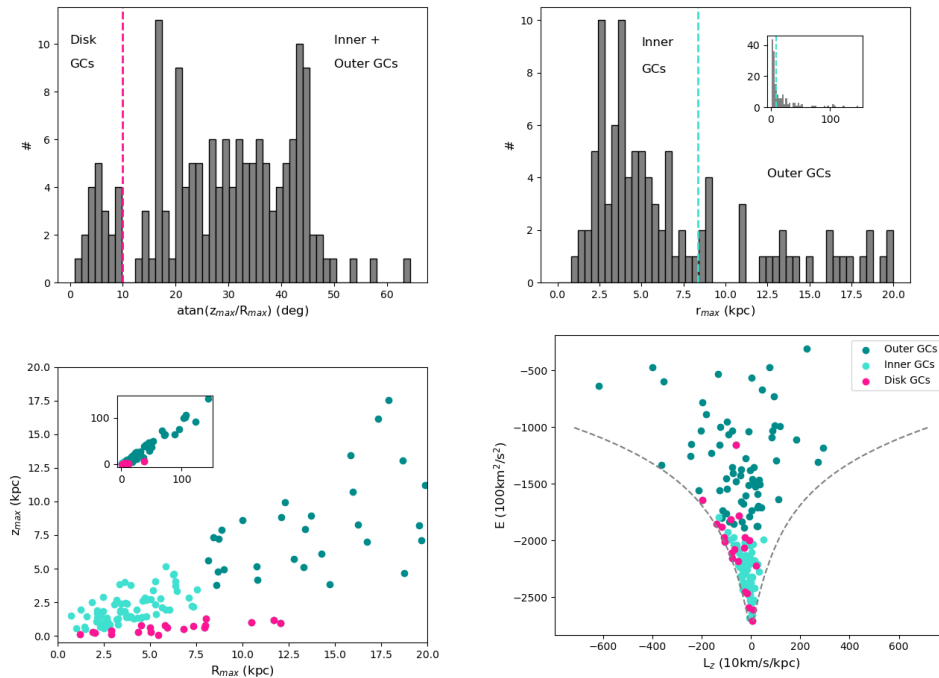


Fig. D.1. A series of plots describing the categorization of disk, inner, and outer globular clusters. *From the top left to the bottom right:* *First panel:* Distribution of the arctangent of the z_{max}/R_{max} ratio for all simulated GCs. The values are expressed in degrees. The vertical dashed line at 10° separates disk clusters ($\arctan(z_{max}/R_{max}) \leq 10^\circ$) from the rest of the population of GCs. *Second panel:* Distribution of the maximum 3D distance, r_{max} , from the Galactic center, reached by the GCs orbits in the last 5 Gyr. The main plot shows this distribution for $r_{max} \leq 20$ kpc, where (as the inset shows) the whole distribution is extended at $r_{max} > 100$ kpc. In both panels, the vertical dashed line, at the solar radius r_\odot , separates the group of inner GCs from the group of outer GCs. We note that the clusters in one of these two groups which also satisfy the criterion to be disk clusters are classified as disk GCs and are not in the inner or outer GC groups. *Third panel:* Distribution of disk GCs (magenta points), inner GCs (turquoise points), and outer GCs (dark turquoise points) in the $R_{max} - z_{max}$ plane. The main panel shows the distribution of the GCs having $R_{max} \leq 20$ kpc, the inset the distribution of the whole GC sample. *Fourth panel:* Distribution of the disk GCs (magenta points), inner GCs (turquoise points), and outer GCs (dark turquoise points) in the $E - L_z$ plane. The dashed grey lines correspond, for any given energy E , to the angular momentum of the corresponding circular orbit. Prograde orbits correspond to negative L_z values, retrograde orbits to positive L_z .

Table D.1. Classification of the 159 globular clusters studied in this paper in disk clusters ("D"), inner clusters ("I") and outer clusters ("O"). The values of r_{max} and the angle in degrees of the $\arctan(z_{max}/R_{max})$ are also given.

Cluster	r_{max}	angle	class	Cluster	r_{max}	angle	class	Cluster	r_{max}	angle	class
2MASS-GC01	5.45	0.85	D	2MASS-GC02	7.38	17.15	I	AM1	123.19	36.56	O
AM4	26.97	43.53	O	Arp2	42.44	44.54	O	BH140	10.52	5.54	D
BH261	3.83	21.02	I	Crater	147.37	44.46	O	Djor1	11.74	5.77	D
Djor2	2.39	16.74	I	E3	12.91	24.07	O	ESO280-SC06	13.82	33.04	O
ESO452-SC11	2.53	41.47	I	Eridanus	109.07	44.83	O	FSR1716	5.46	17.07	I
FSR1735	4.43	17.10	I	FSR1758	14.35	23.13	O	HP1	2.70	53.56	I
IC1257	19.69	19.93	O	IC1276	7.98	5.71	D	IC4499	27.17	42.77	O
Laevens3	70.74	41.35	O	Liller1	1.20	5.84	D	Lynga7	4.69	17.18	I
NGC104	7.71	24.70	I	NGC1261	20.99	36.68	O	NGC1851	19.94	29.46	O
NGC1904	19.57	22.81	O	NGC2298	16.69	26.93	O	NGC2419	96.76	38.13	O
NGC2808	14.92	14.57	O	NGC288	12.50	39.00	O	NGC3201	25.53	22.62	O
NGC362	12.27	36.03	O	NGC4147	24.90	45.18	O	NGC4372	7.36	16.30	I
NGC4590	27.99	32.55	O	NGC4833	8.13	9.07	D	NGC5024	22.32	44.24	O
NGC5053	18.08	44.39	O	NGC5139	7.14	21.89	I	NGC5272	16.02	40.27	O
NGC5286	13.32	21.11	O	NGC5466	41.16	43.51	O	NGC5634	22.18	43.13	O
NGC5694	51.29	35.50	O	NGC5824	32.44	40.00	O	NGC5897	9.18	41.61	O
NGC5904	24.76	42.83	O	NGC5927	5.83	7.91	D	NGC5946	5.31	23.80	I
NGC5986	5.00	29.36	I	NGC6093	4.04	49.12	I	NGC6101	32.24	30.56	O
NGC6121	6.84	4.48	D	NGC6139	3.72	34.95	I	NGC6144	4.41	43.66	I
NGC6171	3.95	33.40	I	NGC6205	8.96	39.68	O	NGC6218	4.95	31.01	I
NGC6229	30.26	37.44	O	NGC6235	8.37	34.55	O	NGC6254	4.98	29.32	I
NGC6256	2.68	14.83	I	NGC6266	2.57	21.99	I	NGC6273	5.56	37.78	I
NGC6284	6.51	36.21	I	NGC6287	6.50	30.33	I	NGC6293	3.40	37.21	I
NGC6304	3.38	14.75	I	NGC6316	3.80	22.98	I	NGC6325	2.57	32.34	I
NGC6333	9.07	28.89	O	NGC6341	10.90	40.72	O	NGC6342	2.48	38.09	I
NGC6352	4.53	9.72	D	NGC6355	3.55	29.38	I	NGC6356	8.83	28.77	O
NGC6362	5.41	33.16	I	NGC6366	6.04	17.80	I	NGC6380	2.35	16.74	I
NGC6388	3.91	19.73	I	NGC6397	6.61	27.48	I	NGC6401	3.70	21.02	I
NGC6402	3.99	32.64	I	NGC6426	16.84	22.68	O	NGC6440	1.53	25.31	I
NGC6441	4.67	16.48	I	NGC6453	2.71	36.68	I	NGC6496	5.71	26.65	I
NGC6517	3.31	21.34	I	NGC6522	1.97	42.54	I	NGC6528	2.89	16.38	I
NGC6535	4.92	16.72	I	NGC6539	3.64	39.67	I	NGC6540	2.54	12.61	I
NGC6541	4.78	29.39	I	NGC6544	5.93	18.30	I	NGC6553	4.36	4.14	D
NGC6558	2.75	21.35	I	NGC6569	2.85	26.50	I	NGC6584	20.31	35.07	O
NGC6624	1.61	64.40	I	NGC6626	3.22	20.88	I	NGC6637	2.11	56.81	I
NGC6638	2.34	31.98	I	NGC6642	2.20	26.61	I	NGC6652	3.15	49.58	I
NGC6656	10.87	21.01	O	NGC6681	6.33	41.70	I	NGC6712	5.15	28.49	I
NGC6715	38.71	45.11	O	NGC6717	2.48	33.11	I	NGC6723	4.26	47.80	I
NGC6749	5.05	3.24	D	NGC6752	5.72	20.72	I	NGC6760	5.95	6.19	D
NGC6779	13.46	30.72	O	NGC6809	6.50	36.15	I	NGC6838	7.34	5.82	D
NGC6864	16.06	33.89	O	NGC6934	37.41	20.95	O	NGC6981	21.54	35.97	O
NGC7006	47.26	32.50	O	NGC7078	10.86	25.72	O	NGC7089	18.77	34.91	O
NGC7099	8.76	40.99	O	NGC7492	25.78	45.99	O	Pal1	18.77	13.96	O
Pal10	12.06	4.56	D	Pal11	8.69	23.83	O	Pal12	41.33	42.80	O
Pal13	49.09	42.54	O	Pal14	88.95	35.97	O	Pal15	46.62	44.52	O
Pal2	38.20	8.94	D	Pal3	104.49	43.88	O	Pal4	105.89	43.58	O
Pal5	17.54	42.94	O	Pal6	3.53	27.77	I	Pal8	3.99	20.14	I
Pyxis	73.65	47.40	O	Rup106	32.08	31.98	O	SagittariusII	75.32	41.80	O
Ter1	2.92	2.13	D	Ter10	6.55	32.40	I	Ter12	4.23	17.31	I
Ter2	1.49	18.30	I	Ter3	3.81	26.97	I	Ter4	1.11	28.72	I
Ter5	2.04	7.10	D	Ter6	1.93	8.77	D	Ter7	41.39	45.10	O
Ter8	47.16	45.55	O	Ter9	2.92	7.94	D	Ton2	4.39	24.81	I
UKS1	7.95	4.51	D	VVV-CL001	5.04	7.09	D	Whiting1	52.30	43.09	O